

4.1 Displacements

The most fundamental response quantities to compare are displacements, so significant emphasis was placed on measurements and comparisons of these. As discussed later, various local phenomena can significantly influence the measurements of strains in the liner, reinforcement, or tendons, but displacement measurements are regarded as the most reliable source of general response information. Much global strain information can also be inferred from displacement measurement by using, for example, a kinematic relationship such as

$$\epsilon_h = \frac{u_r}{R},$$

where ϵ_h is the hoop strain, u_r is the radial displacement, and R is the radius.

Meridional strain can also be inferred from the difference in vertical displacement divided by the gage length in between.

Displacements as a function of pressure are compared at SOLs 1 through 14 in Figures 4-1 through 4-4. Each comparison plot includes four curves:

1. LST DOR
2. LST correction (LST DOR corrected for ambient temperature effects, as per Reference [8])
3. 2000 analysis (final pretest analysis performed just prior to the test and discussed in Chapter 2)
4. 1999 analysis (published pretest analysis [1] and [4])

A discussion of each comparison is listed by location, below. One additional adjustment to the analysis results should be noted. To focus on comparing the pressure response of the model, all of the analysis results were shifted so that the calculated zero pressure response matched the data at the start of the test. This eliminated differences that could occur due to creep or other time dependent effects. The only other loading conditions considered in the analyses, besides internal pressurization, were dead load and prestressing loads. Since the PCCV instrumentation was initialized on March 3, 2000, after construction was essentially complete, response to dead load was not measured. The model was then completely prestressed, exposed to six months of ambient temperature fluctuations (during which the model was allowed to creep, shrink, and relax), and finally to preliminary pressure testing prior to the start of the LST. By adjusting the analysis results, differences due to these secondary effects were eliminated from the comparison to the pressure response.

SOL 1. Vertical Displacement at Outside Edge, Top of Basemat. The test data shows virtually no uplift, while the analyses at 3.3 Pd show 2.3mm and 9mm for the 1999 and 2000 analyses, respectively. The apparent discrepancy between the test data and the analysis results may be an artifact from the way basemat uplift was measured during the LST. The displacement gage(s) were mounted to measure the relative displacement between the bottom of the basemat and the top of the underlying mud-mat, since there were no other practical means of referencing a fixed point. In an analysis that uses a very stiff foundation, even very small basemat curvatures create appreciable basemat uplift, but being much more flexible, mud-mat flexure can be assumed to follow basemat flexure. As a result, there could have been appreciable basemat flexure without the mud-mat ever separating from the PCCV basemat and, therefore, no observed relative motion. Unfortunately, there is no way to corroborate the accuracy of the analysis predictions for basemat uplift. The differences between the analyses and the test, and between the analyses themselves, are both noteworthy and are discussed in the revised global posttest analysis in Chapter 5.

SOLs 2, 3, 4, 5, 6, 14, and 15. There is very good agreement (to within +/- 4% over most of the pressurization history) for all of the cylinder radial displacement locations between analysis and test, but a few general observations can be made. The analyses and the test consistently exhibit a sharp jump in displacement at approximately 1.45 Pd (0.57 MPa). This is possibly associated with the onset of hoop cracking in the cylinder, although the data is not entirely conclusive on this point. At first, it was thought this was associated with the 3 hour pressure hold at 1.5 Pd, but the jump in the data occurs just prior to the 1.5 Pd pressure hold. Also, there is no similar jump in data at the 2.0 Pd pressure hold, which was held overnight. The radial displacement at the A/L is somewhat overpredicted beyond 2.8 Pd.

SOLs 7, 8, 9, 10, and 11. There is poor correlation between analysis and test data for these displacements in the dome and springline. Radial displacements at the springline were underpredicted in analysis by roughly a factor of 2. Vertical

displacement was also off, but overprediction is understandable, given the significant overprediction of basemat uplift. (The 1999 analysis better predicts this quantity than the 2000 analysis.) The same is true for vertical displacements at the dome 45-degree-angle and the apex, but the radial displacement at the dome 45-degree-angle is well predicted (to within +/- 20%).

SOLs 12 and 13. At the buttress locations, the analysis overpredicted the measured response at the midheight and underpredicted the measured response at the springline. This is consistent with the trends observed in the 3DCM analysis, which is discussed in much more detail in Chapter 6. Note that for SOLs where axisymmetric analysis is inapplicable, only a “2000” results curve is plotted.

4.2 Rebar Comparisons

Rebar comparisons are made in Figures 4-5 through 4-9.

SOLs 16, 17, 18, 19, 20, and 21. This series of locations compares inner and outer meridional rebars in a series near the base of the cylinder wall, which is a zone of significant flexure and shear. In general, the strains in the inner rebar layers agree fairly well with analysis and the outer rebar layers show more noticeable differences. The main reason for this may be simply that the outer rebar strains have quite small amplitudes, since the wall’s vertical flexure tends to add tension on the inside and compression on the outside surfaces. It is often difficult to match a test measurement of very small amplitude (i.e., percentage differences may appear large, while in absolute terms, the differences are quite small). The predicted trends do appear to be reasonable, however. It should also be noted that the outer rebars that were gaged are likely to be very close to the neutral axis of bending in the section. Thus, if the analytical prediction of neutral axis location is only off by a few millimeters, the strain predictions immediately adjacent to this could be at large variance with the test model, or even have opposite signs. The inside bars are sufficiently far from the neutral axis of bending to prevent such sensitivity.

SOLs 22 and 23. These locations compare hoop and meridional rebar strain at the cylinder midheight. Agreement with analysis is generally good, although the hoop bar strains late in the test tend to be underpredicted. This difference has been attributed to rebar gage effects, as discussed in Chapter 3. The argument is that the analysis agrees well on radial displacements at this location, so by kinematics, it follows that the prediction of global hoop strain at this location is also good.

SOLs 24, 25, and 26. These locations compare a hoop rebar and an inner and outer meridional rebar at the springline. Again, the hoop rebar strain and inner rebar strain predictions show similar trends to the measurements, while the outer rebar strain is significantly overpredicted. The same observations made at the wall-base juncture apply here. Due to the radial stiffness differential between cylinder and dome, the springline is once again a point of significant meridional bending, with tension on the inside and compression on the outside. (This flexural component is in addition to the underlying tension caused by the $pr/2t$ cylinder stress.) As an indicator, the measurements for the inside meridional bar reaches .0013 by the end of the test (3.3 Pd), while the measurement for the outside bar only reaches .00022.

SOL 27, 28, and 29. These rebar strain measurements in inner and outer hoop and meridional rebar show good agreement to analysis for the hoop rebar, but poor agreement for both meridional rebar. This observation and the dome displacement observation clearly show that the analysis overpredicted vertical deformations in the dome.

SOL 30, 31, 32, and 33. These comparisons are for the meridional (inner and outer) and hoop rebar at the 90 degree buttress. The comparisons of inner meridional rebar strain at the base of the wall are good (to within about 25%), while for the outer meridional rebars they are significantly overpredicted. The previous argument about local bending and proximity to the neutral axis may also apply here. The buttress hoop rebar strain at cylinder midheight is also significantly overpredicted.

4.3 Liner Strain Comparisons

Liner strain comparisons are made in Figures 4-10 through 4-13.

SOL 34, 35, 36, and 37. The first four comparisons are for strains near the wall-base juncture at azimuth 0 degrees and azimuth 135 degrees, inside and outside liner surface. At elevation 0.01 meters, the analysis shows a similar trend to the data, but overpredicts the magnitude. This comparison may be highly influenced by gage placement and by the location for extracting the analytical data. The location is within just a few millimeters of a sharp stiffness discontinuity. There is also some evidence in the test data that the liner base anchor may have begun to pull out of the concrete; if this indeed occurred, it would lessen the severity of the stiffness discontinuity and the meridional strains near the wall-base juncture. Unfortunately, the liner strain gages at azimuth 135 degrees were damaged by welding operations during the PCCV model construction, so the evidence supporting this hypothesis is limited. The meridional and hoop strain comparisons at 0.25 meters elevation show fair agreement. It is interesting to note that the hoop gages at 0.25 meters elevation show positive values during prestress and a negative trend during pressurization. This is counter to the rest of the cylinder and is likely caused by the reverse in vertical curvature that takes place at this elevation, and apparently is a Poisson Effect caused by wall flexure.

SOL 38 and 39. Hoop and meridional strain comparisons at cylinder midheight show similar trends. At approximately 2.8 Pd, the test data indicates significant yielding of the liner in the hoop direction. The analysis results also demonstrate a change in stiffness at this pressure, but not so sharply. Note that the analysis results are purely global response, taken from axisymmetric analysis, while liner strain measurements can be influenced by local details on the liner, such as proximity to stiffeners, weld seams, or even proximity to a concrete crack behind the liner.

SOL 40, 41, and 42. Hoop and meridional strain comparisons at the springline show good agreement (within ~10%) for hoop behavior, but the meridional strain, which is likely influenced significantly by vertical bending behavior, is overpredicted by analysis. This is consistent with the observed trend that vertical deformations in the dome were overpredicted by analysis. The meridional strain comparison at the dome apex shows fairly good agreement (within ~25%).

SOL 43 and 44. These locations compare meridional and hoop strain near the 90 degree buttress at the cylinder midheight. The hoop strain compares very closely, while the meridional strain is overpredicted.

SOL 45 and 46. These locations are intended to capture strain concentration locations near the thickened insert plate of the E/H and A/L, respectively. While at pressures lower than about 2.7 Pd, there is fair agreement with the measurements, clearly the local analyses predicted a strong strain concentration that did not occur in the test. This fundamental difference between the analytical predictions and the test is discussed later in detail.

SOL 47. This location is on the liner at the basemat, 100 mm inside the cylinder. While the strain comparisons at least show a similar trend, there are large differences in magnitude. However, the measured data and the analysis predictions are small, so quantities being compared are also small.

4.4 Tendon Comparisons

Tendon gage versus analysis (pressure histories) comparisons are made in Figure 4-14 and 4-15

SOL 48, 49, and 54. These locations compare strain and load cell force in two vertical (hairpin) tendons. The comparisons of strain are fairly good, while the comparison of load cell force is somewhat overpredicted.

SOL 50, 52, 53, and 55. These locations compare strain for hoop tendon H53 (mid-tendon, near buttress, and between E/H and A/L) and load cell force for hoop tendon H53. The strain comparisons generally show good agreement, except near the buttress, where the analysis overpredicted. The load cell force also shows reasonably good agreement.

An overview of comparisons of analytically predicted to actual tendon behavior is provided in Figures 4-16 through 4-22. These figures combine the test measurement information from load cells and the average of the wire strain gages.

The wire strain gage data was converted to force by SNL using the stress versus strain curves for the total tendon. These were provided in Ref. [8]. The analysis data for the hoop tendon comparisons is from the pretest 3DCM analysis. More hoop tendon comparisons are provided in Chapter 6 in the discussion on the 3DCM. The reader is also directed to those Figures (6-3 to 6-6) for the following discussion.

The hoop tendon data provides the following insights into the PCCV hoop tendon behavior and the predictions of behavior provided by the pretest 3DCM analysis.

1. The initial prestress anchor forces put into the pretest model have the same shape as the basic design friction assumption and roughly 9% lower magnitude. This 9% reduction from design values was incorporated to address the long term losses that occurred between initial seating and the LST. This strategy for initial anchor force, on average, agrees well with the tendon anchor force measurements taken just prior to LST pressurization. These observations are based on comparing the "Analysis @ 0.000" anchor force data to the data points at "9/26/00 10:03 0.00." At H11, H35, H53, H67, and H68, the zero pressure anchor forces are generally in good agreement with the analysis, and are generally 5% to 10% lower than the design assumptions.
2. The shape of the tendon stress distribution at the start of the LST also shows a similar trend compared with measurements, implying that the angular friction and anchor set modeling assumptions at the start of the test (which were made based on standard design assumptions) were reasonable. There is some scatter in the level of agreement, however. Tendon H11 shows about 20% less angular friction loss than assumed, while H35, H53, and H67 show much closer agreement. H68 also shows some scatter in the measured friction loss profile.
3. Some of the hoop tendon stress distributions during pressurization showed poor agreement with the pretest analysis. This is based on comparing the analysis curve at 1.17 MPa (3.0 Pd) to the data at 1.162 MPa. While H11 and H53 show fair agreement at the "interior" gages, the anchor forces are significantly over-predicted. Higher on the cylinder (H53 and H67), the interior gages are underpredicted *and* the anchor forces are overpredicted.
4. The cylinder hoop tendon data, in total, shows evidence of changes in friction orientation (i.e. tendon slipping) during pressurization. H53 and H67 show this particularly well. The data indicate that the shape of the tendon stress profile changes during pressurization. The total force increase on the plot is equivalenced to a hoop strain derived from the radial expansion of the cylinder (i.e., H53 $\Delta\epsilon=0.48\%$ and H67 $\Delta\epsilon=0.45\%$, while hoop strain from radial expansion is significantly lower at 0.35% and 0.37%). This implies that portions of the tendons are slipping to accommodate the higher deformation at other azimuths.

The vertical tendon data (Figures 4-17 through 4-22) provide the following insights.

1. As with the hoop tendons, there was about 8% to 10% loss occurrence between the initial prestressing and the start of the LST caused by long term effects and by the System Functionality Test (SFT) and SIT. This is evidenced in Figures 4-17 and 4-18 for tendon V37, Figures 4-19 and 4-20 for V46, and Figures 4-21 and 4-22 for V85. Only V85 showed significant friction losses above the springline, and the other two gaged vertical tendons showed only about half of the friction loss in the dome than what was assumed by the designers and incorporated in the analysis.
2. Comparisons with the axisymmetric analysis show that assuming no friction along the straight portion of the tendon and much smaller friction in the dome would provide improved simulation of the vertical tendon behavior. (As discussed in Chapter 5, this justifies returning to the 1999 axisymmetric analysis as the better vertical tendon simulation.)

4.5 Wall-Base Juncture Shear Behavior

Another local area of the PCCV model that was studied in detail was the wall-base juncture [1]. Some relatively large concrete strains, driven by shear and flexure were predicted to occur as shown in Figure 4-23, but no failure associated with the shear and flexure mechanism was predicted until $P > 4.0$ Pd, much larger than the 3.3 Pd reached in the LST. Nevertheless, it is of interest to compare special rebar and liner strain measurements taken in the wall-base juncture area

to the pretest analysis. Since it was concluded during the posttest work that the 1999 pretest model provided the more appropriate simulation of the true vertical tendon stresses, and since this modeling detail has significant influence on the wall-base juncture behavior, the comparisons to the test are only made to the 1999 predictions.

Because this area was identified as having a high potential for large strains and liner tearing in the preliminary analysis, a significant effort was made to instrument the liner and wall at several azimuths. Specially fabricated ‘gage bars’ (not part of the model reinforcing) were installed through the thickness of the wall in an attempt to monitor the local strain distribution. Unfortunately, many of the gages installed on the liner and the gage bars were damaged during construction or subsequent water penetration and were not functional during the LST. The typical arrangement of liner strain gages at the wall-base juncture are shown in Figure 4-24. The ‘gage bar’ strain gages installed in the area are shown schematically in Figure 4-25. Fortunately, a large number of gages survived at the 135 azimuth, which was chosen to represent the axisymmetric behavior of the model. During the test, many of these gages were monitored in real time using this display screen. The gage numbering shown on the screen is tabulated in Table 4-2. A labeling scheme that facilitates analysis versus test comparisons is shown in Figure 4-26.

Table 4-2. Gage Identification for the Basemat Junction Display Screen

Number on Screen	Gage Name
1	GB-M-Z1-05
2	GB-M-Z1-10
3	RS-R-Z2-02
4	GB-M-Z1-15
5	GB-M-Z1-20
7	GB-M-Z1-09
8	RS-R-Z2-01
9	GB-M-Z1-14
10	GB-M-Z1-19
11	GB-M-Z1-03
13	RS-R-Z-1-02
14	GB-M-Z1-13
15	GB-M-Z1-18
18	RS-R-Z1-01
20	GB-M-Z1-22
24	GB-M-Z1-21
25	RS-M-Z2-01
26	RS-M-Z2-02
27	RS-M-Z1-01
28	RS-M-Z1-02
38	RS-M-Z0-13
39	RS-M-Z0-14

Comparisons between wall-base area liner and rebar strain gages are provided in Figures 4-27 through 4-49. The analysis data was zeroed to the experimental measurements, but a specific gage had to be selected for this zeroing. Which gage was selected is clear from observing which data/gage history curves “match” at P=0. The liner strain comparisons near the base of the wall (Figures 4-27 through 4-32) show similar trends to the analysis. When two liner positions are shown (i.e., B, C, etc.), this is provided to straddle strain gage locations that occur between the two analysis liner locations. Thus, often a particular gage will agree well with one of the pair of analysis points or with an average of the two. In general, the agreement shows that the wall-base liner behavior was well simulated by the analysis.

The level of correlation with the rebar gages (Figures 4-33 through 4-49) was not as good, but such was the case in comparing "free-field" rebar strain data, as well. As described in Chapter 3, in general the rebar strain measurements, upon reaching yield ($\epsilon \cong 0.002$), tend to significantly overstate the actual strain. It is also quite difficult to pinpoint an analysis location that coincides with a rebar strain gage location. Nevertheless, some of the gages show quite good agreement with analysis. These include Axisymmetric Position D compared to GB-M-A1-04 (Figure 4-34), midway

between Positions E and J versus GB-M-Z1-05 (Figure 4-35), Position D vs. GB-M-Z1-10 (Figure 4-38), and Position V (in flexural compression) vs. GB-M-Z1-22 (Figure 4-43) and Position W vs. GB-M-Z1-18 (Figure 4-44). These are all vertical bars, indicating that the analysis captured the wall-base flexure behavior reasonably well.

Figures 4-46, 4-47, 4-48, and 4-49 compare stirrup strains. In general, these would be extremely difficult to match with analysis because stirrup strains are so influenced by the precise location of a major shear crack. Nevertheless, Figure 4-48 for stirrup location AB (shown in yellow on Figure 4-26, at about Elev. 12 inches) shows similar behavior to the gage measurements, indicating that shear behavior was simulated reasonably well. Note that all of the stirrup strains (measured and predicted) are well below yield, indicating that at the end of the LST (3.3 Pd), the model is far from developing shear failure.

4.6 Failures: Predicted and Observed

The 3DCM model predicted rupture of hoop tendons near the E/H with strains exceeding 5% at a model pressure of about 3.5 Pd[1]. However, this mode was predicted to be precluded by the liner tearing and leakage failure mode associated with the local models. The failure pressure at which a local analysis computed effective plastic strain that reached the failure strain of approximately 16% was 3.2 Pd, or 1.3MPa. The location for this liner-tearing failure was near the E/H, adjacent to a vertical liner anchor that terminated near the liner insert plate transition. Other local models showed other candidate liner tear locations, several of which were predicted to occur during the pressure range 3.2 Pd to 3.5 Pd, if they were not precluded first by the growth of the first tear and subsequent depressurization of the vessel. Significant candidate tear locations were also predicted near weld seams with hoop stiffener rat-holes, for example, near the 90-degree buttress where hoop strains are elevated due to circumferential bending. Failure at such locations was predicted to occur shortly after the E/H location.

As discussed in detail in Chapter 8, this last type of tear location was the predominant failure mode observed in the LST. Liner tears occurred in 16 locations, and there is evidence (acoustic and pressure/leak-rate measurements) supporting approximately 2.5 Pd as the pressure of the first tear initiation. Although predicted as a general failure mode, the specific location and pressure were not predicted. The following chapters discuss and present conclusions as to why these specific tear events were not explicitly predicted and why the strain predictions at the highest strain location of the pretest analysis was significantly overpredicted.

While the scope and objectives of the pretest analysis work for the 1:4-scale PCCV did not include a formal probabilistic risk assessment of the failure (leakage) pressure prediction, the final probability of liner tearing/leakage versus pressure was described in probabilistic terms with reference to the final list of candidate tearing locations. Combining probabilities and locations produced the following leakage pressure predictions and confidence intervals, which were published prior to the test. Best estimate (Probability = 0.5), $P_{\text{leakage}}=3.2 \text{ Pd}=1.3 \text{ MPa}$; upper bound (Probability = 0.9), $P_{\text{leakage}}=3.5 \text{ Pd}=1.4 \text{ MPa}$; lower bound (Probability = 0.1), $P_{\text{leakage}}=2.75 \text{ Pd}=1.1 \text{ MPa}$. Referring back to the pretest report where these were derived, the first leakage occurred below the 10% probability. This was an unacceptable prediction, but is easily explained by the presence of extensive flaws near weld seams. Such flaws probably can and should be considered in containment probabilistic calculations. Discussion of these issues as they relate to the test observations is also provided in later chapters.

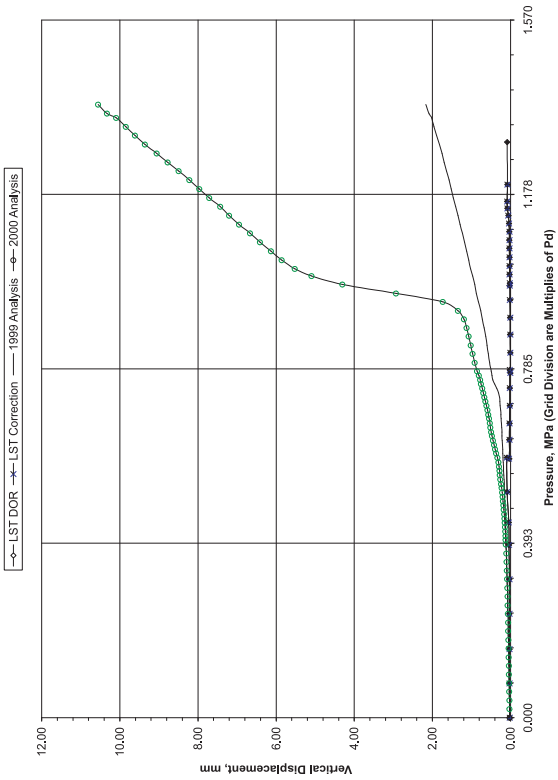
4.7 Discussion and Conclusions of Analysis vs. Test Comparisons

A good overview of the test versus analysis comparisons in this chapter can be made by combining the response history information into deformed shape comparison plots. This information is provided in Figures 4-50 through 4-53. The plots show displaced shape along a horizontal slice (at Elev. 4.68 m) and three vertical slices (at 135, 324, and 90 degree azimuths) at various pressures compared to analysis. The overall conclusions from these and other comparisons in this chapter are as follows.

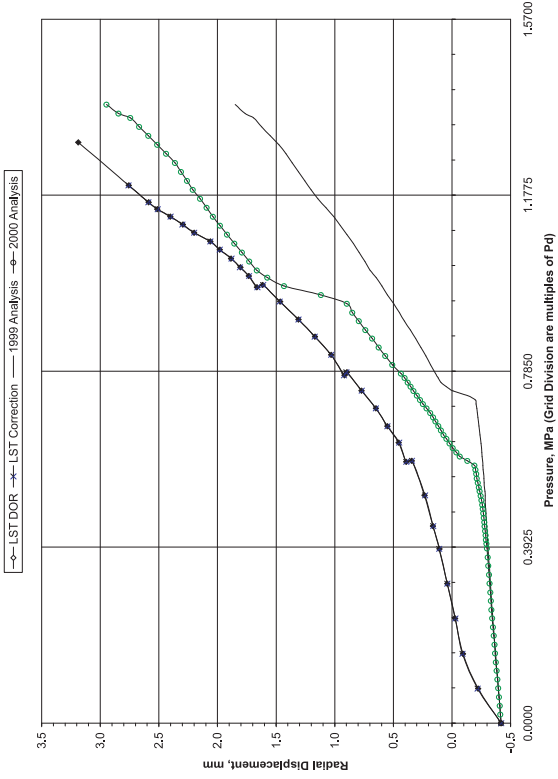
- Radial displacements were well predicted by global axisymmetric analysis, but dome and overall vertical displacements were significantly overpredicted.

- Based on the gages available, the wall-base juncture behavior appears to have been well predicted by the detailed wall-base juncture (axisymmetric) modeling.
- Maximum pressure (187.9 psig (3.30 Pd), which was primarily a function of the onset of global yielding, was closely predicted by analysis, but the predicted failure mode did not manifest itself. Note that the maximum pressure achieved during the LST was also limited by the capacity of the pressurization system to balance the increasing leak rate after functional failure occurred.
- An initial small leak occurred at 2.5 Pd that was not predicted by analysis, but this probably occurred due to defects associated with weld seam repair.
- Average radial displacement reached 23mm at 3.3 Pd
 - Average hoop strain = 0.0040 (well predicted by global analysis).
- Maximum radial displacement at E/H = 29mm at 3.3 Pd
 - Equivalent hoop strain = 0.0054 (reasonably well predicted by 3DCM, but prediction of some displacements at other azimuths — like the buttresses — was poor).

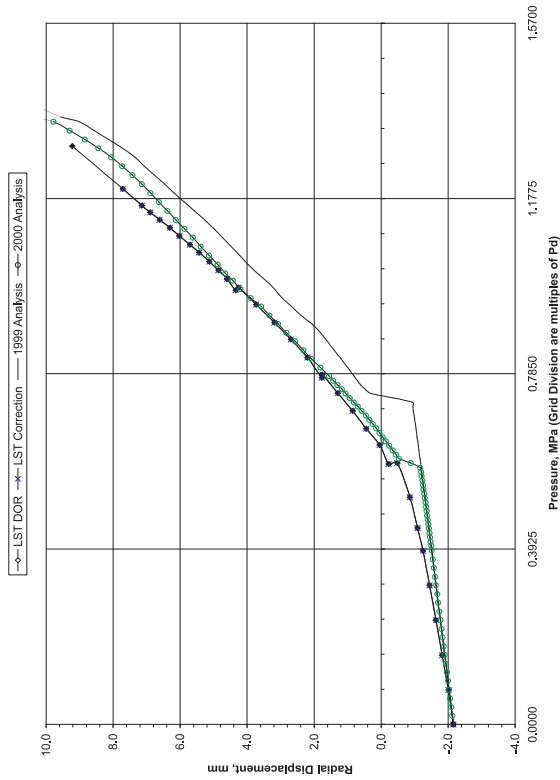
Standard Output Location #1. Azimuth: 135 Degrees, Elevation: 0.00 Meters, Top of Basemat



Standard Output Location #2. Azimuth: 135 Degrees, Elevation: 0.25 Meters, Base of Cylinder



Standard Output Location #3. Azimuth: 135 Degrees, Elevation: 1.43 Meters, Base of Cylinder



Standard Output Location #4. Azimuth: 135 Degrees, Elevation: 2.63 Meters, Base of Cylinder

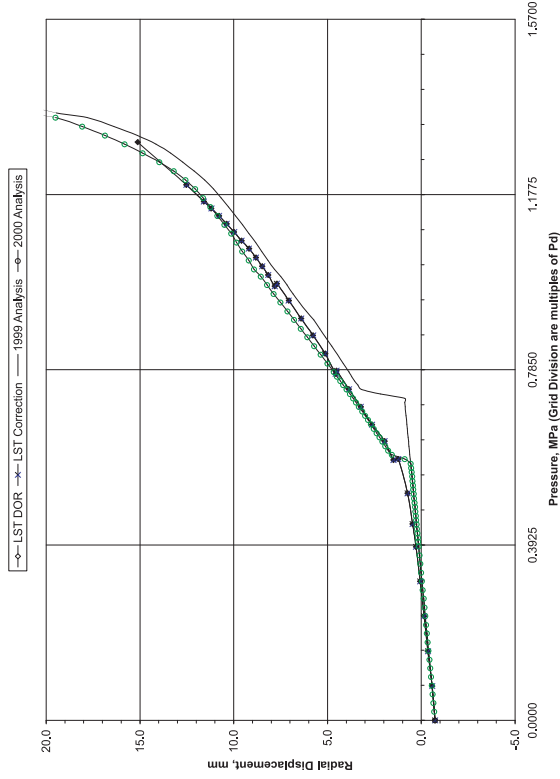
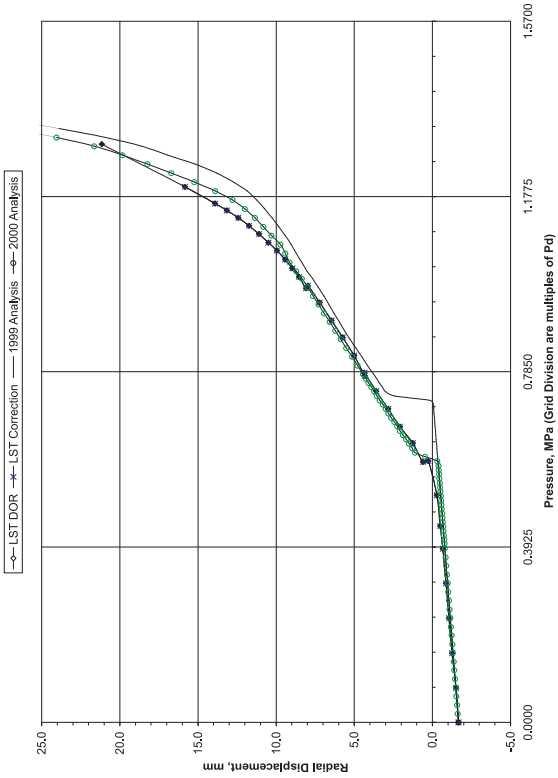
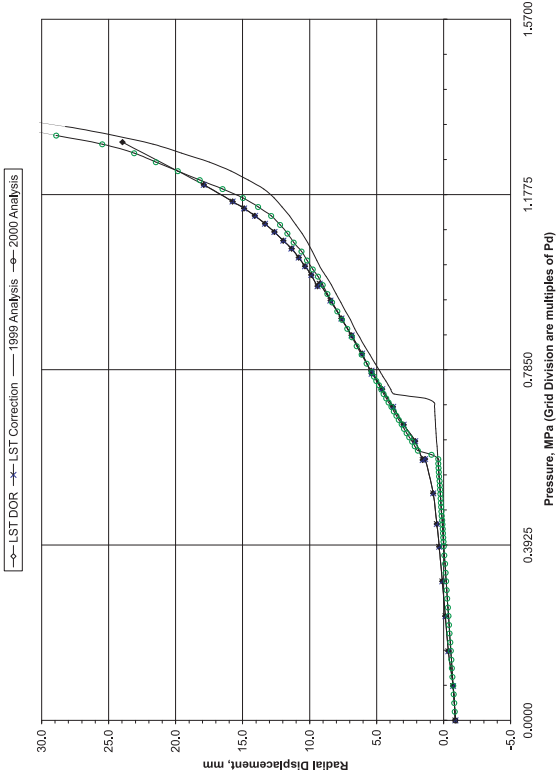


Figure 4-1. Comparisons at Standard Output Location 1, 2, 3, and 4

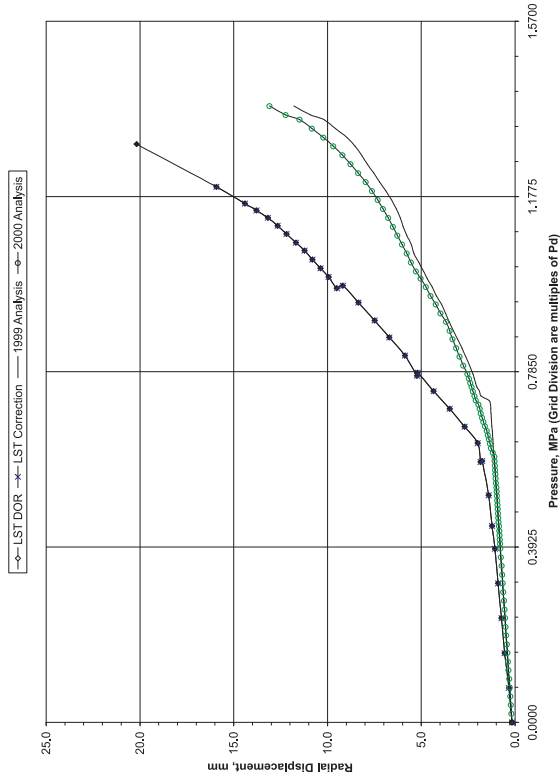
Standard Output Location #5. Azimuth: 135 Degrees, Elevation: 4.68 Meters, E/H Elevation



Standard Output Location #6. Azimuth: 135 Degrees, Elevation: 6.20 Meters, Approximate Midheight



Standard Output Location #7. Azimuth: 135 Degrees, Elevation: 10.75 Meters, Springline



Standard Output Location #8. Azimuth: 135 Degrees, Elevation: 10.75 Meters, Springline

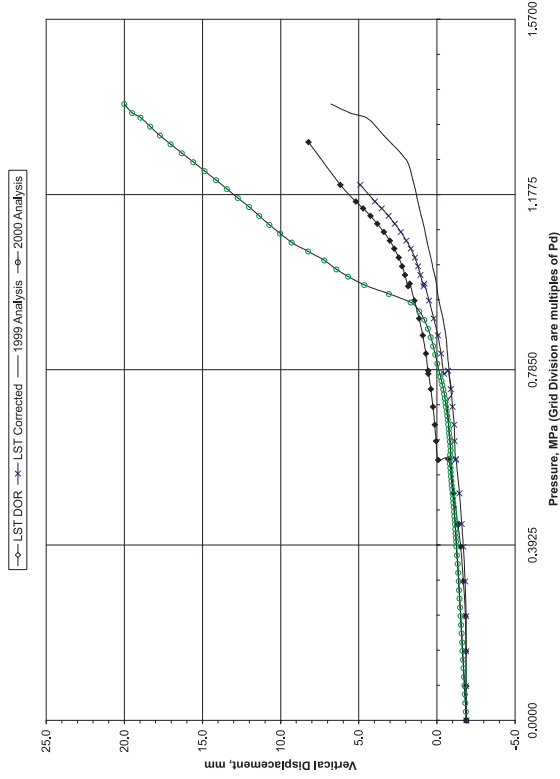
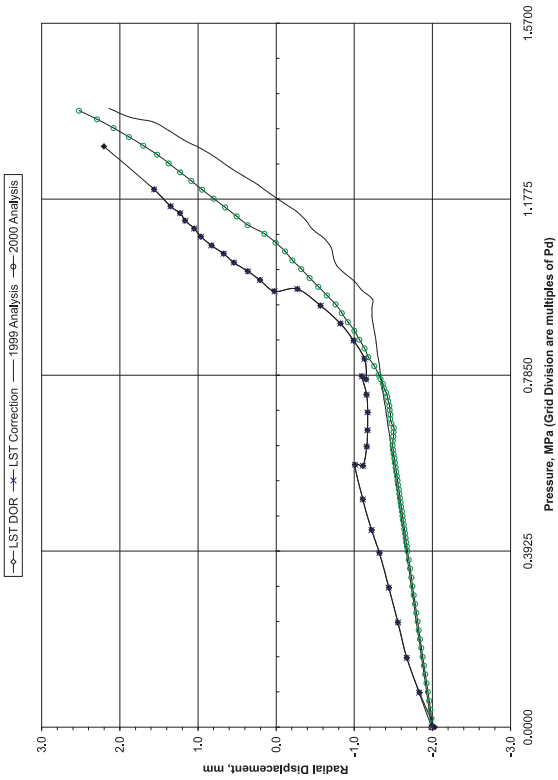
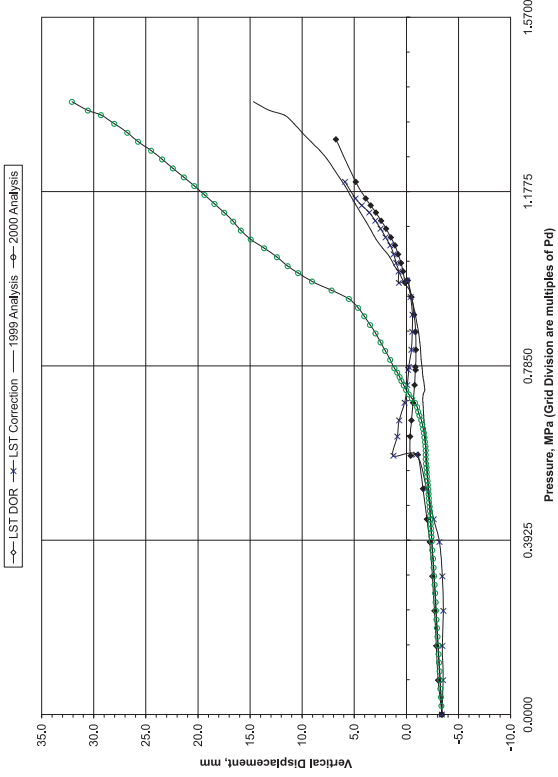


Figure 4-2. Comparisons at Standard Output Location 5, 6, 7, and 8

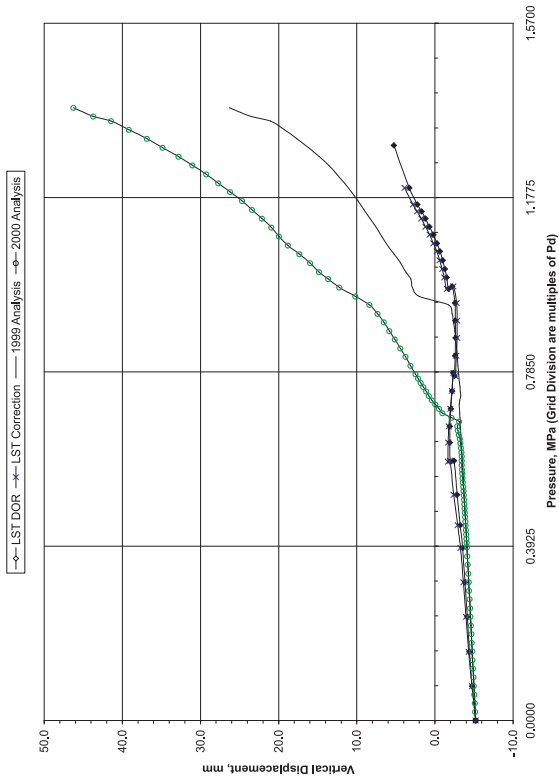
Standard Output Location #9. Azimuth: 135 Degrees, Elevation: 14.55 Meters, Dome 45 deg



Standard Output Location #10. Azimuth: 135 Degrees, Elevation: 14.55 Meters, Dome 45 deg



Standard Output Location #11. Azimuth: 135 Degrees, Elevation: 16.13 Meters, Dome Apex



Standard Output Location #12. Azimuth: 90 Degrees, Elevation: 6.20 Meters, Midheight at Buttress

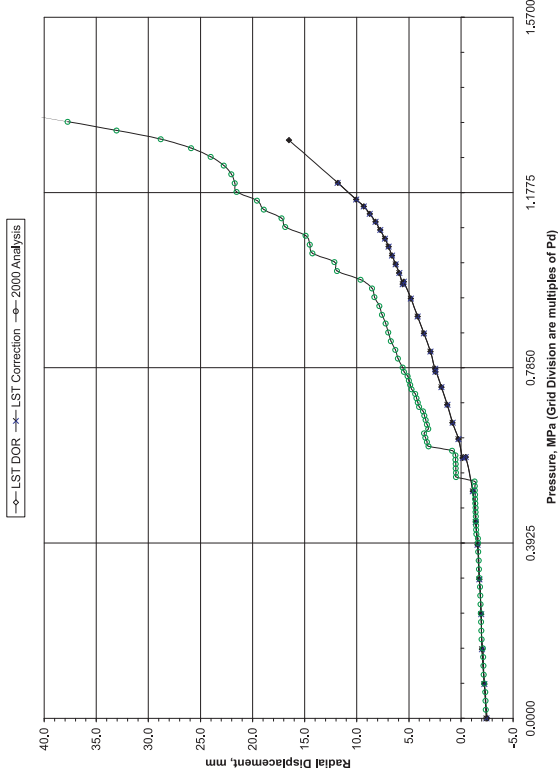
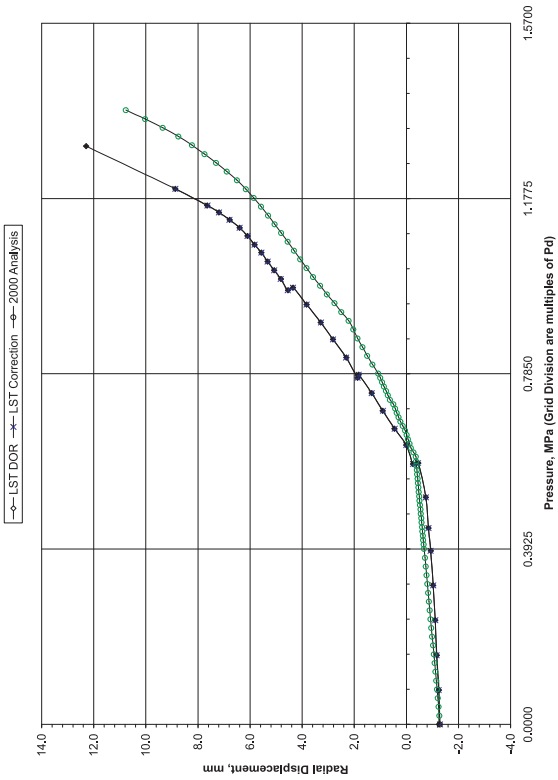
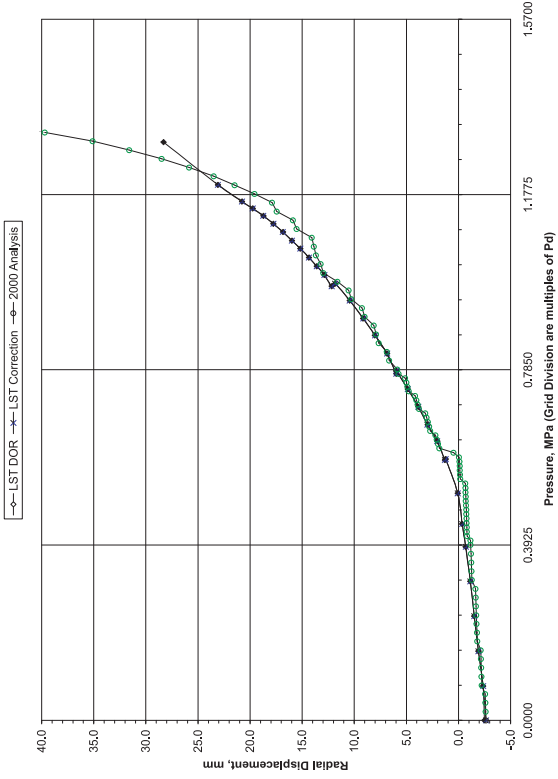


Figure 4-3. Comparisons at Standard Output Location 9, 10, 11, and 12

Standard Output Location #13. Azimuth: 90 Degrees, Elevation: 10.75 Meters, Springline at Buttress



Standard Output Location #14. Azimuth: 324 Degrees, Elevation: 4.675 Meters, Center of E/H



Standard Output Location #15. Azimuth: 62 Degrees, Elevation: 4.525 Meters, Center of ALL

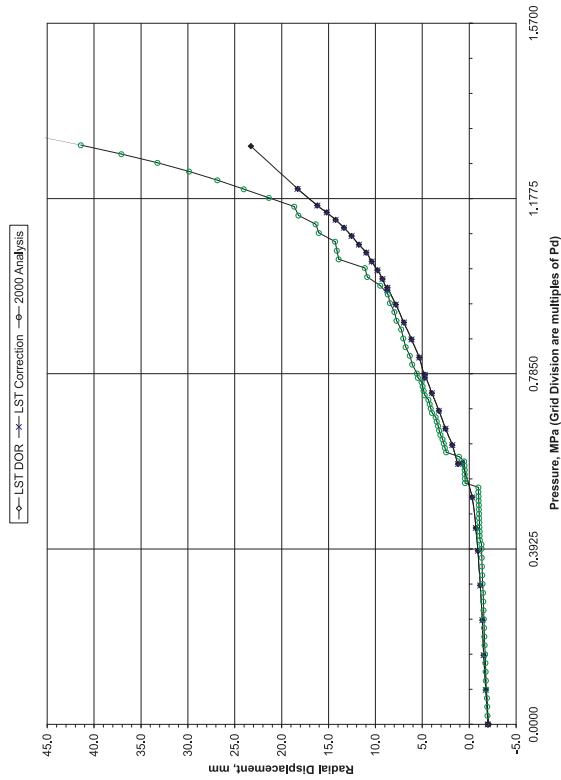
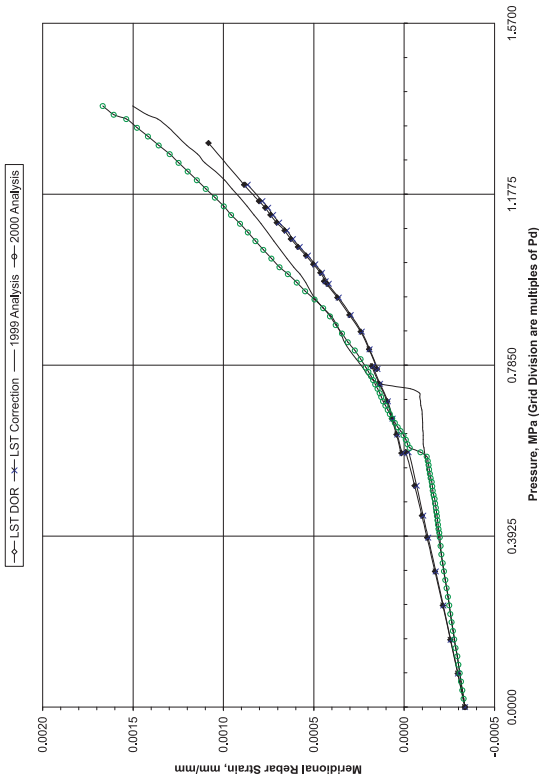
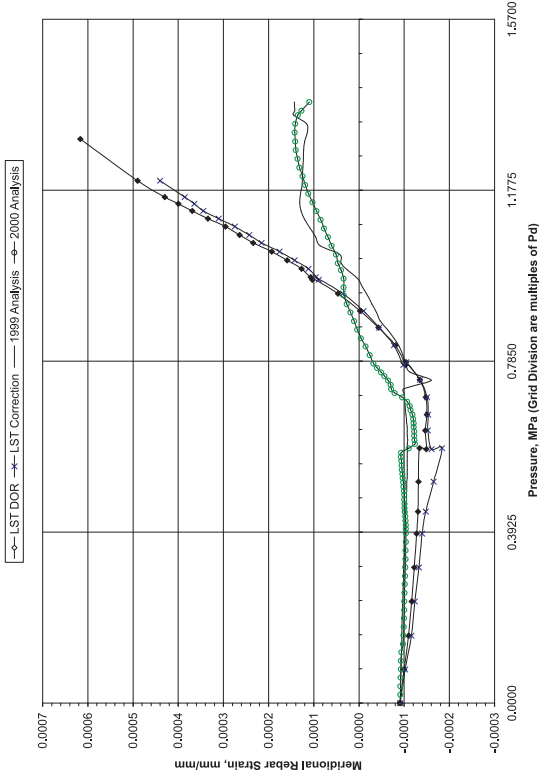


Figure 4-4. Comparisons at Standard Output Location 13, 14, and 15

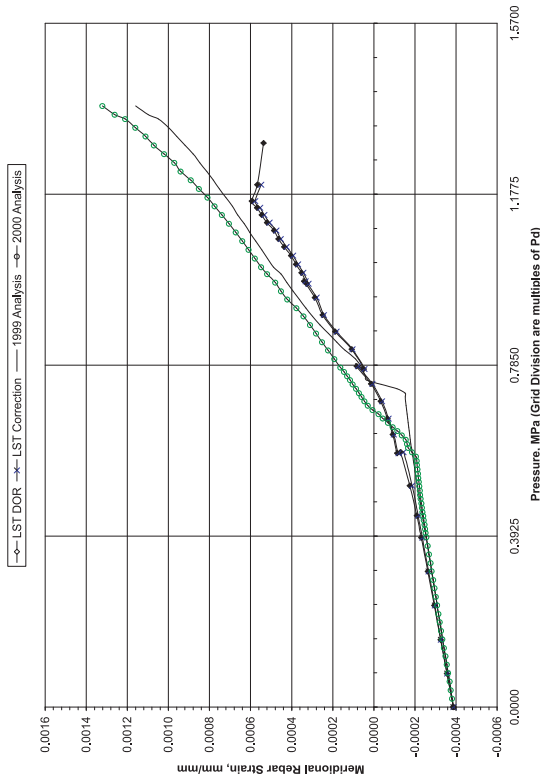
Standard Output Location #16. Azimuth: 135 Degrees, Elevation: 0.05 Meters, Inner Rebar Layer, Base of Cylinder



Standard Output Location #17. Azimuth: 135 Degrees, Elevation: 0.05 Meters, Outer Rebar Layer, Base of Cylinder



Standard Output Location #18. Azimuth: 135 Degrees, Elevation: 0.25 Meters, Inner Rebar Layer, Base of Cylinder



Standard Output Location #19. Azimuth: 135 Degrees, Elevation: 0.25 Meters, Outer Rebar Layer, Base of Cylinder

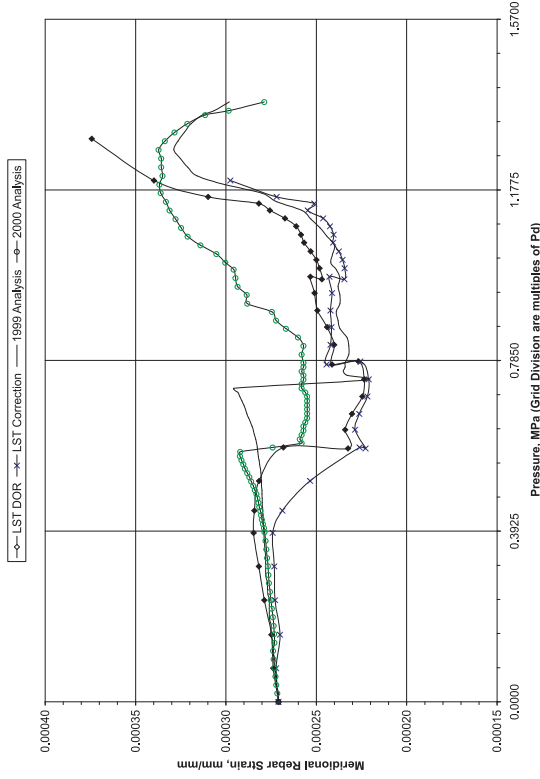
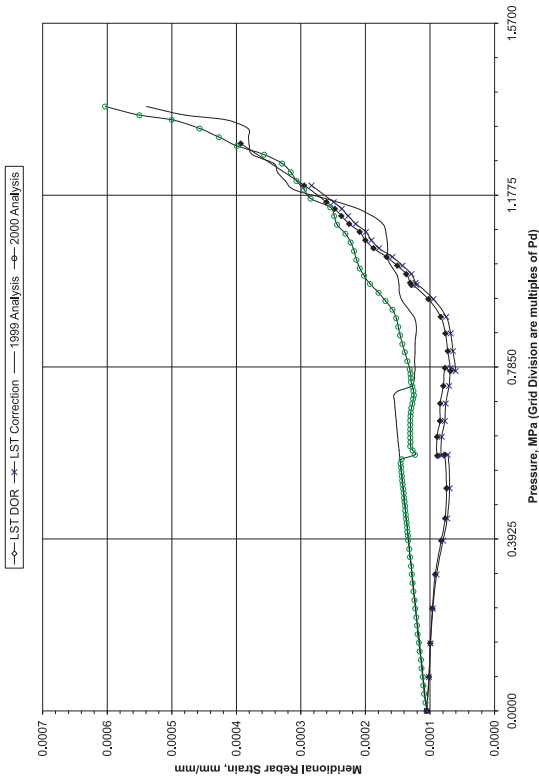
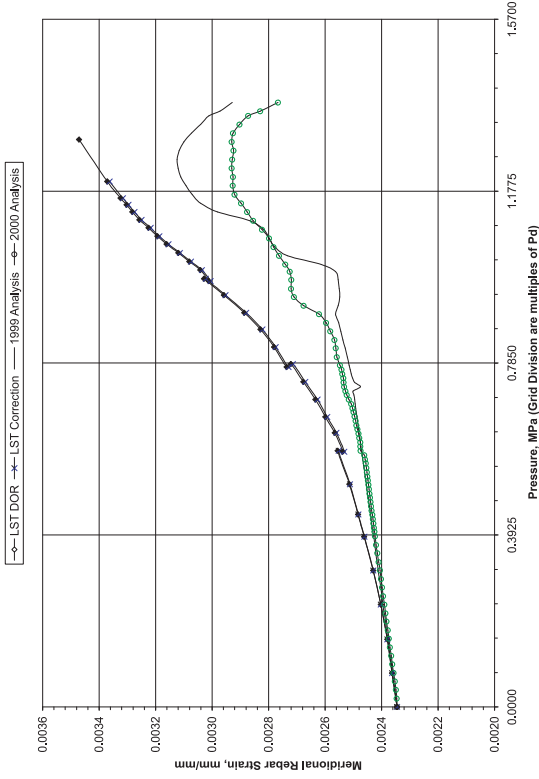


Figure 4-5. Comparisons at Standard Output Location 16, 17, 18, and 19

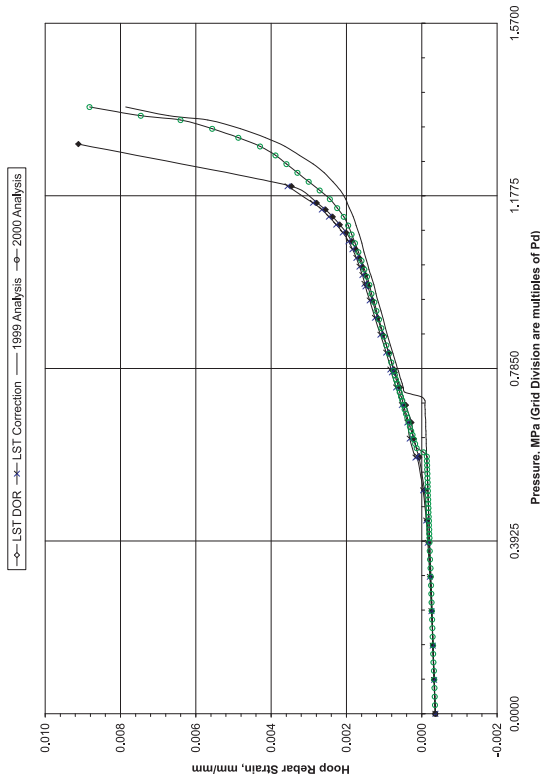
Standard Output Location #20. Azimuth: 135 Degrees, Elevation: 1.43 Meters, Inner Rebar Layer, Base of Cylinder



Standard Output Location #21. Azimuth: 135 Degrees, Elevation: 1.43 Meters, Outer Rebar Layer, Base of Cylinder



Standard Output Location #22. Azimuth: 135 Degrees, Elevation: 6.20 Meters, Outer Rebar Layer, Midheight



Standard Output Location #23. Azimuth: 135 Degrees, Elevation: 6.20 Meters, Outer Rebar Layer, Midheight

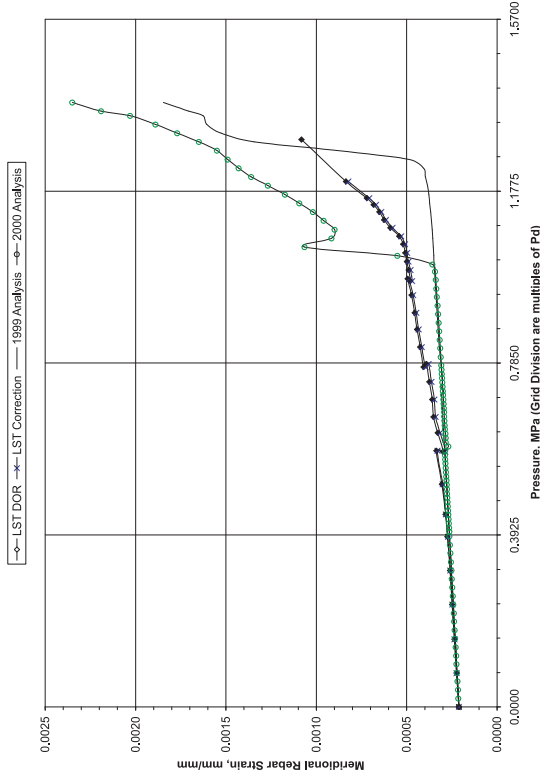
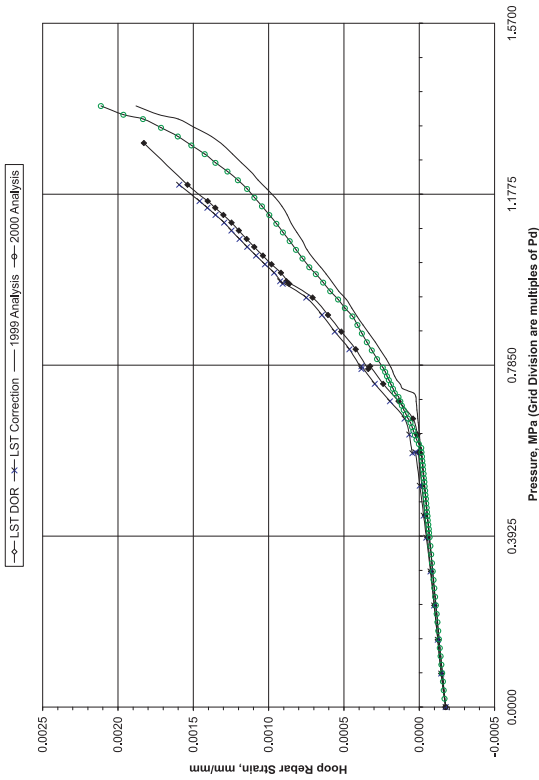
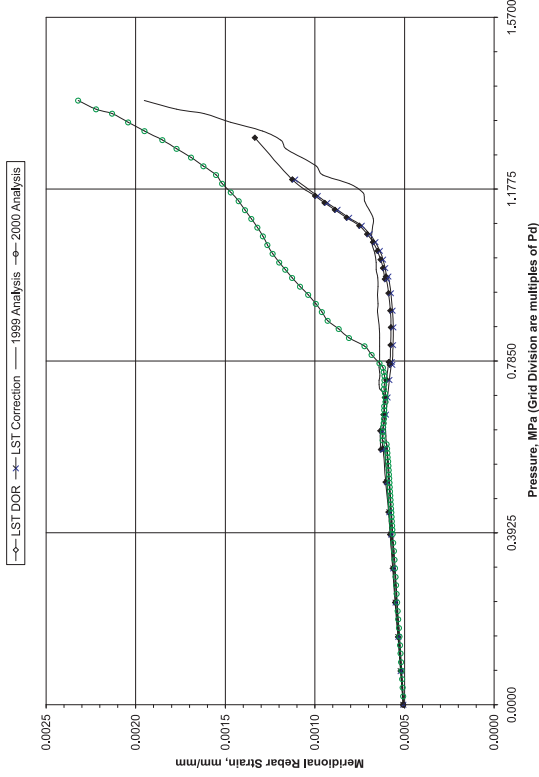


Figure 4-6. Comparisons at Standard Output Location 20, 21, 22, and 23

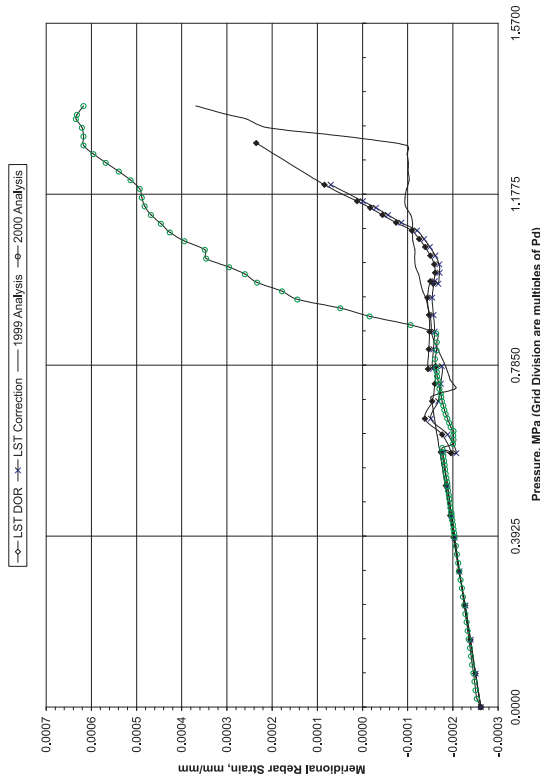
Standard Output Location #24, Azimuth: 135 Degrees, Elevation: 10.75 Meters, Outer Rebar Layer, Springline



Standard Output Location #25, Azimuth: 135 Degrees, Elevation: 10.75 Meters, Inner Rebar Layer, Springline



Standard Output Location #26, Azimuth: 135 Degrees, Elevation: 10.75 Meters, Outer Rebar Layer, Springline



Standard Output Location #27, Azimuth: 135 Degrees, Elevation: 14.55 Meters, Outer Rebar Layer, Dome 45 deg

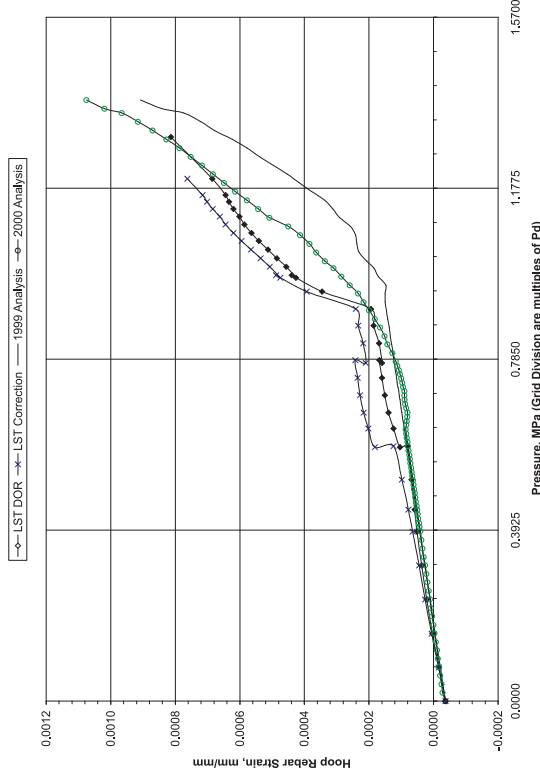
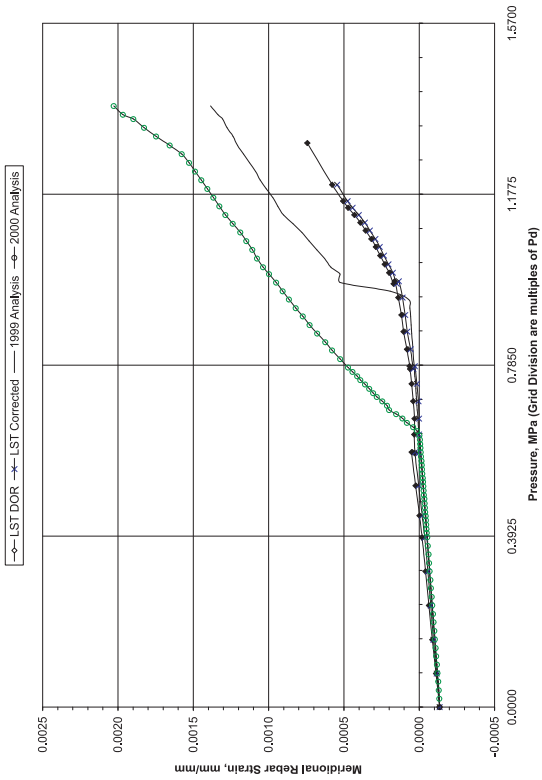
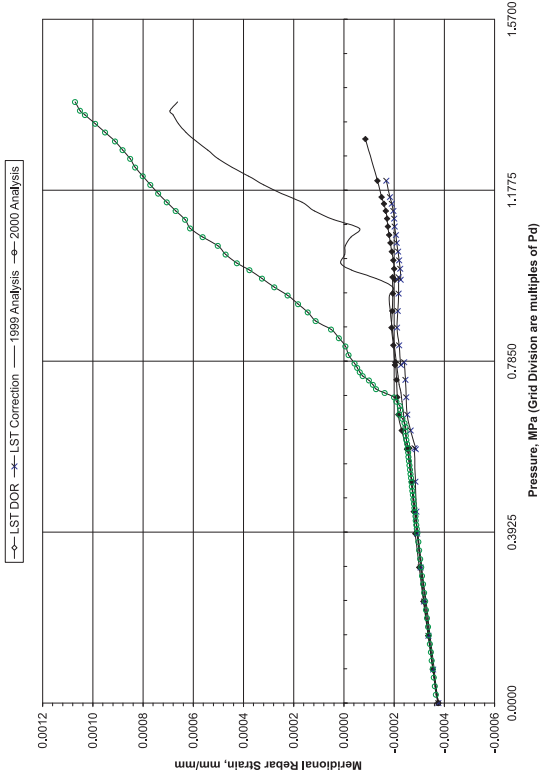


Figure 4-7. Comparisons at Standard Output Location 24, 25, 26, and 27

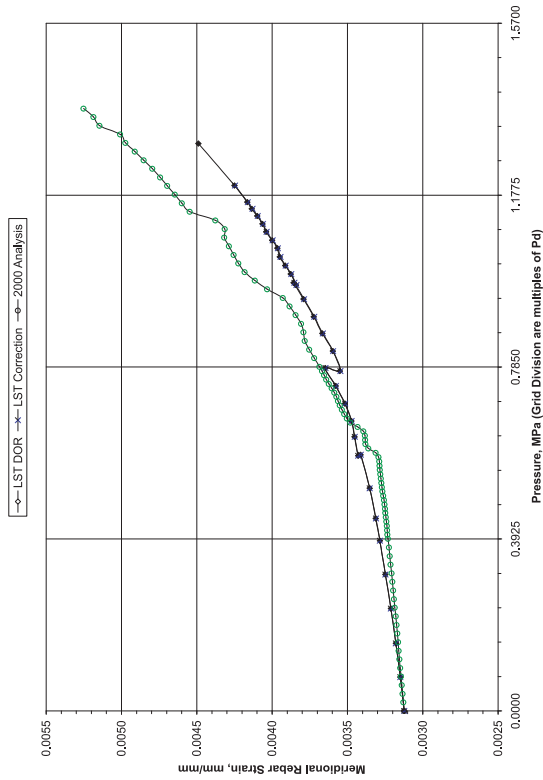
Standard Output Location #28. Azimuth: 135 Degrees, Elevation: 14.55 Meters, Inner Rebar Layer, Dome 45 deg



Standard Output Location #29. Azimuth: 135 Degrees, Elevation: 14.55 Meters, Outer Rebar Layer, Dome 45 deg



Standard Output Location #30. Azimuth: 90 Degrees, Elevation: 0.05 Meters, Inner Rebar Layer, Base of Cylinder at Buttress



Standard Output Location #31. Azimuth: 90 Degrees, Elevation: 0.05 Meters, Outer Rebar Layer, Base of Cylinder at Buttress

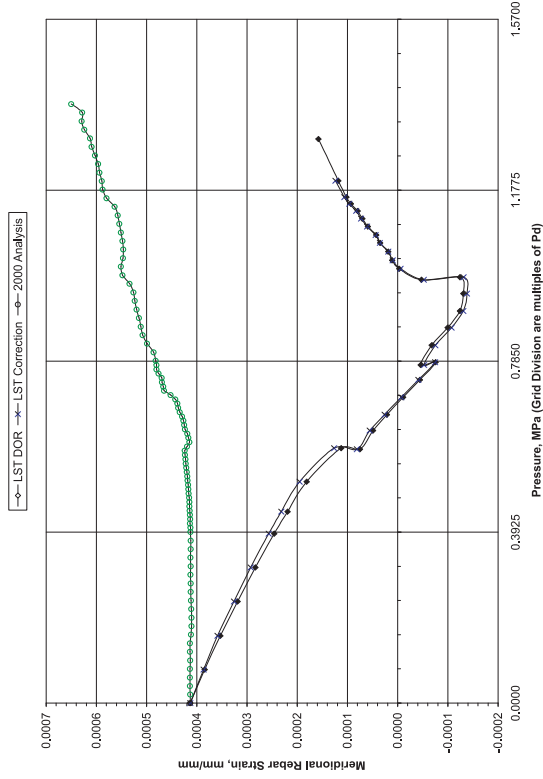
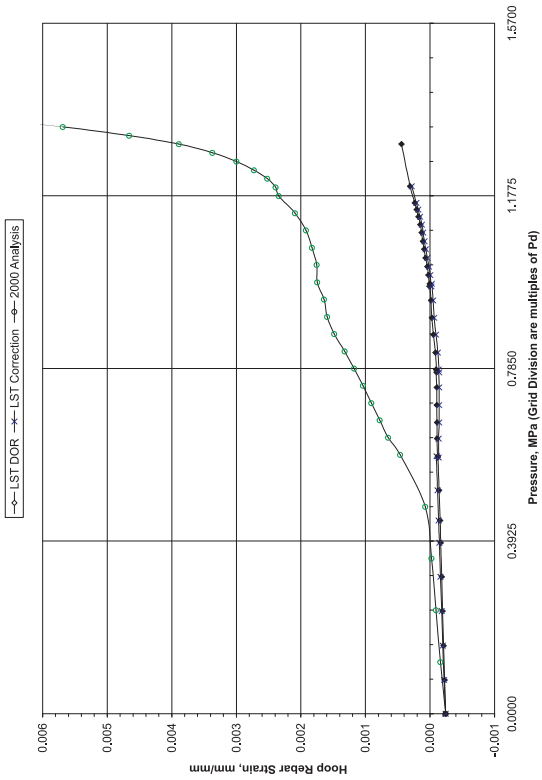


Figure 4-8. Comparisons at Standard Output Location 28, 29, 30, and 31

Standard Output Location #32. Azimuth: 90 Degrees, Elevation: 6.20 Meters,
Outer Rebar Layer, Midheight at Buttress



Standard Output Location #33. Azimuth: 90 Degrees, Elevation: 6.20 Meters,
Outer Rebar Layer, Midheight at Buttress

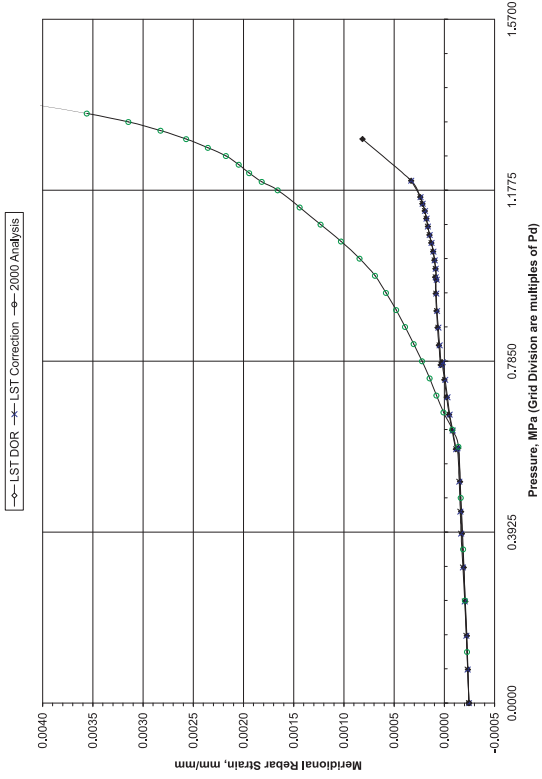
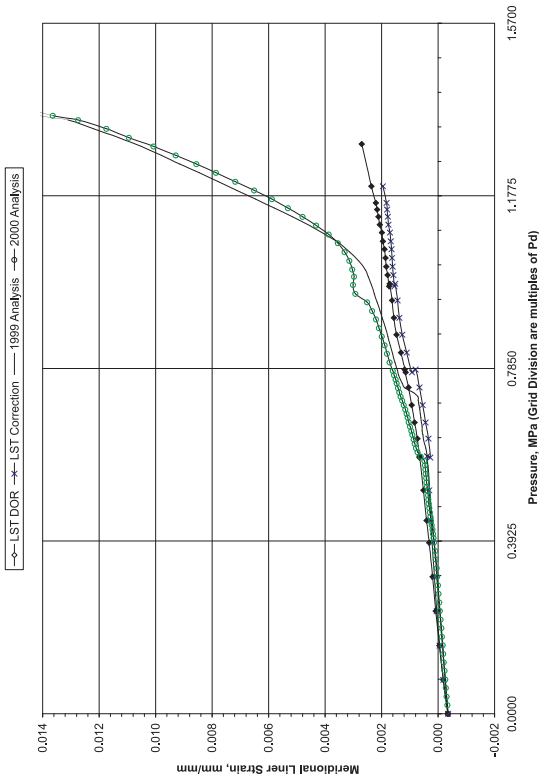
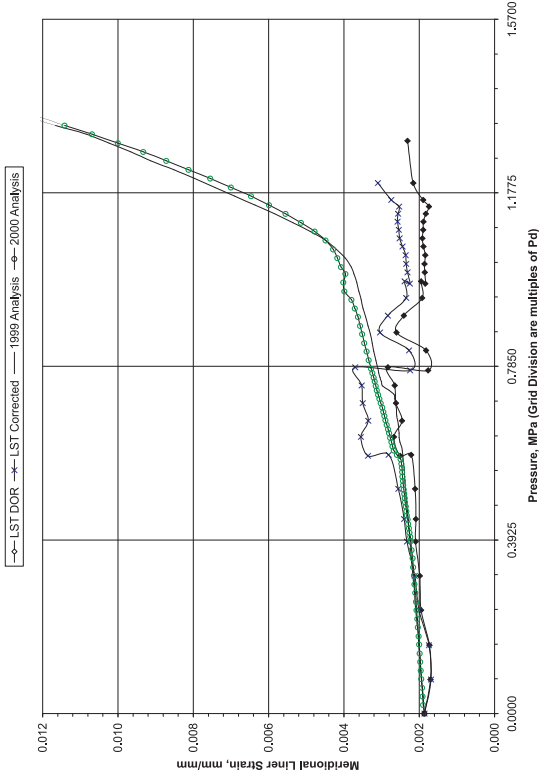


Figure 4-9. Comparisons at Standard Output Location 32 and 33

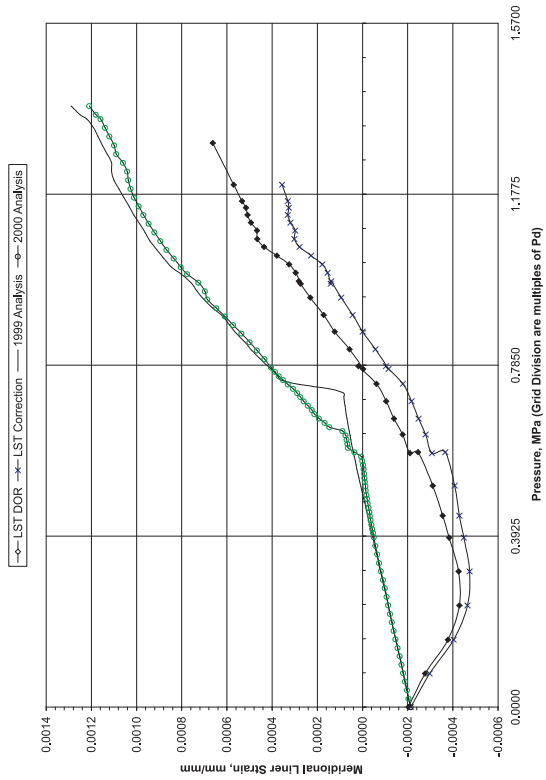
Standard Output Location #34. Azimuth: 0 Degrees, Elevation: 0.01 Meters, Inside Liner Surface, Base of Cylinder



Standard Output Location #35. Azimuth: 0 Degrees, Elevation: 0.01 Meters, Outside Liner Surface, Base of Cylinder



Standard Output Location #36. Azimuth: 135 Degrees, Elevation: 0.25 Meters, Inside Liner Surface, Base of Cylinder



Standard Output Location #37. Azimuth: 135 Degrees, Elevation: 0.25 Meters, Inside Liner Surface, Base of Cylinder

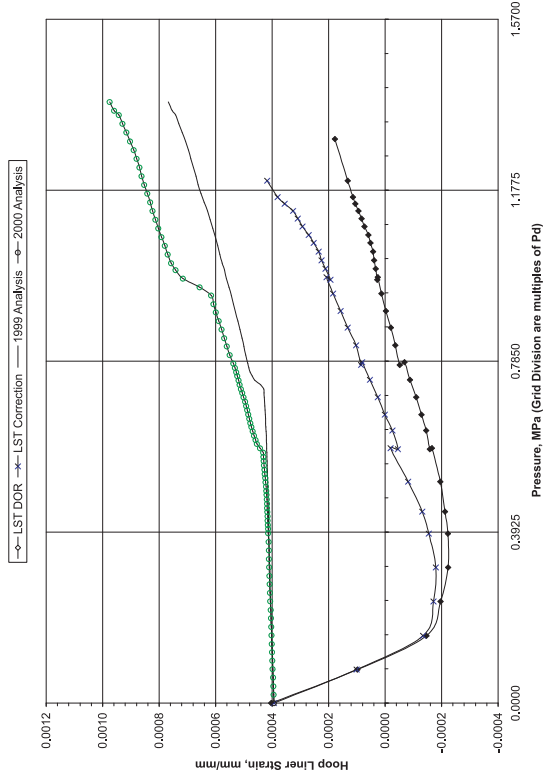
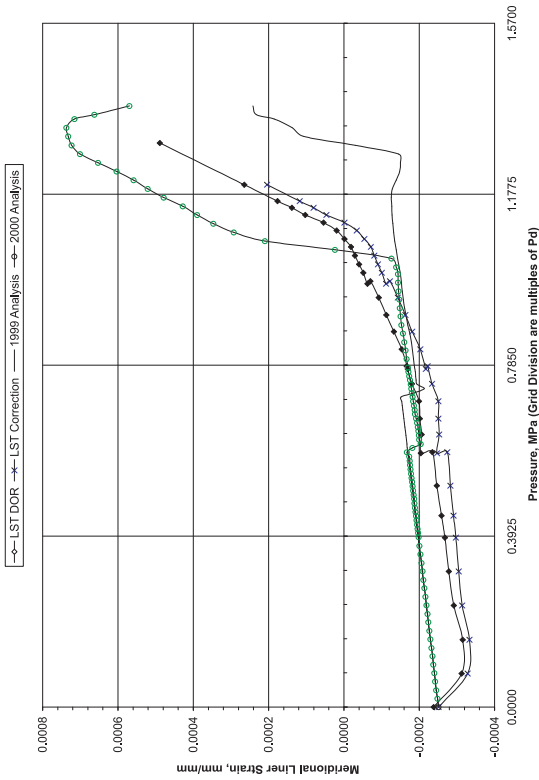
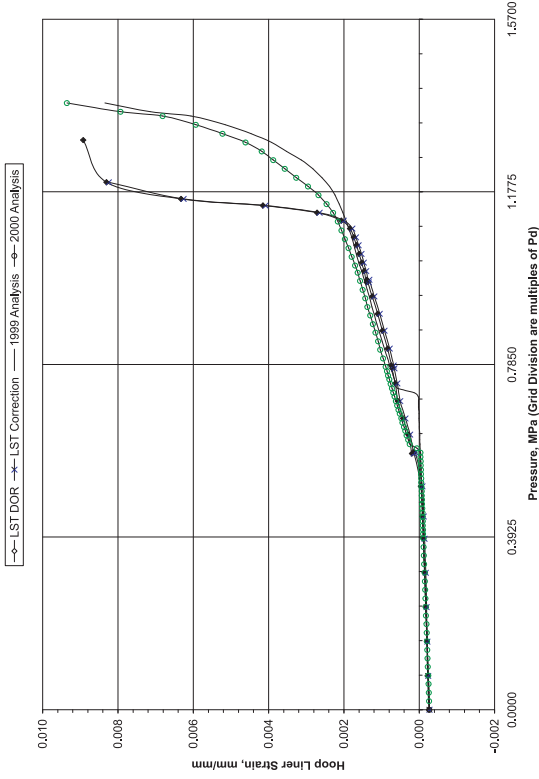


Figure 4-10. Comparisons at Standard Output Location 34, 35, 36, and 37

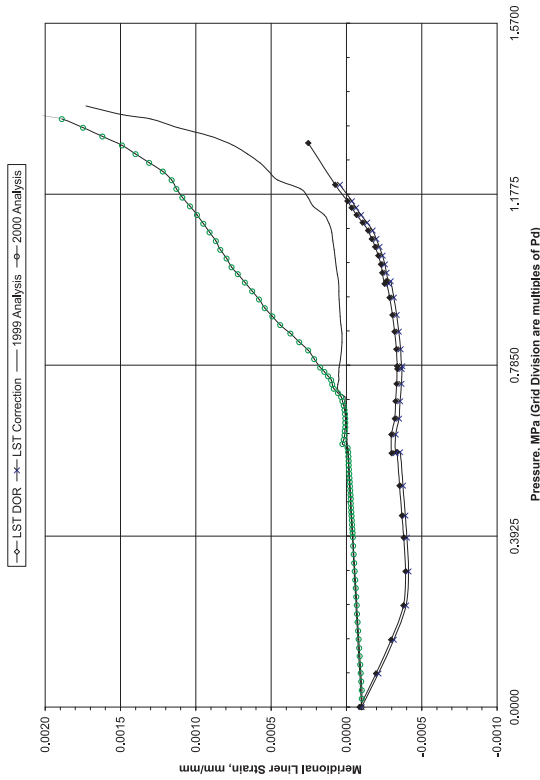
Standard Output Location #38. Azimuth: 135 Degrees, Elevation: 6.20 Meters, Inside Liner Surface, Midheight



Standard Output Location #39. Azimuth: 135 Degrees, Elevation: 6.20 Meters, Inside Liner Surface, Midheight



Standard Output Location #40. Azimuth: 135 Degrees, Elevation: 10.75 Meters, Inside Liner Surface, Springline



Standard Output Location #41. Azimuth: 135 Degrees, Elevation: 10.75 Meters, Inside Liner Surface, Springline

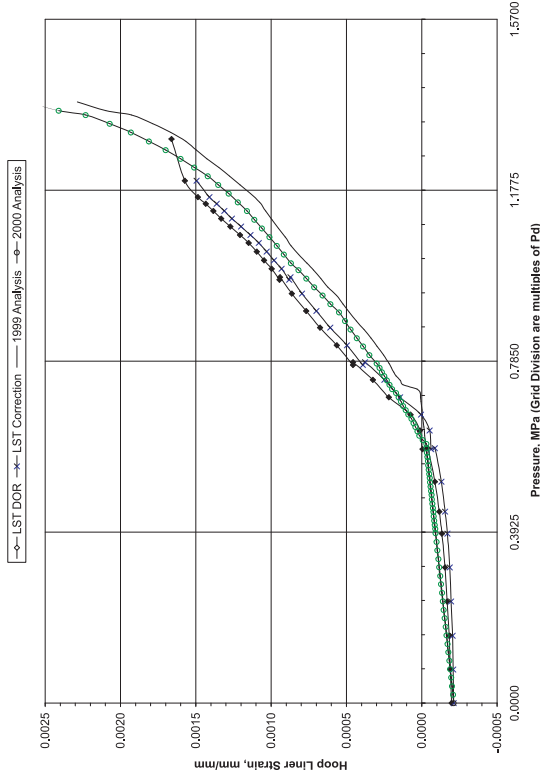
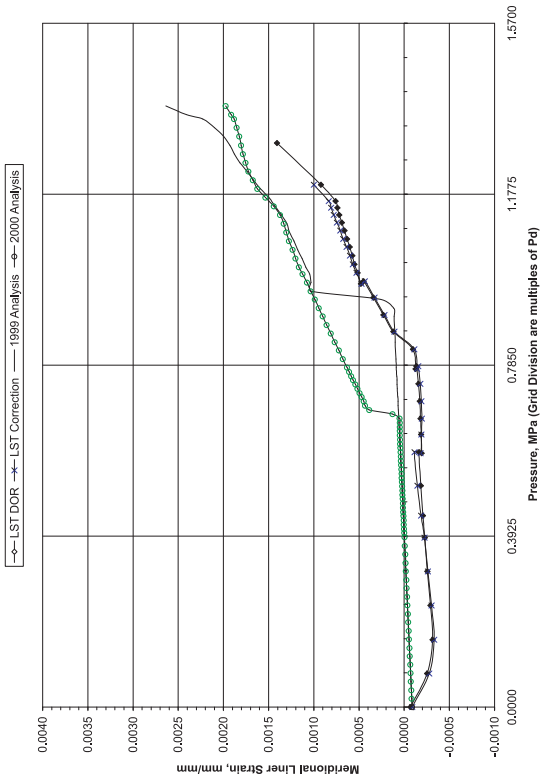
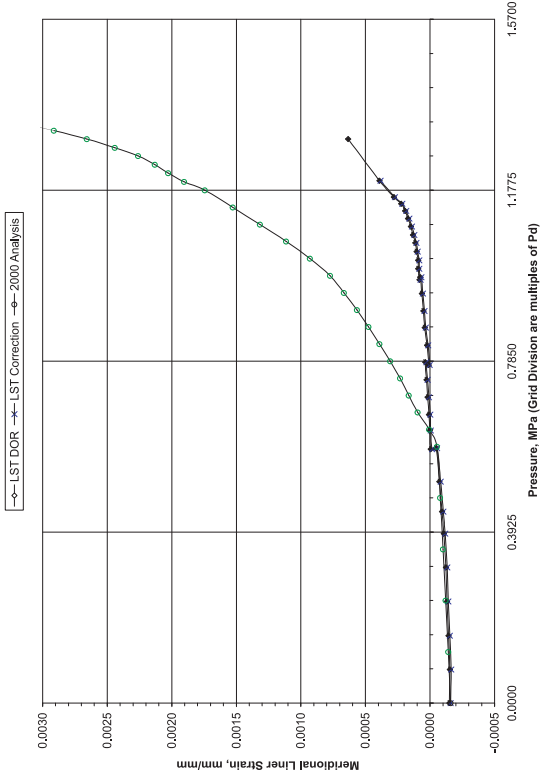


Figure 4-11. Comparisons at Standard Output Location 38, 39, 40, and 41

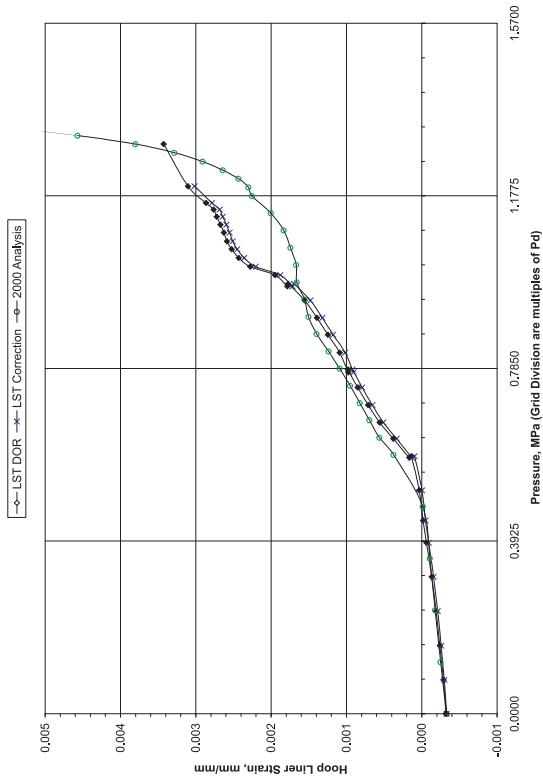
Standard Output Location #42. Azimuth: 135 Degrees, Elevation: 16.13 Meters, Inside Liner Surface, Dome Apex



Standard Output Location #43. Azimuth: 90 Degrees, Elevation: 6.20 Meters, Inside Liner Surface, Midheight at Buttress



Standard Output Location #44. Azimuth: 90 Degrees, Elevation: 6.20 Meters, Inside Liner Surface, Midheight at Buttress



Standard Output Location #45. Azimuth: 334 Degrees, Elevation: 4.675 Meters, Inside Liner Surface, 10 mm from Thickened Plate

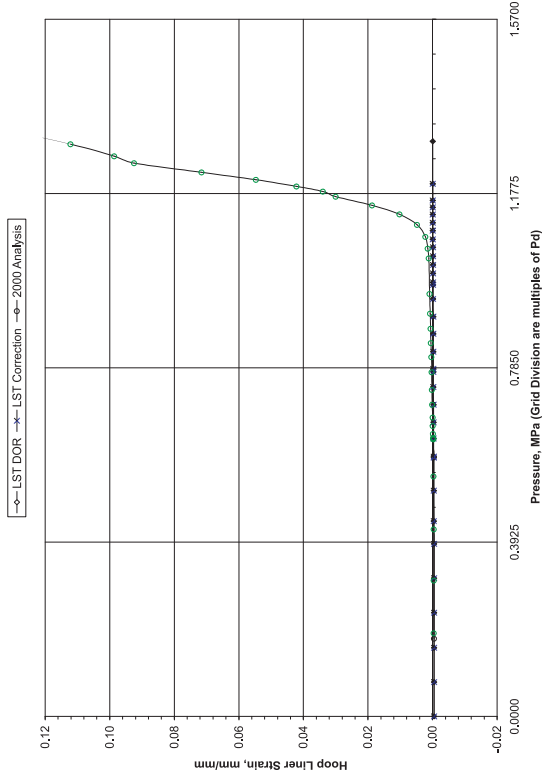
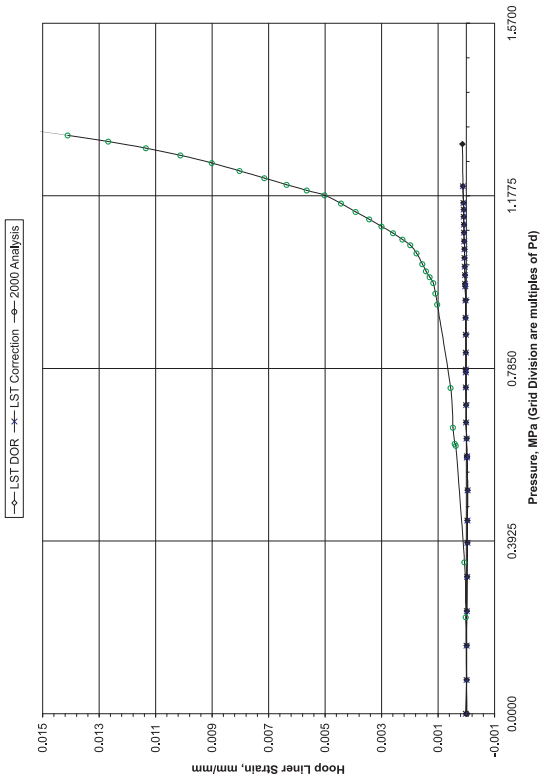


Figure 4-12. Comparisons at Standard Output Location 42, 43, 44, and 45

Standard Output Location #46. Azimuth: 88 Degrees, Elevation: 4.525 Meters,
 Inside Liner Surface, 10 mm from Thickened Plate



Standard Output Location #47. Azimuth: 135 Degrees, Elevation: 0.00 Meters,
 100 mm Inside Cylinder, FF Basement Liner Strain

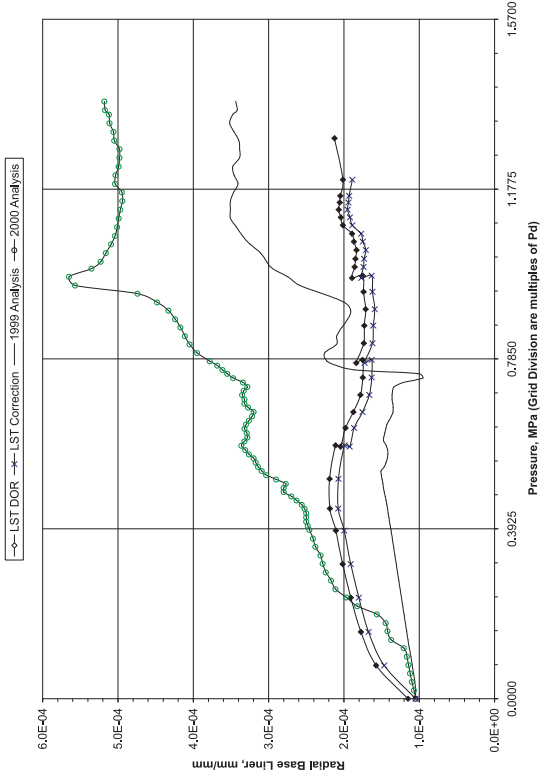
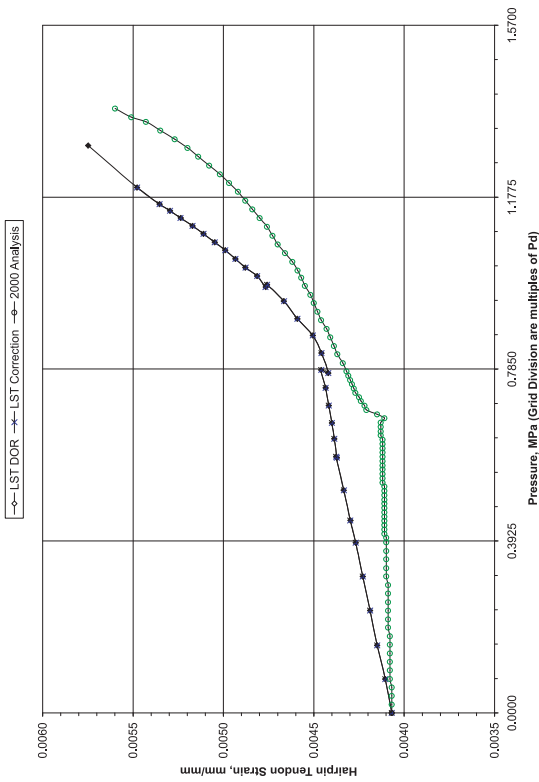
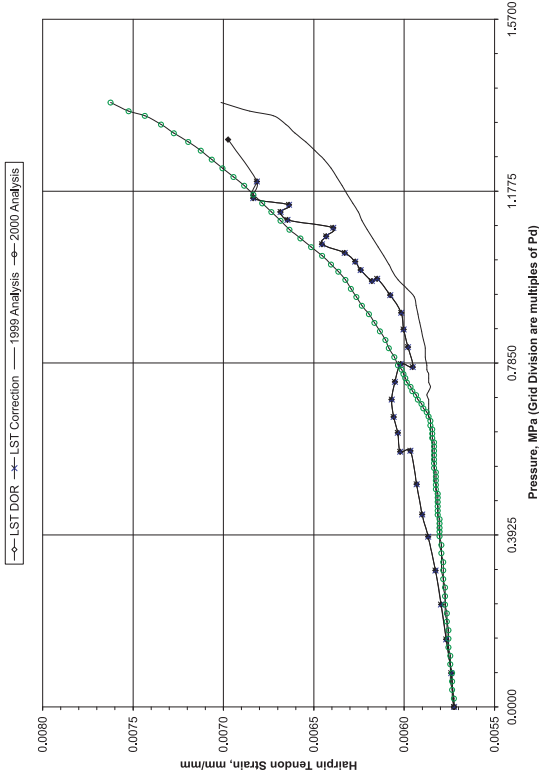


Figure 4-13. Comparisons at Standard Output Location 46 and 47

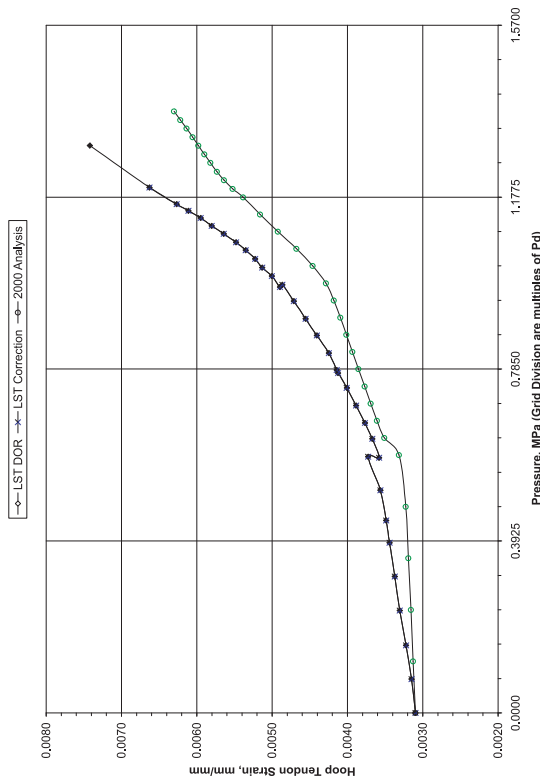
Standard Output Location #48, Azimuth: 180 Degrees, Elevation: 15.60 Meters, Tendon - V37, Tendon Apex



Standard Output Location #49, Azimuth: 135 Degrees, Elevation: 10.75 Meters, Tendon - V46, Tendon Springline



Standard Output Location #50, Azimuth: 90 Degrees, Elevation: 6.58 Meters, Tendon - H53, Mid Tendon



Standard Output Location #52, Azimuth: 280 Degrees, Elevation: 6.58 Meters, Tendon - H53, Tendon Near Buttress

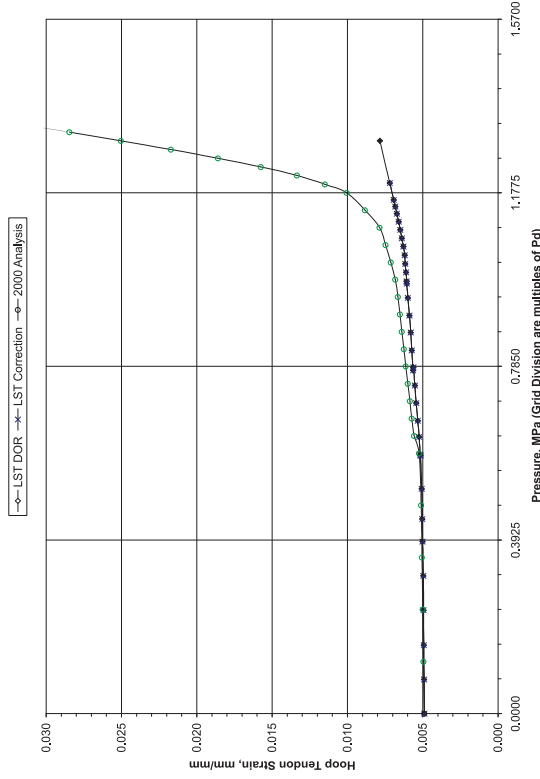
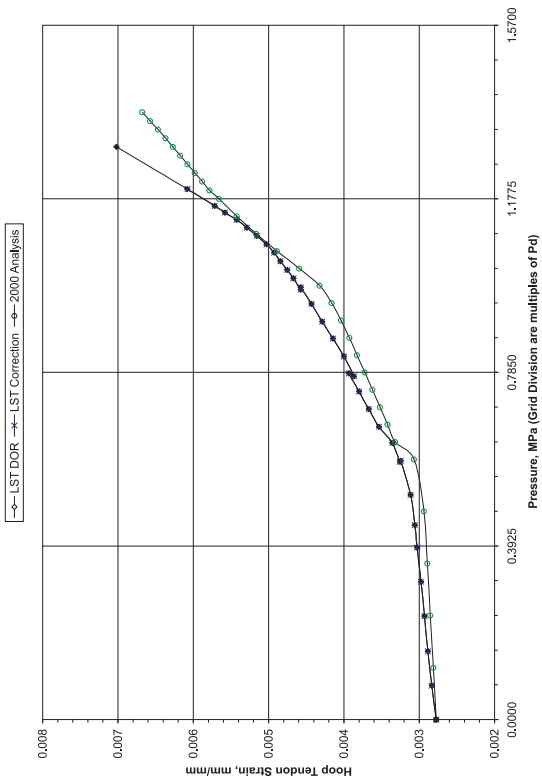
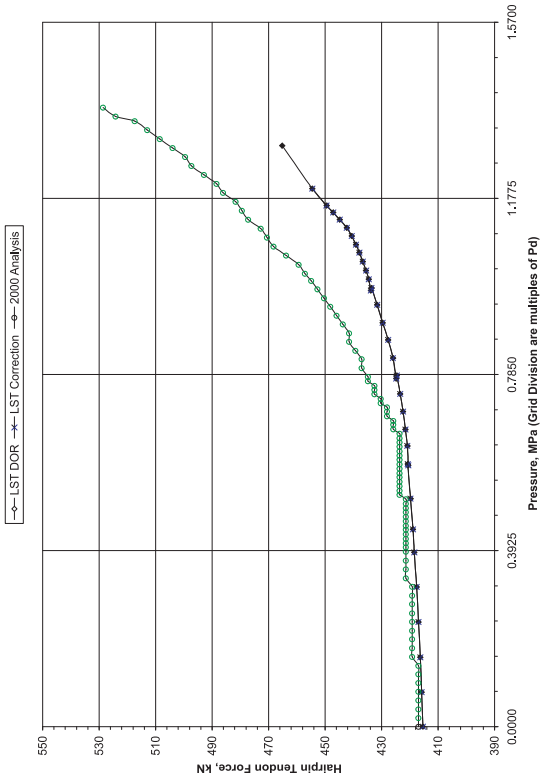


Figure 4-14. Comparisons at Standard Output Location 48, 49, 50, and 52

Standard Output Location #53, Azimuth: 0 Degrees, Elevation: 4.57 Meters, Tendon - HS3, Tendon between EIJ and AL



Standard Output Location #54, Azimuth: 241 Degrees, Elevation: -1.16 Meters, Tendon - V37, Tendon Gallery



Standard Output Location #55, Azimuth: 275 Degrees, Elevation: 6.58 Meters, Tendon - HS3, Tendon at Buttress

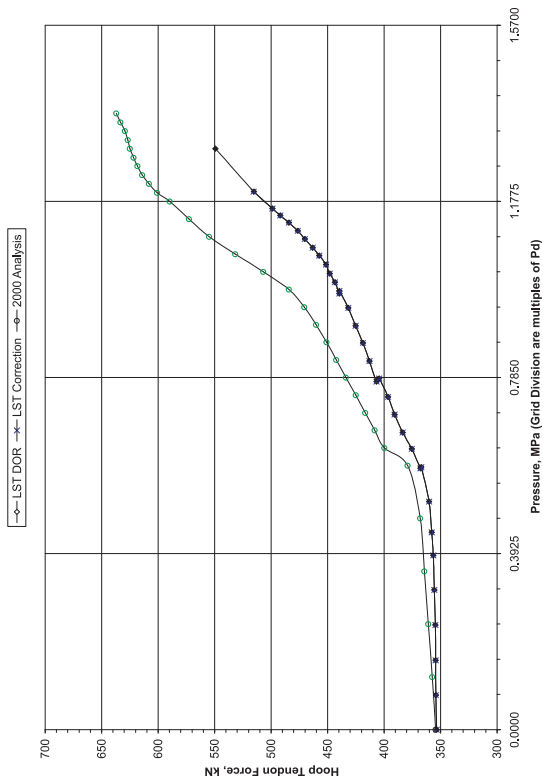


Figure 4-15. Comparisons at Standard Output Location 53, 54, and 55

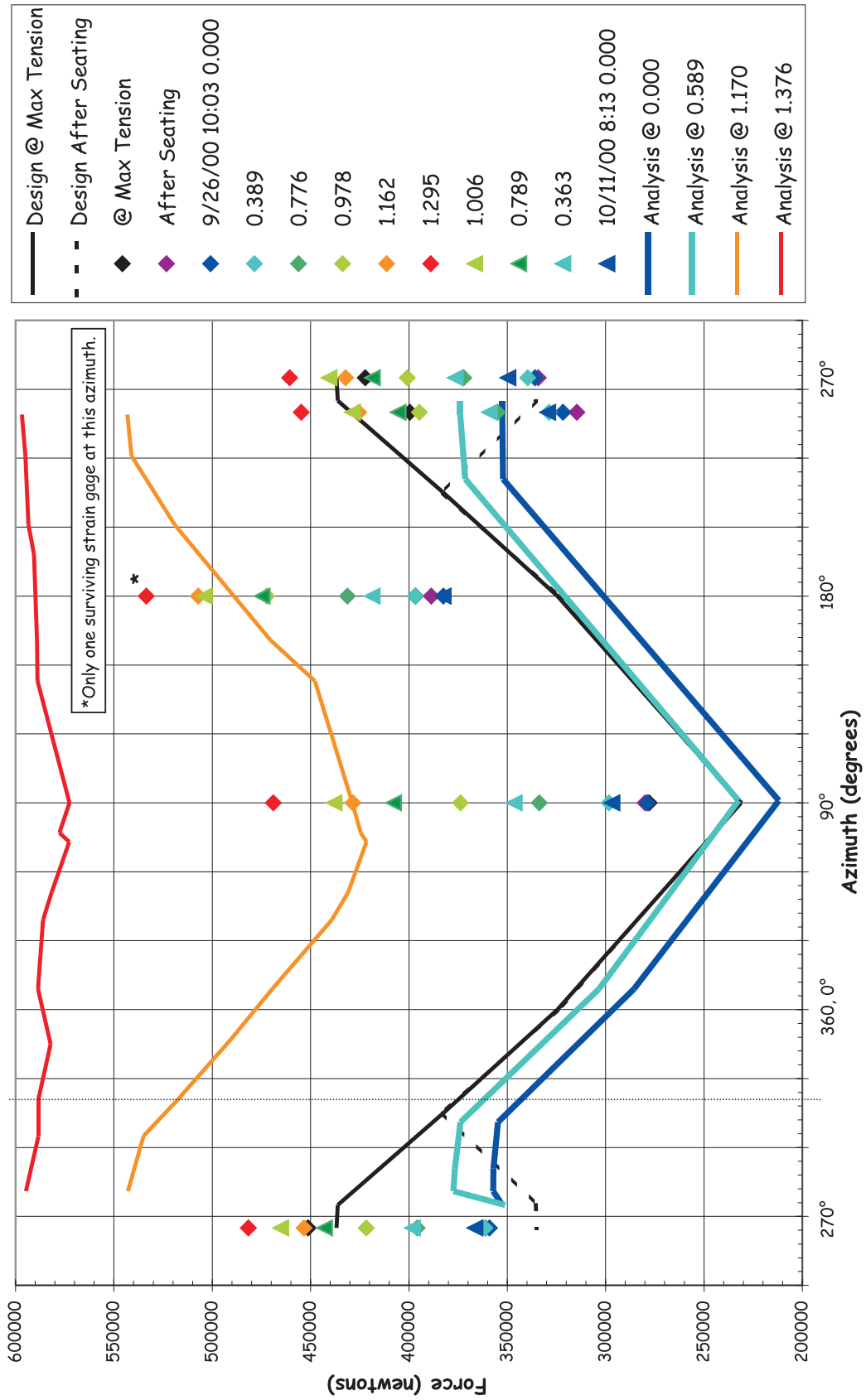


Figure 4-16. H11 Tendon Force Distribution, El. 1854 (Load Cells and Average of Wire Strain Gages)

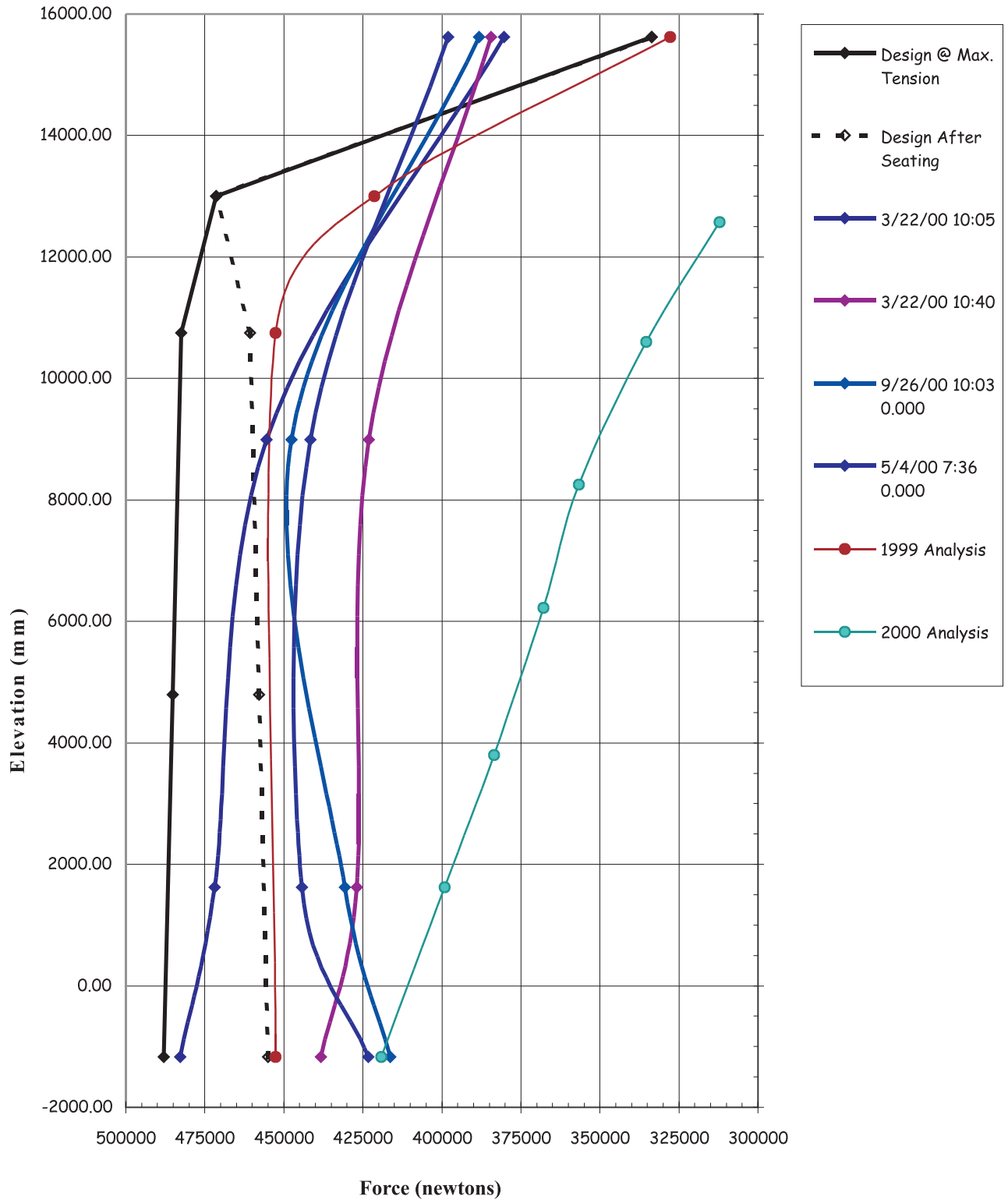


Figure 4-17. V37 Tendon Force Distribution @ Azimuth 240 (Load Cells and Average of Wire Strain Gages)

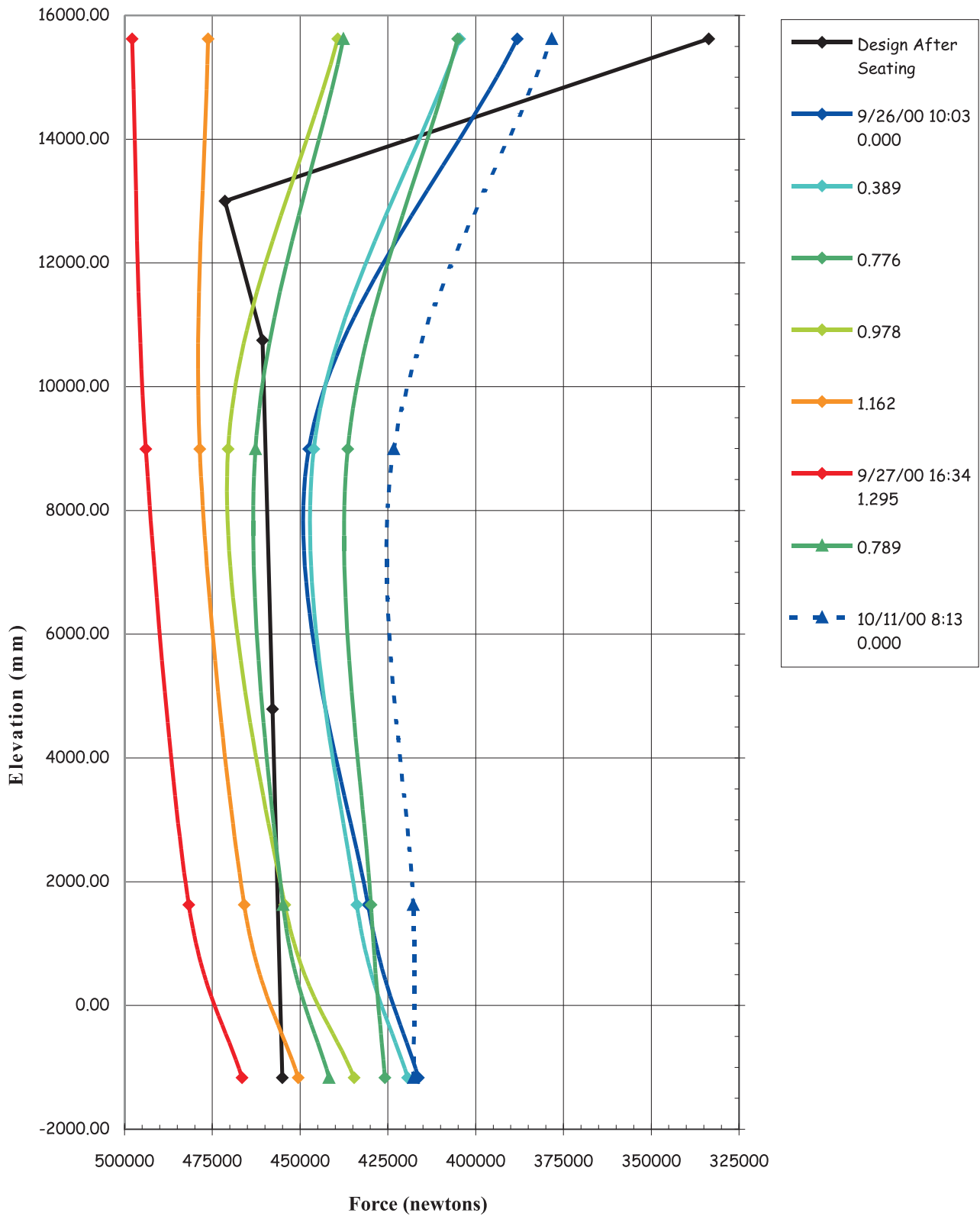


Figure 4-18. V37 Tendon Force Distribution @ Azimuth 240
(Load Cells and Average of Wire Strain Gages)

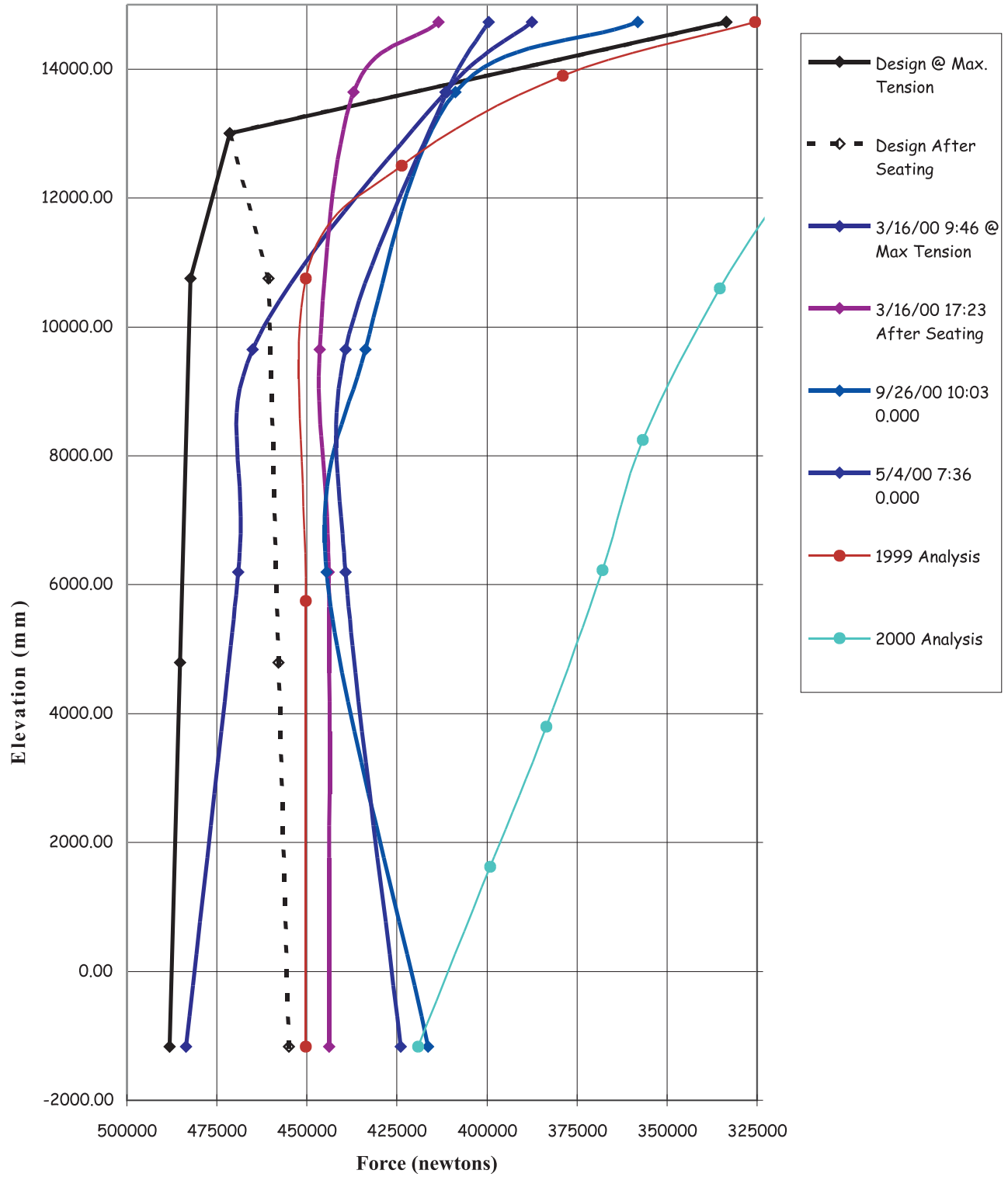


Figure 4-19. V46 Tendon Force Distribution @ Azimuth 135
(Load Cells and Average of Wire Strain Gages)

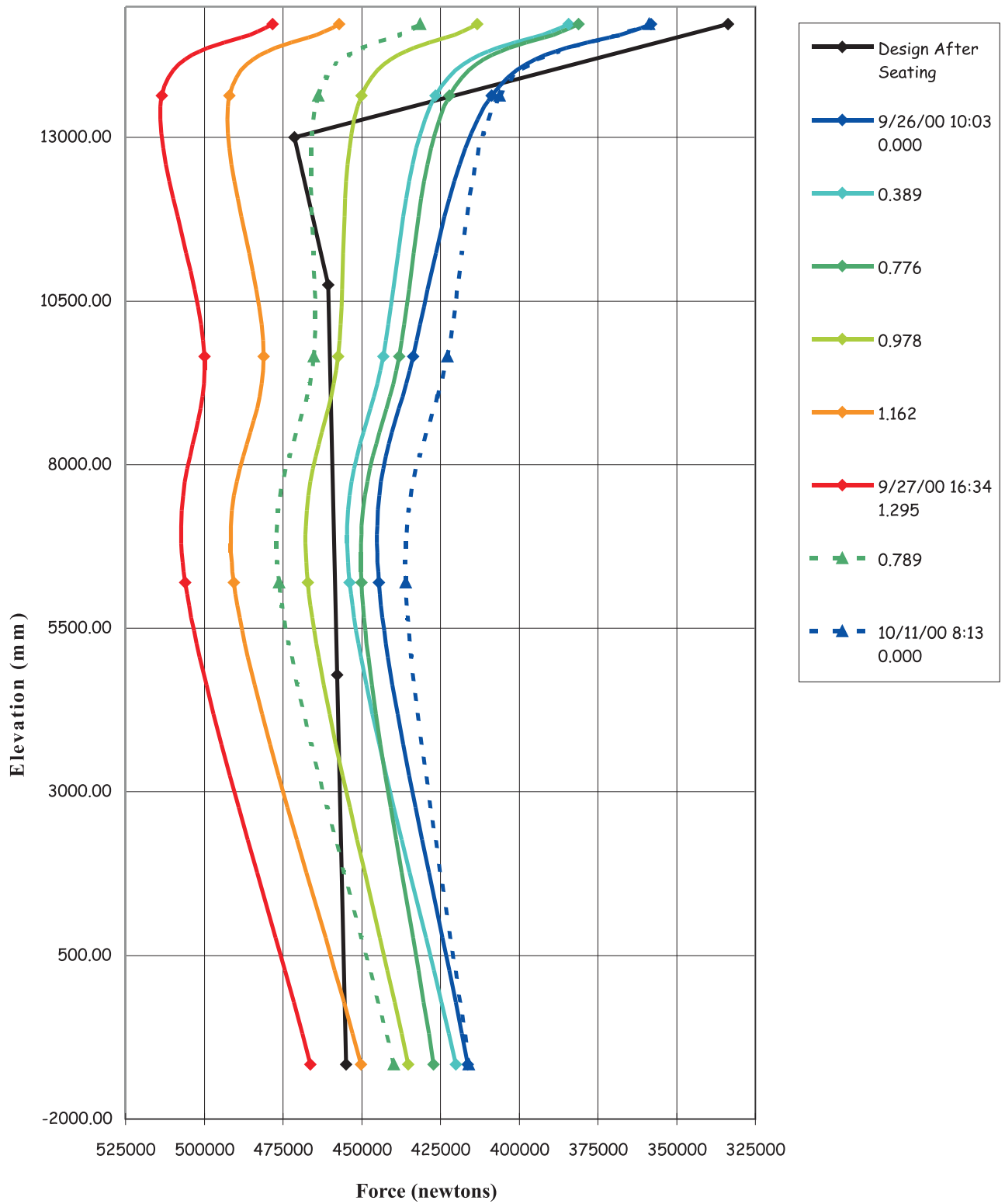


Figure 4-20. V46 Tendon Force Distribution @ Azimuth 135 (Load Cells and Average of Wire Strain Gages)

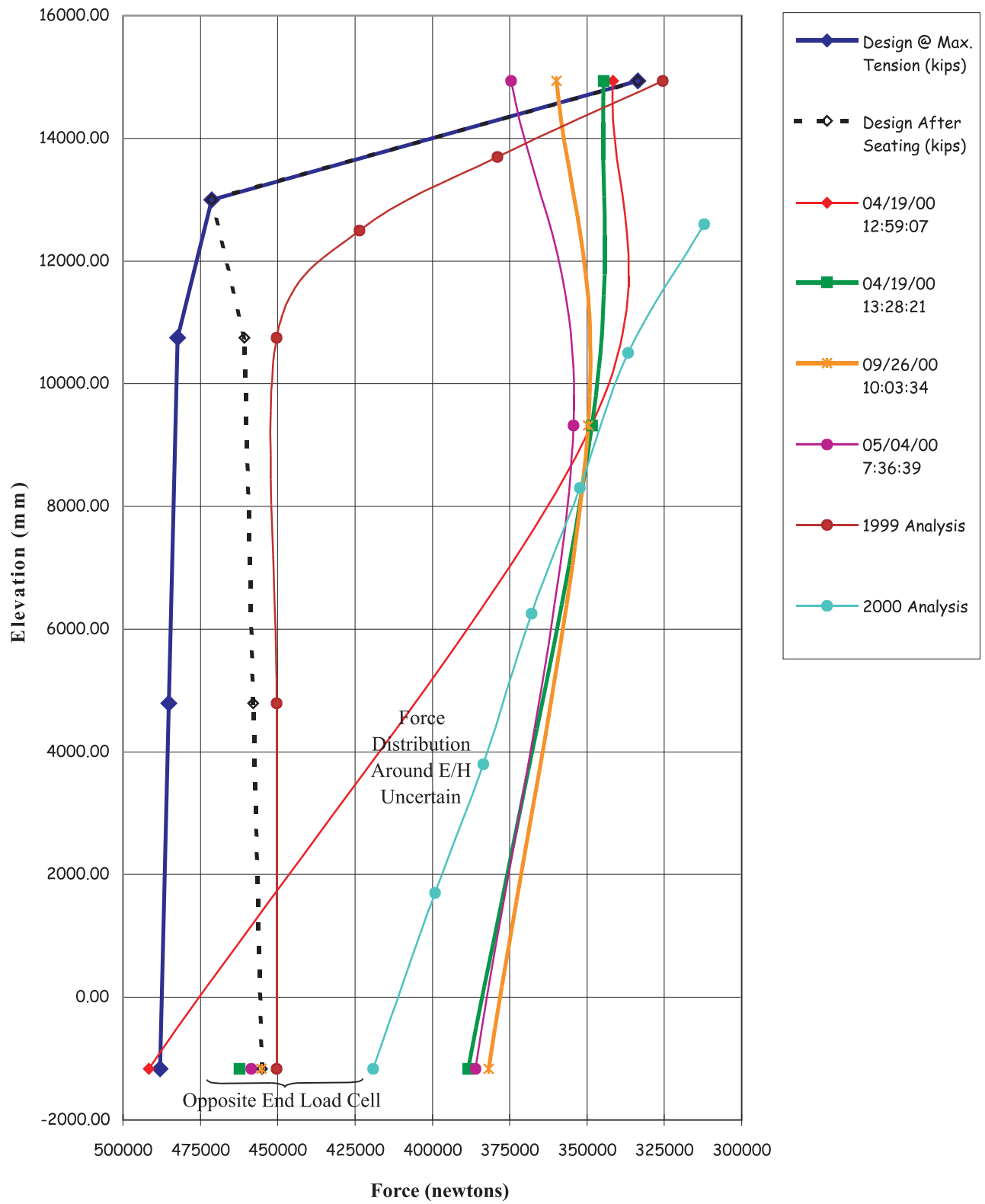


Figure 4-21. V85 Tendon Force Distribution @ Azimuth 325 (Load Cells and Average of Wire Strain Gages)

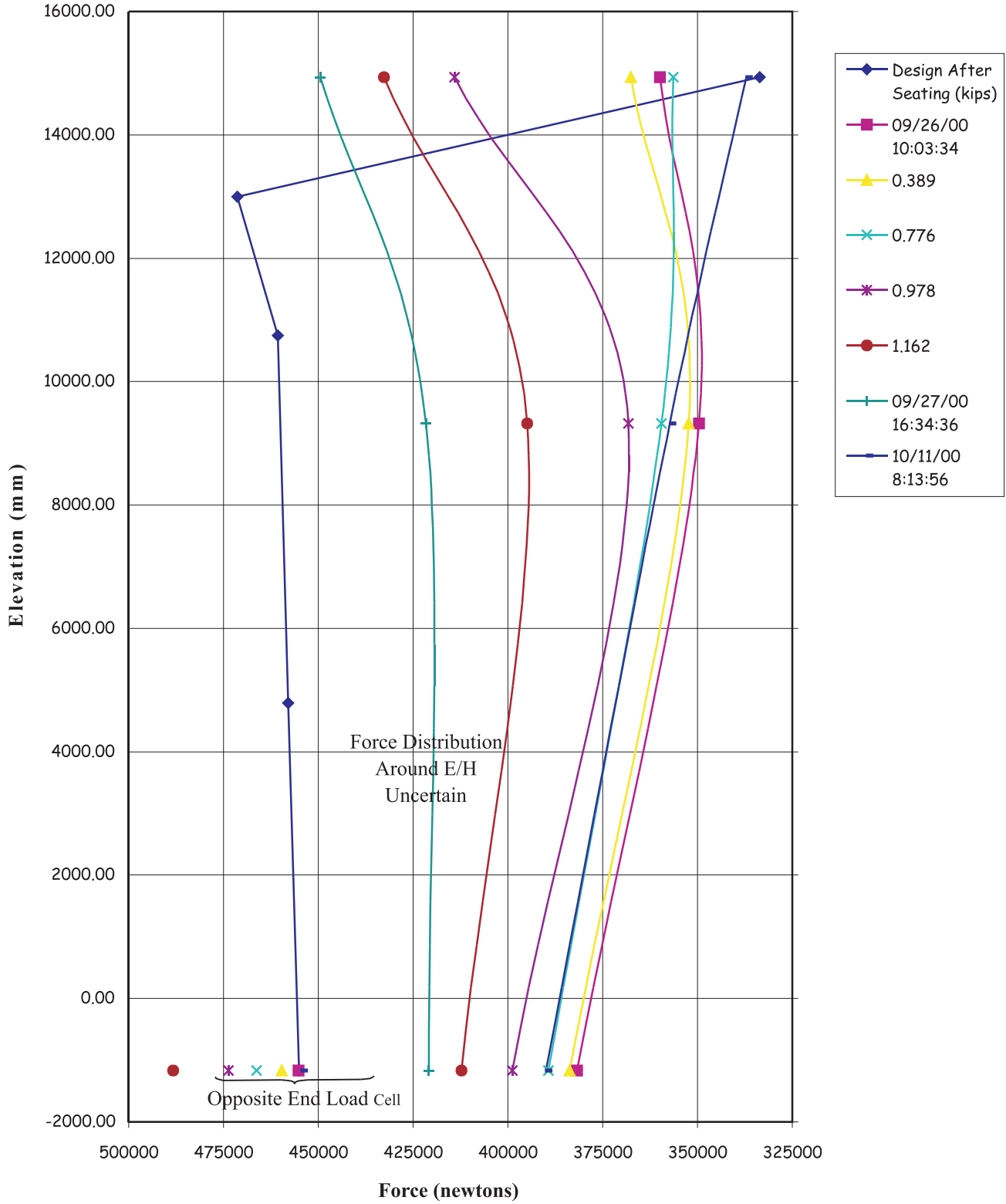


Figure 4-22. V85 Tendon Force Distribution @ Azimuth 325 (Load Cells and Average of Wire Strain Gages)

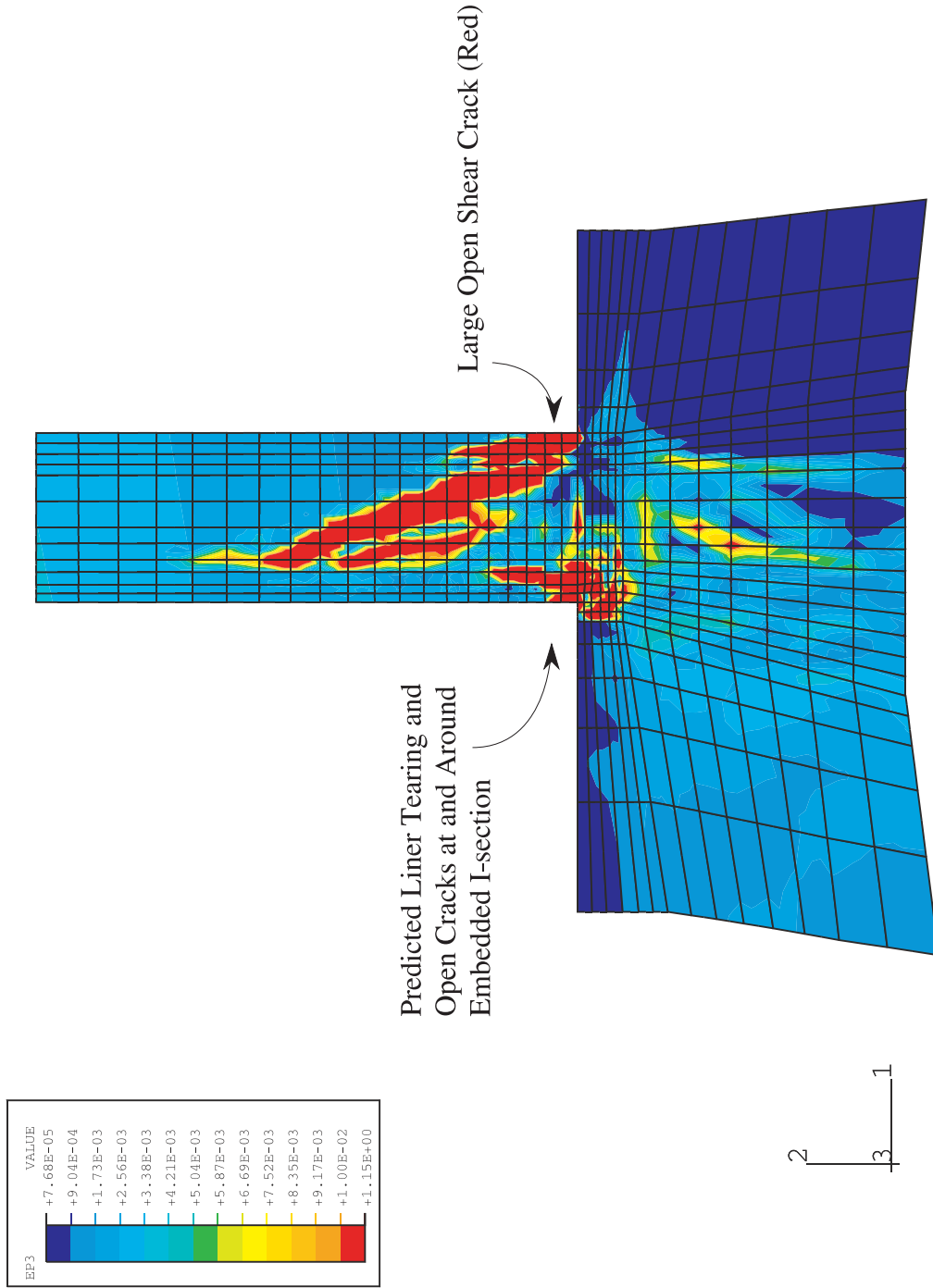


Figure 4-23. Maximum Principle Strain Contours in Wall-Base Region at $4.0 \times Pd$ Showing Open Cracks and Predicted Liner Tearing from 1999 Pretest Analysis

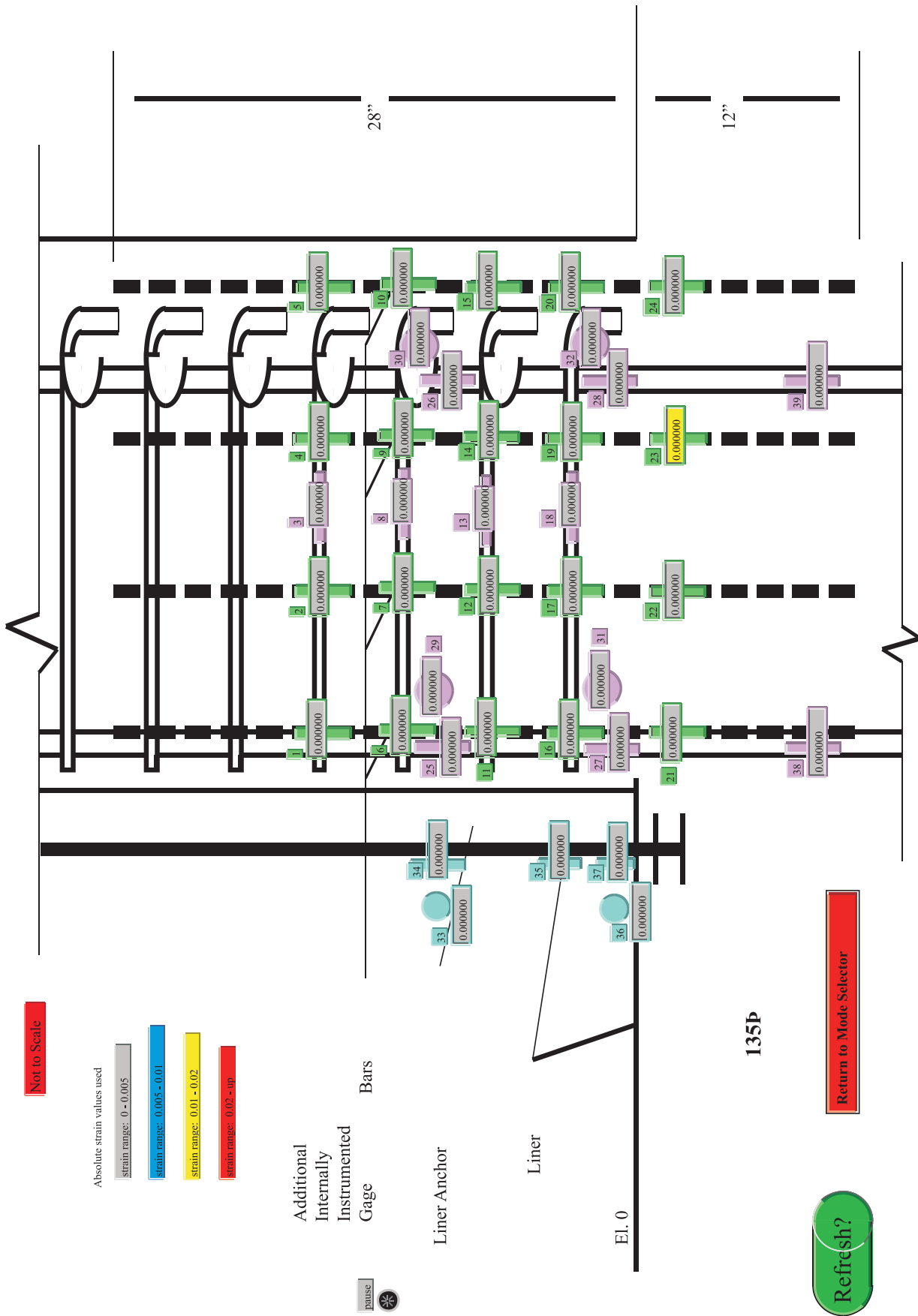


Figure 4-25. Basemat Junction, Gage Bar and Stirrup Strain Gage Locations

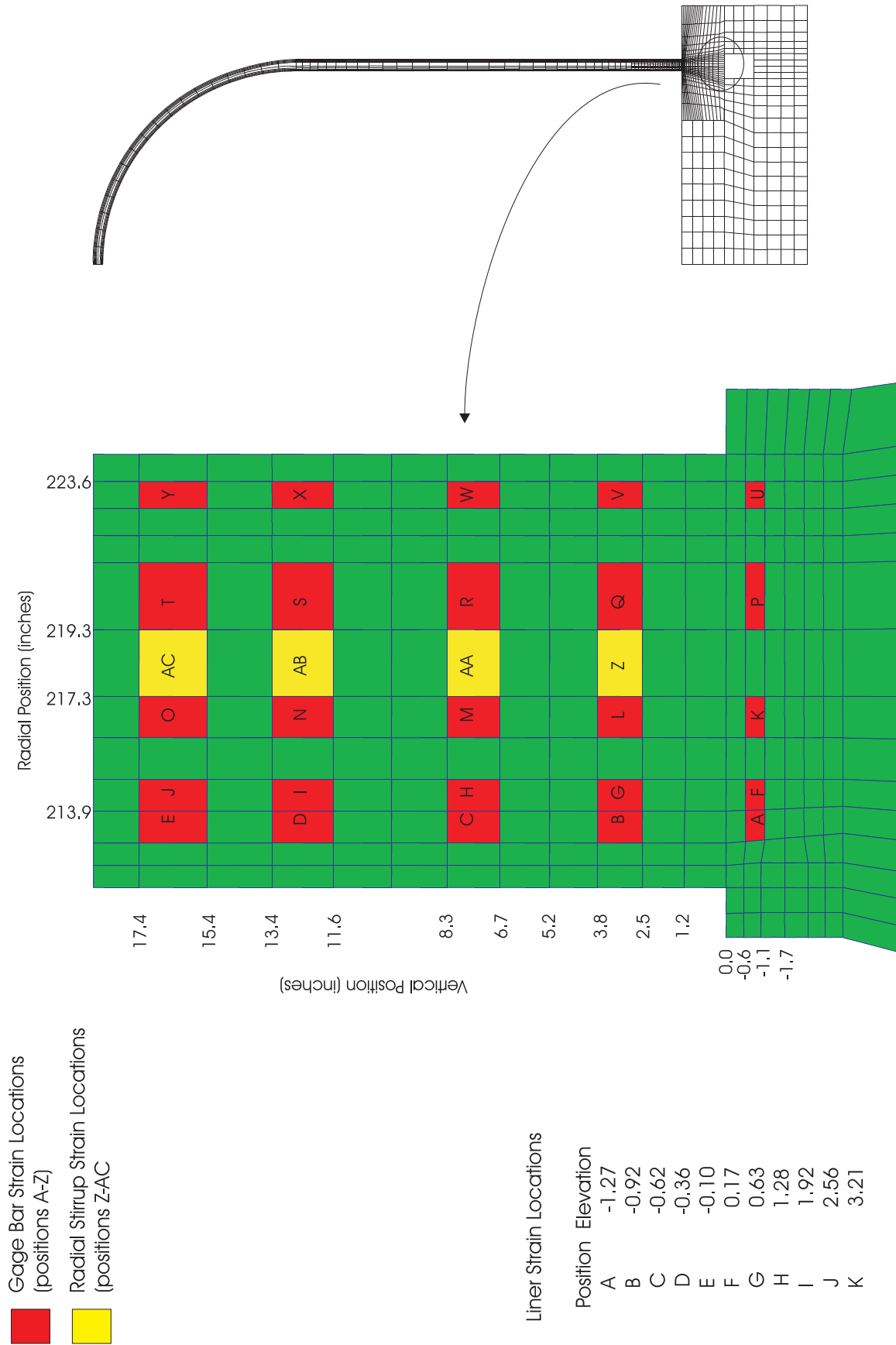


Figure 4-26. Axisymmetric Model Gage Bar, Stirrup, and Liner Strain Comparison Locations

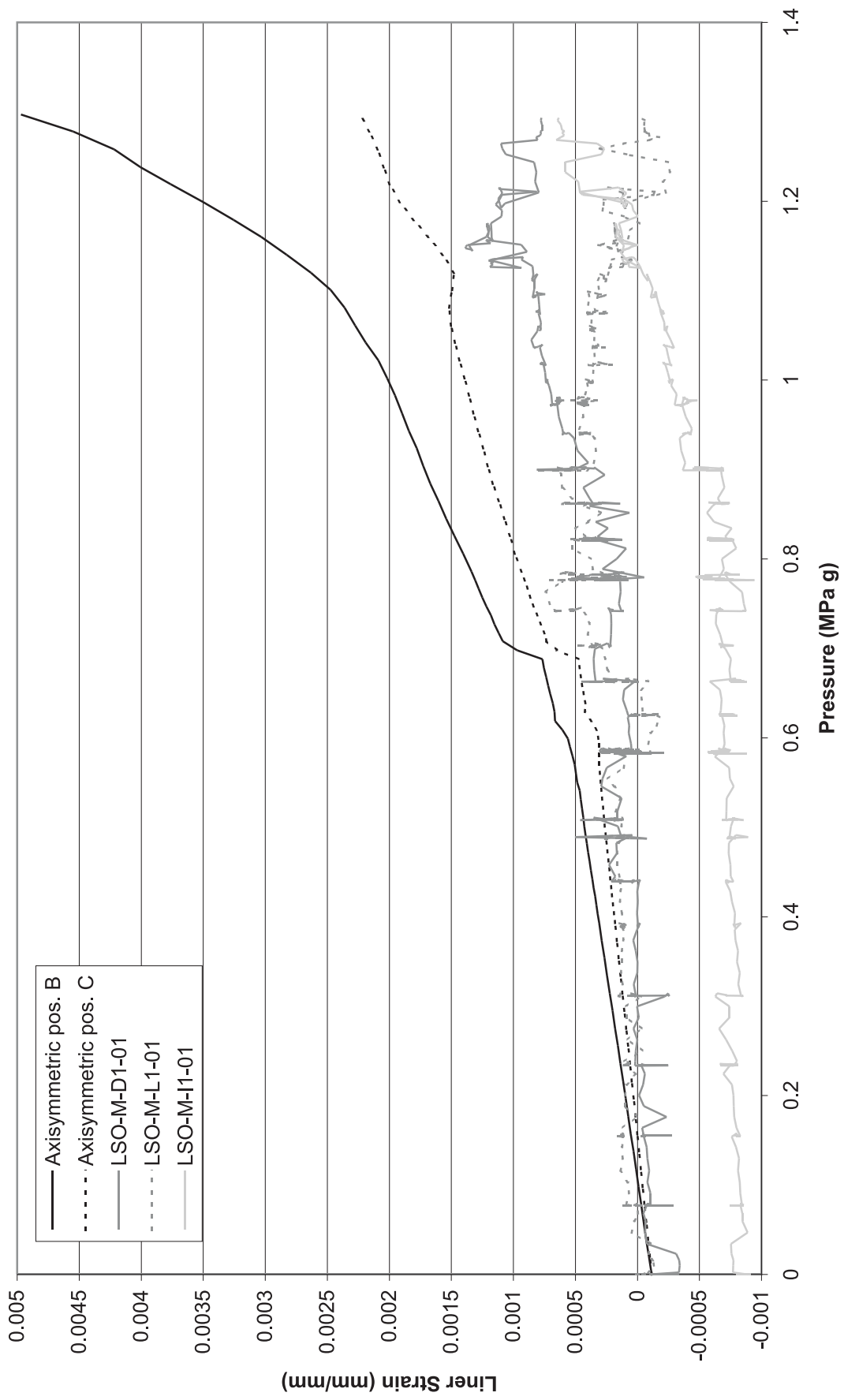


Figure 4-27. 1999 Pretest Analysis vs. LST at Wall Base Liner Position B-C

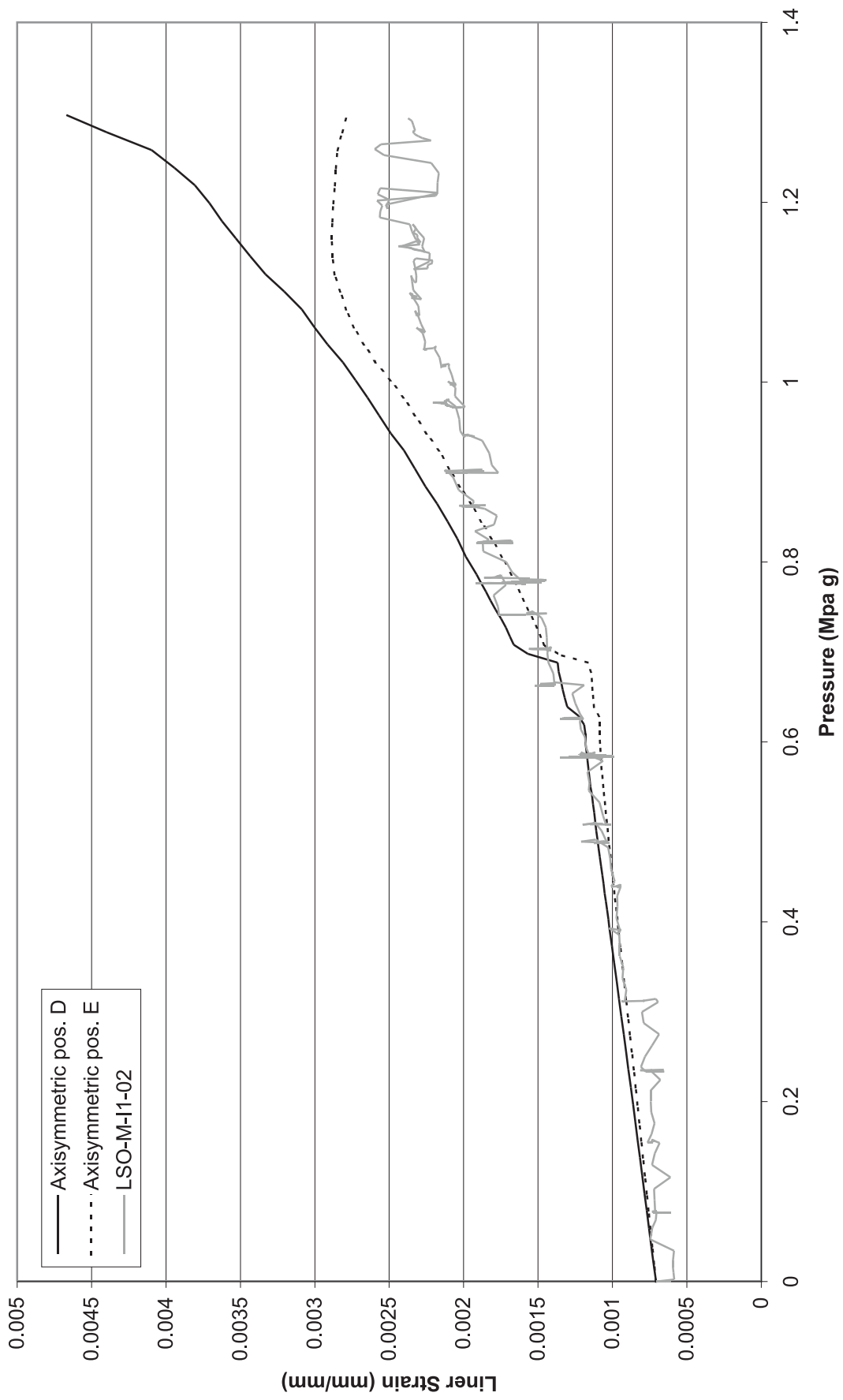


Figure 4-28. 1999 Pretest Analysis vs. LST at Wall Base Liner Position D-E

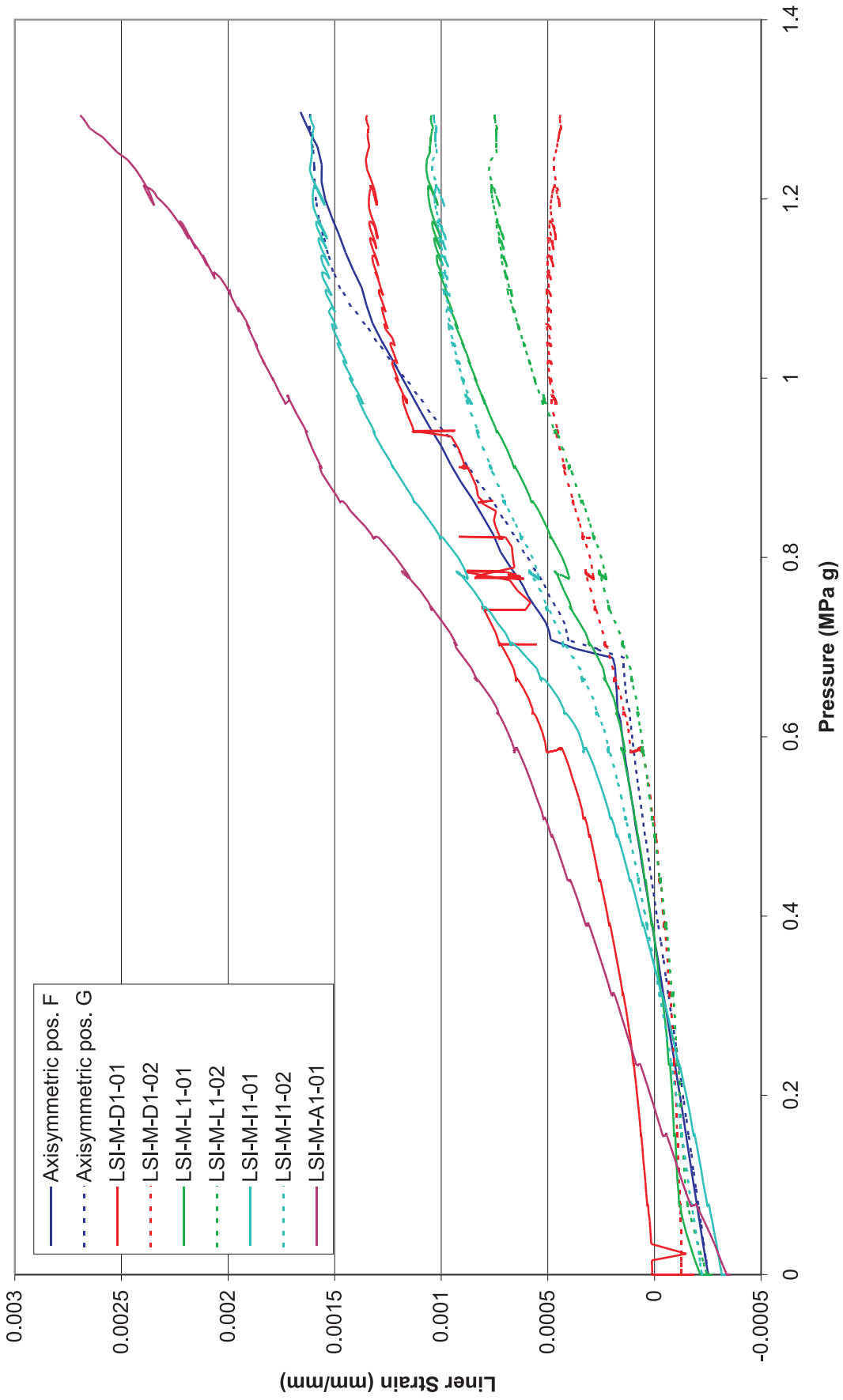


Figure 4-29. 1999 Pretest Analysis vs. LST at Wall Base Liner Position F-G

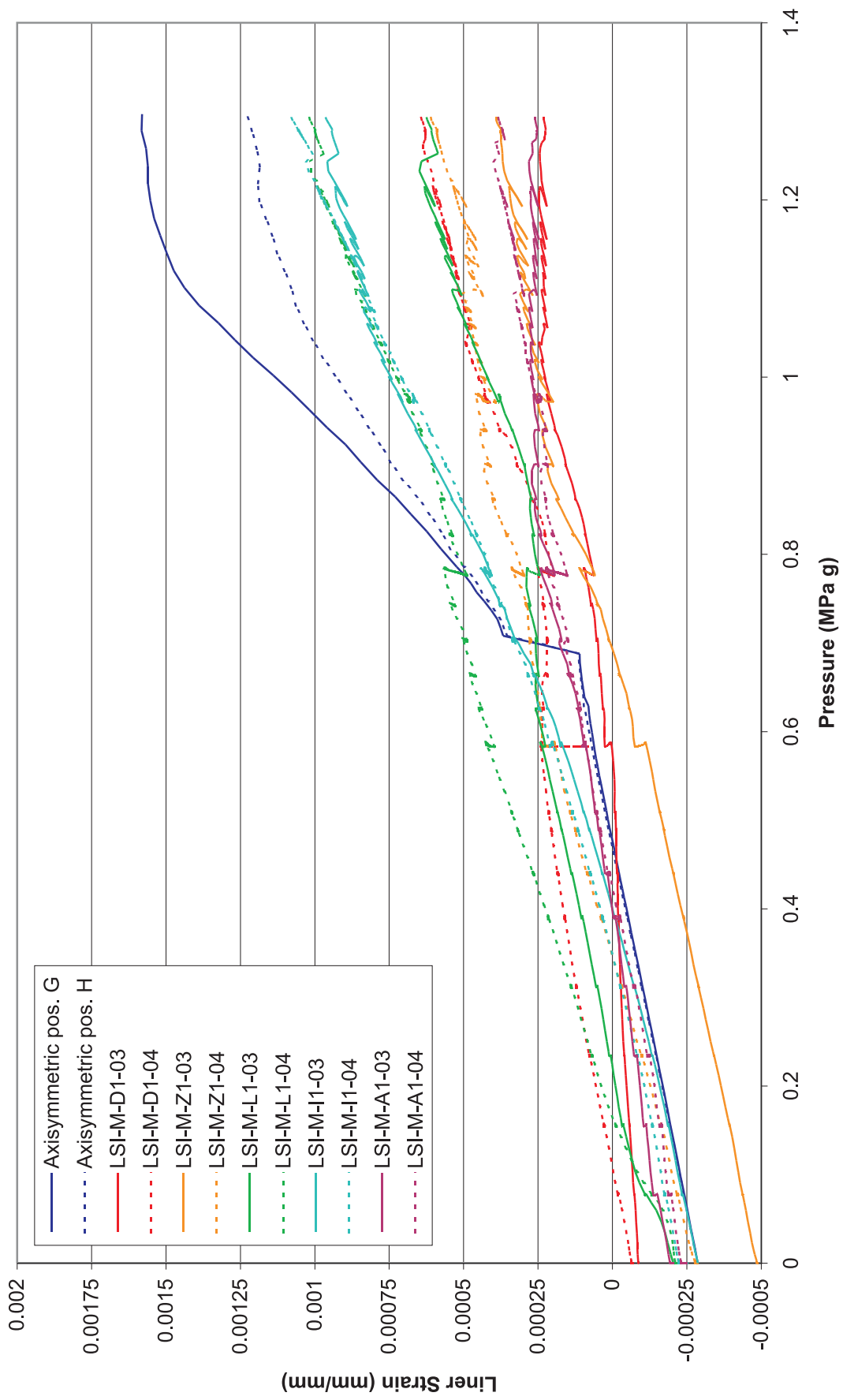


Figure 4-30. 1999 Pretest Analysis vs. LST at Wall Base Liner Position G-H

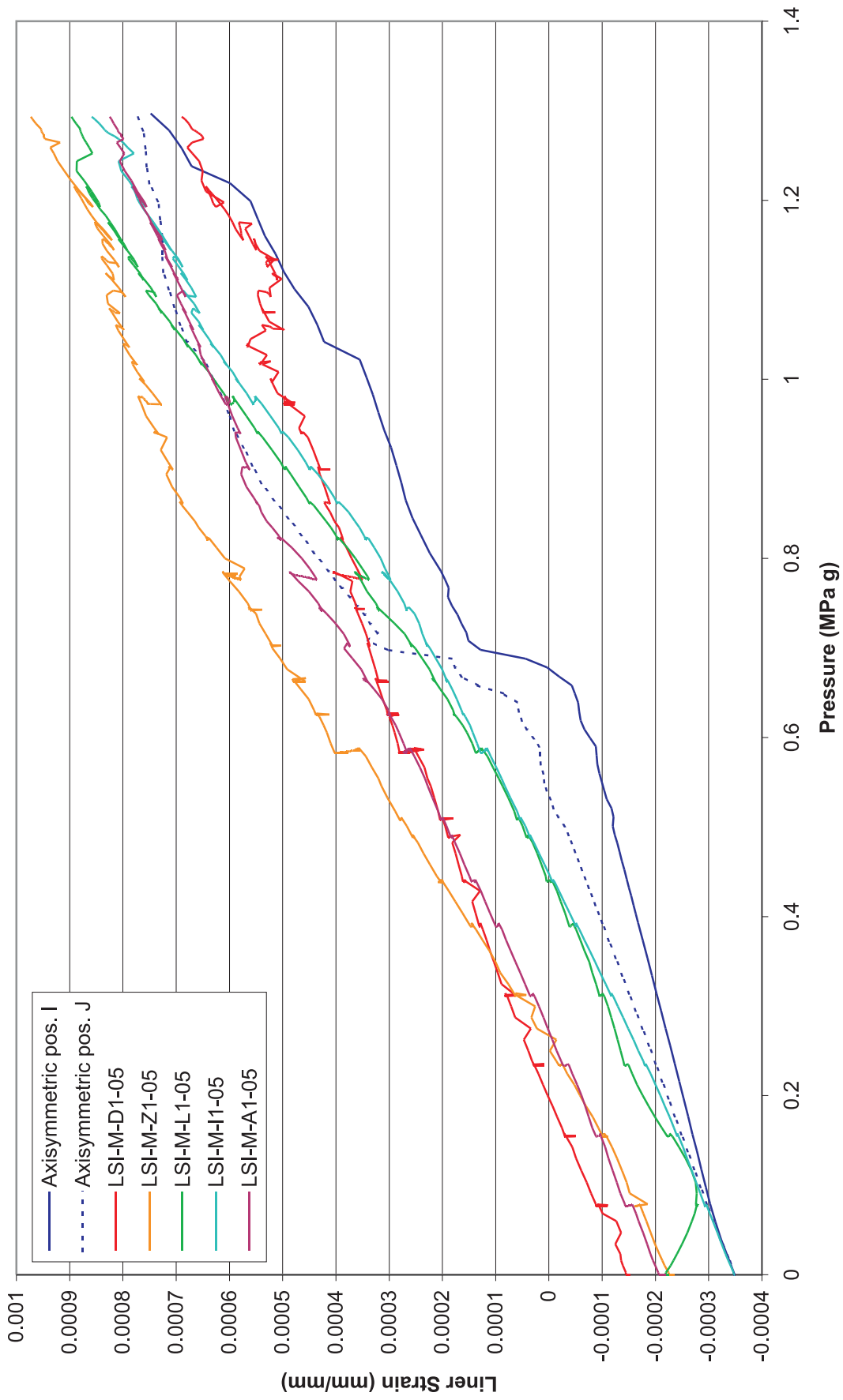


Figure 4-31. 1999 Pretest Analysis vs. LST at Wall Base Liner Position I-J

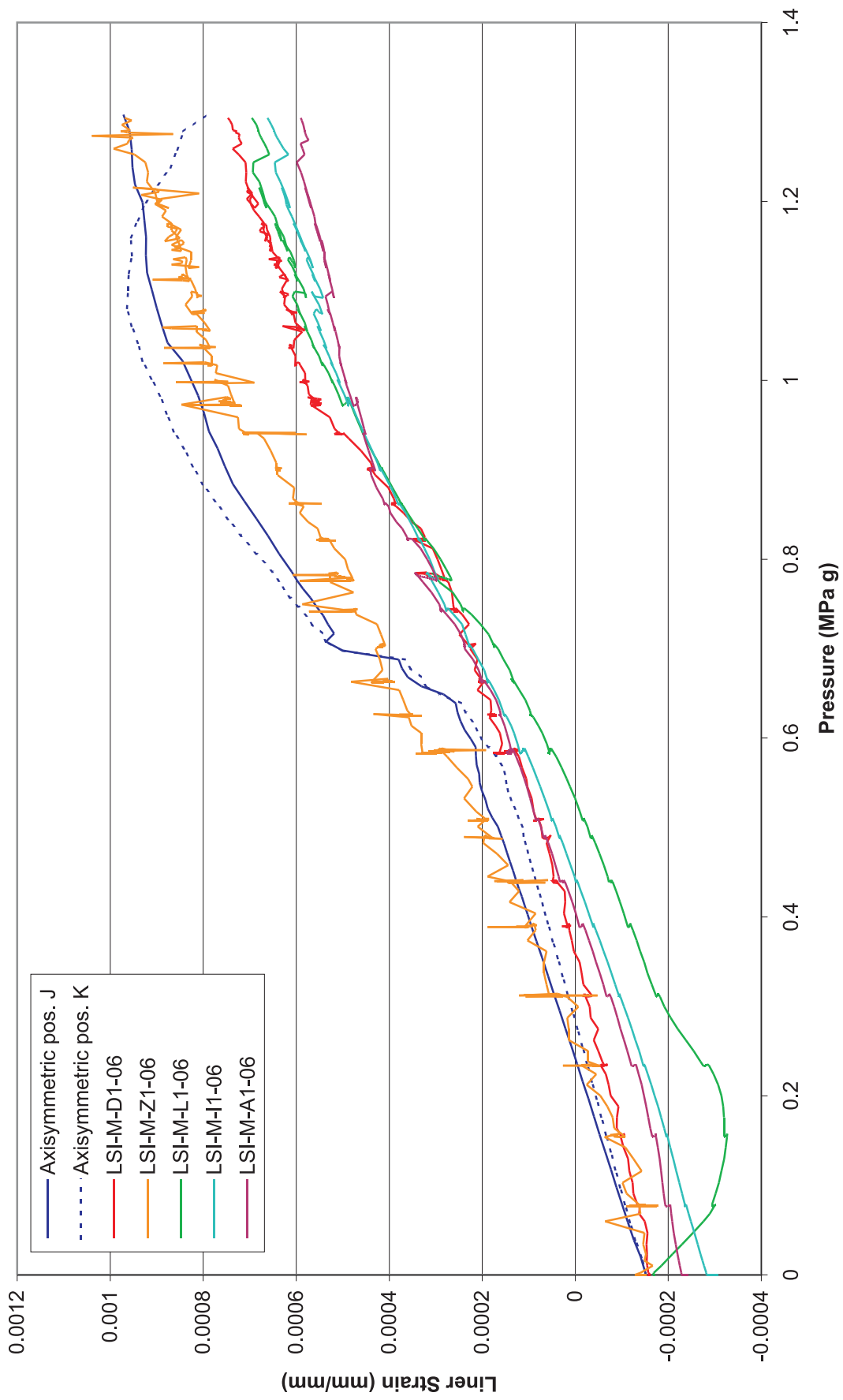


Figure 4-32. 1999 Pretest Analysis vs. LST at Wall Base Liner Position J-K

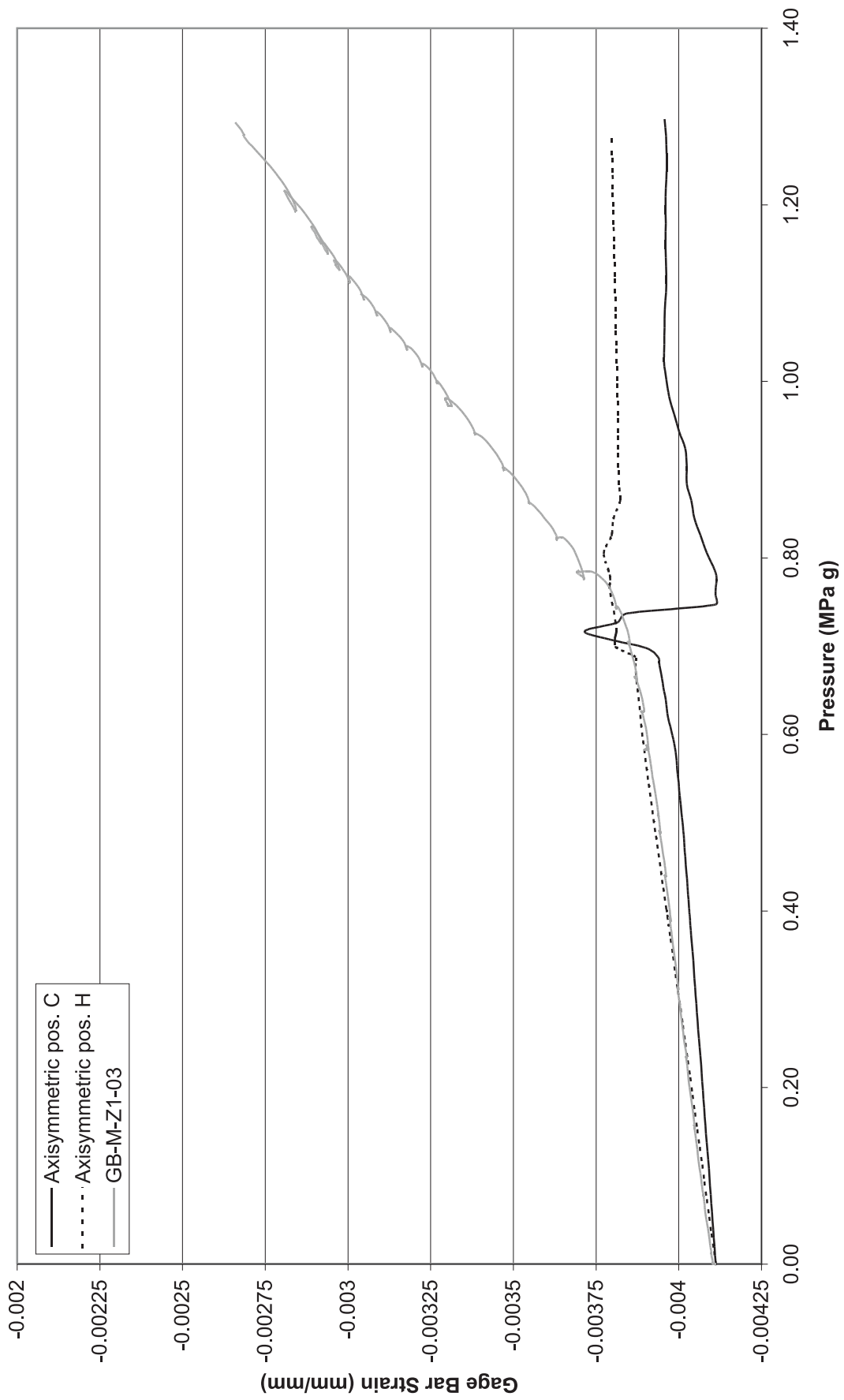


Figure 4-33. 1999 Pretest Analysis vs. LST at Wall Base Gage Bar Position C-H

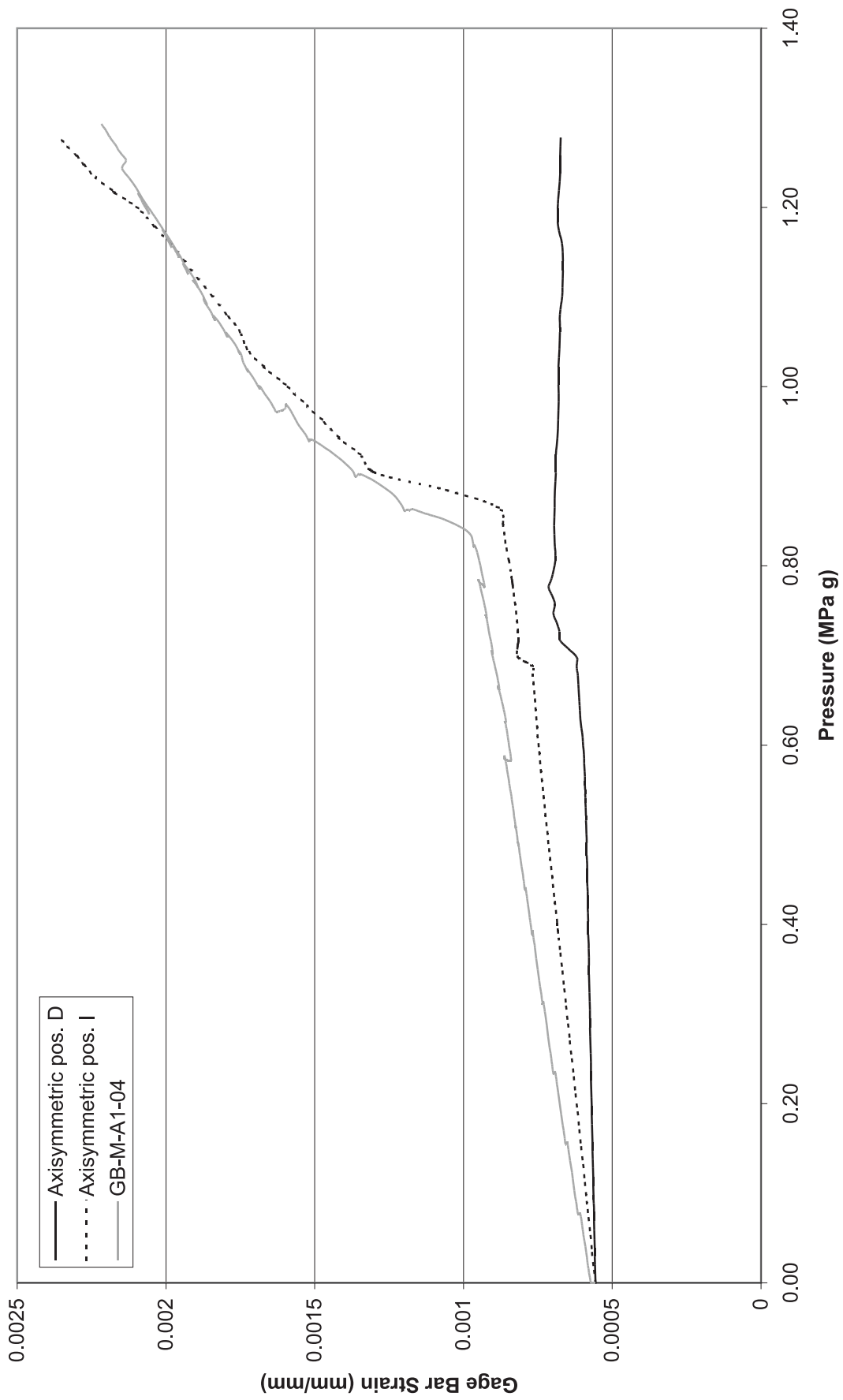


Figure 4-34. 1999 Pretest Analysis vs. LST at Wall Base Gage Bar Position D-I

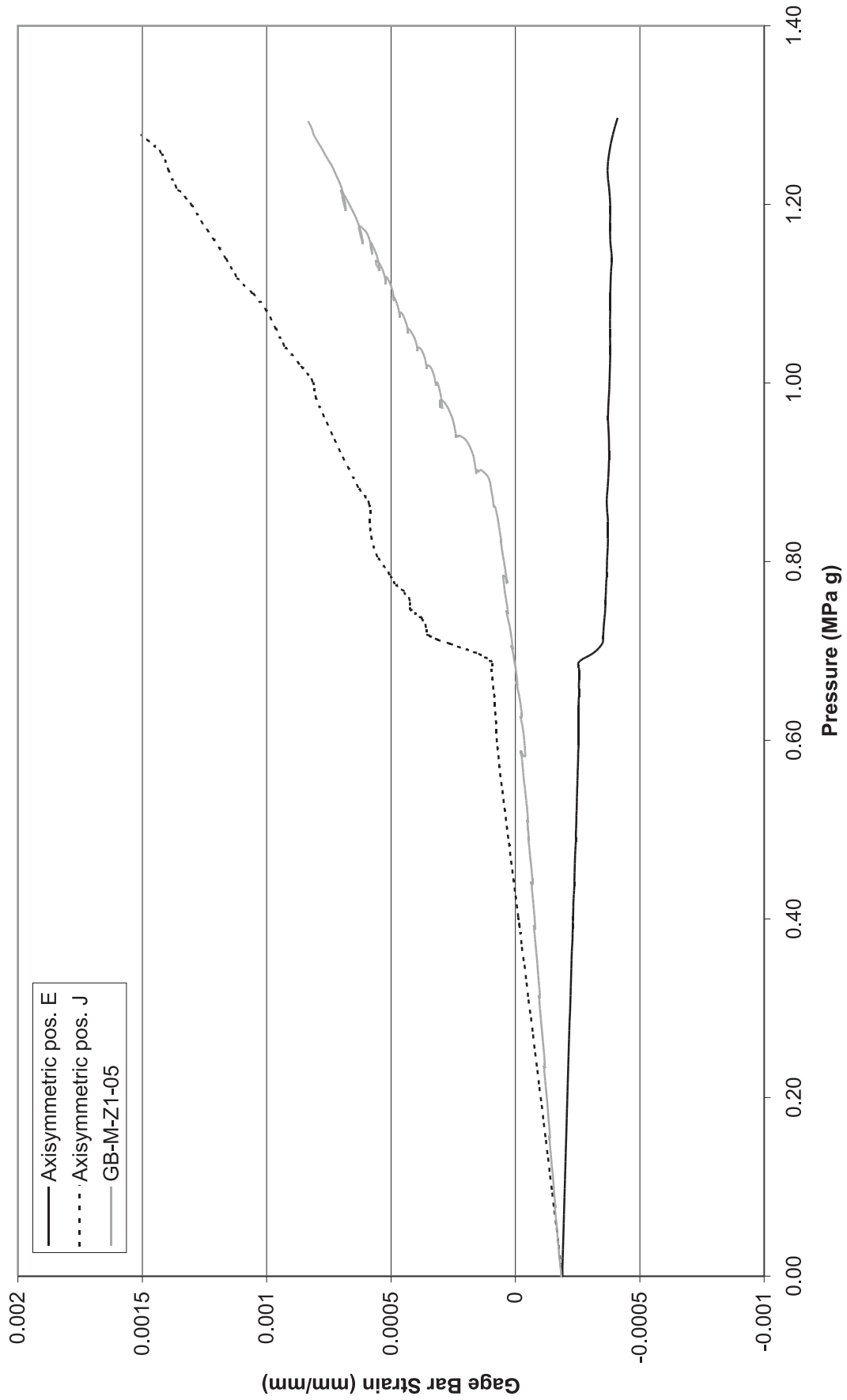


Figure 4-35. 1999 Pretest Analysis vs. LST at Wall Base Gage Bar Position E-J

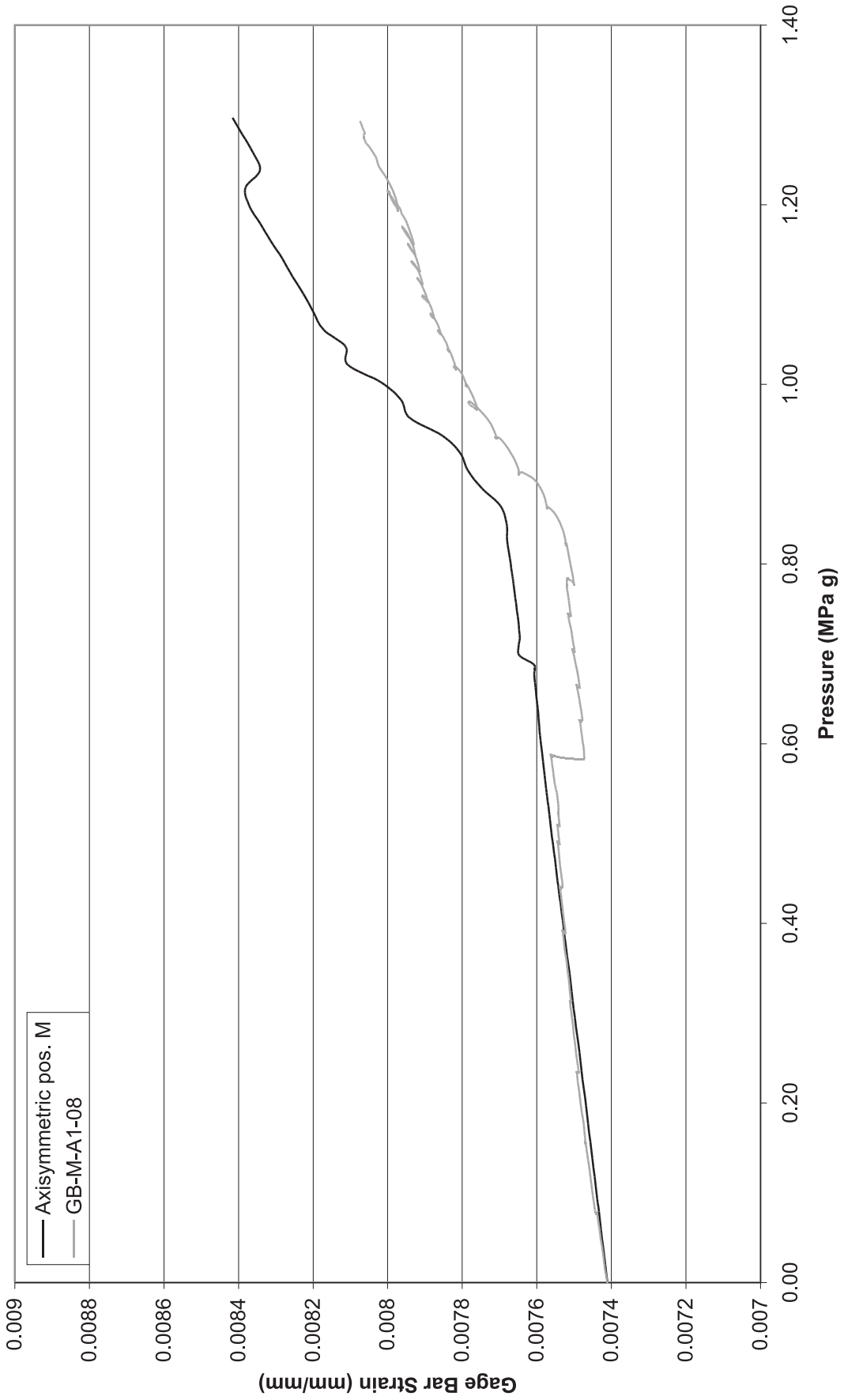


Figure 4-36. 1999 Pretest Analysis vs. LST at Wall Base Gage Bar Position M

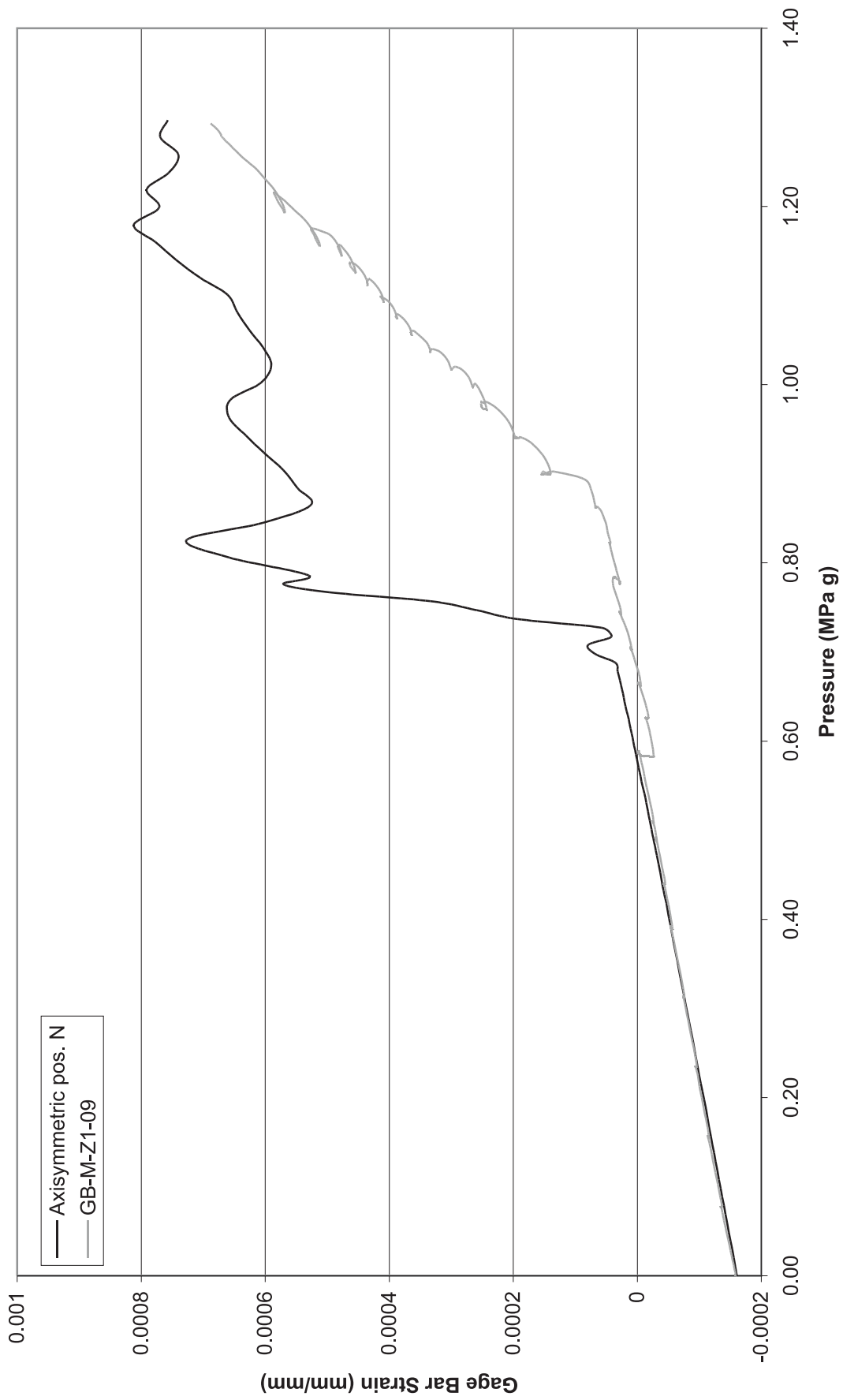


Figure 4-37. 1999 Pretest Analysis vs. LST at Wall Base Gage Bar Position N

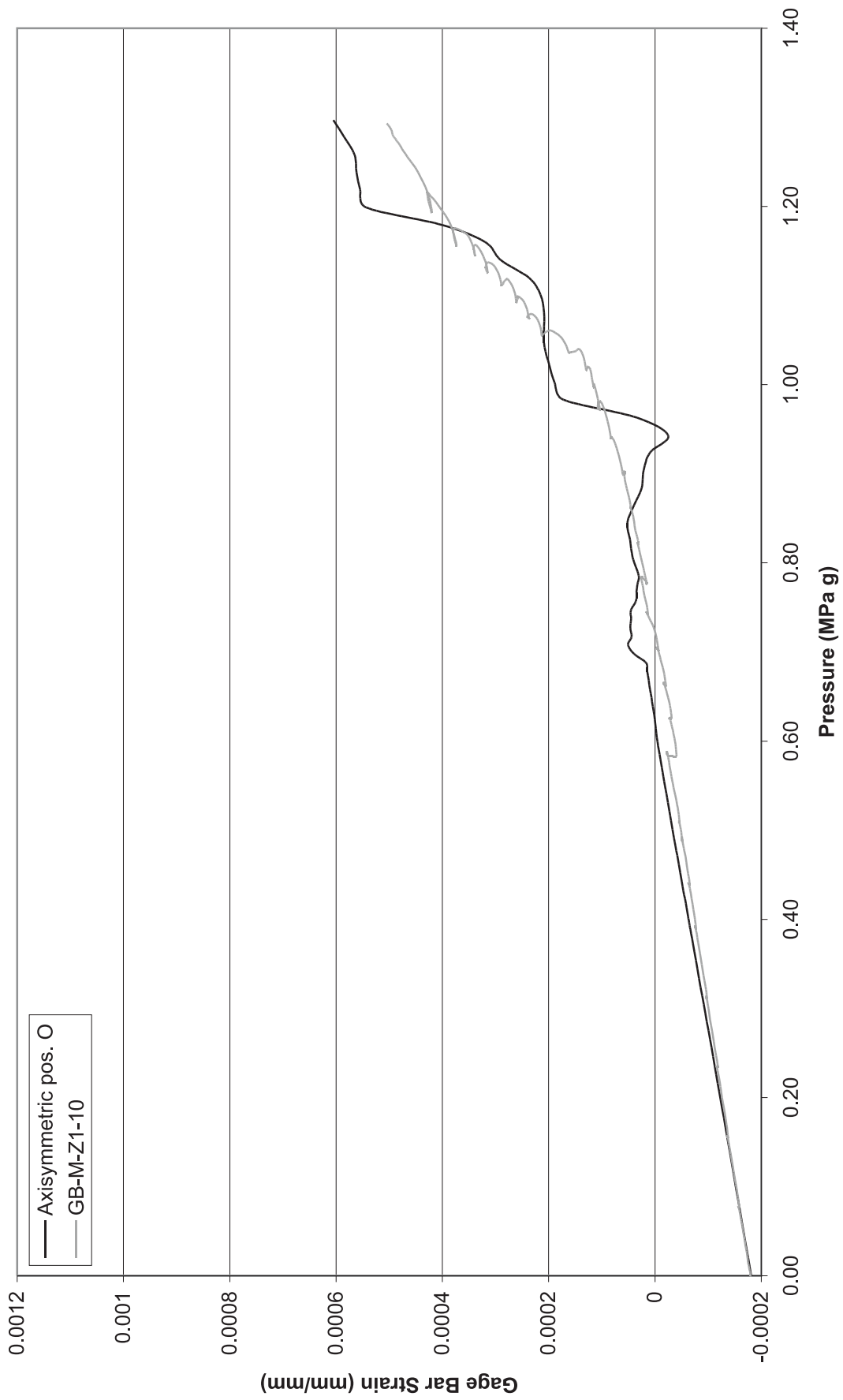


Figure 4-38. 1999 Pretest Analysis vs. LST at Wall Base Gage Bar Position O

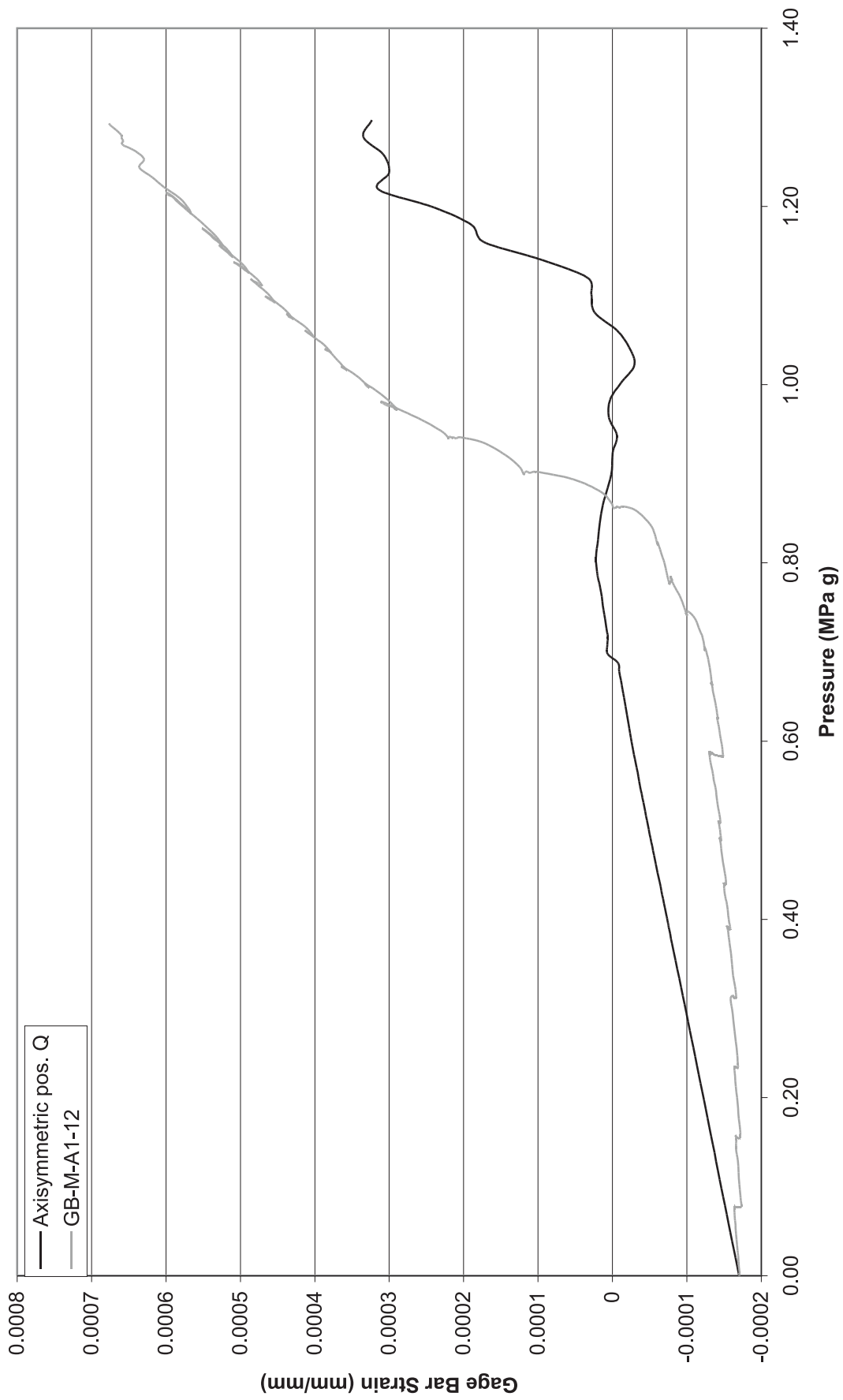


Figure 4-39. 1999 Pretest Analysis vs. LST at Wall Base Gage Bar Position Q

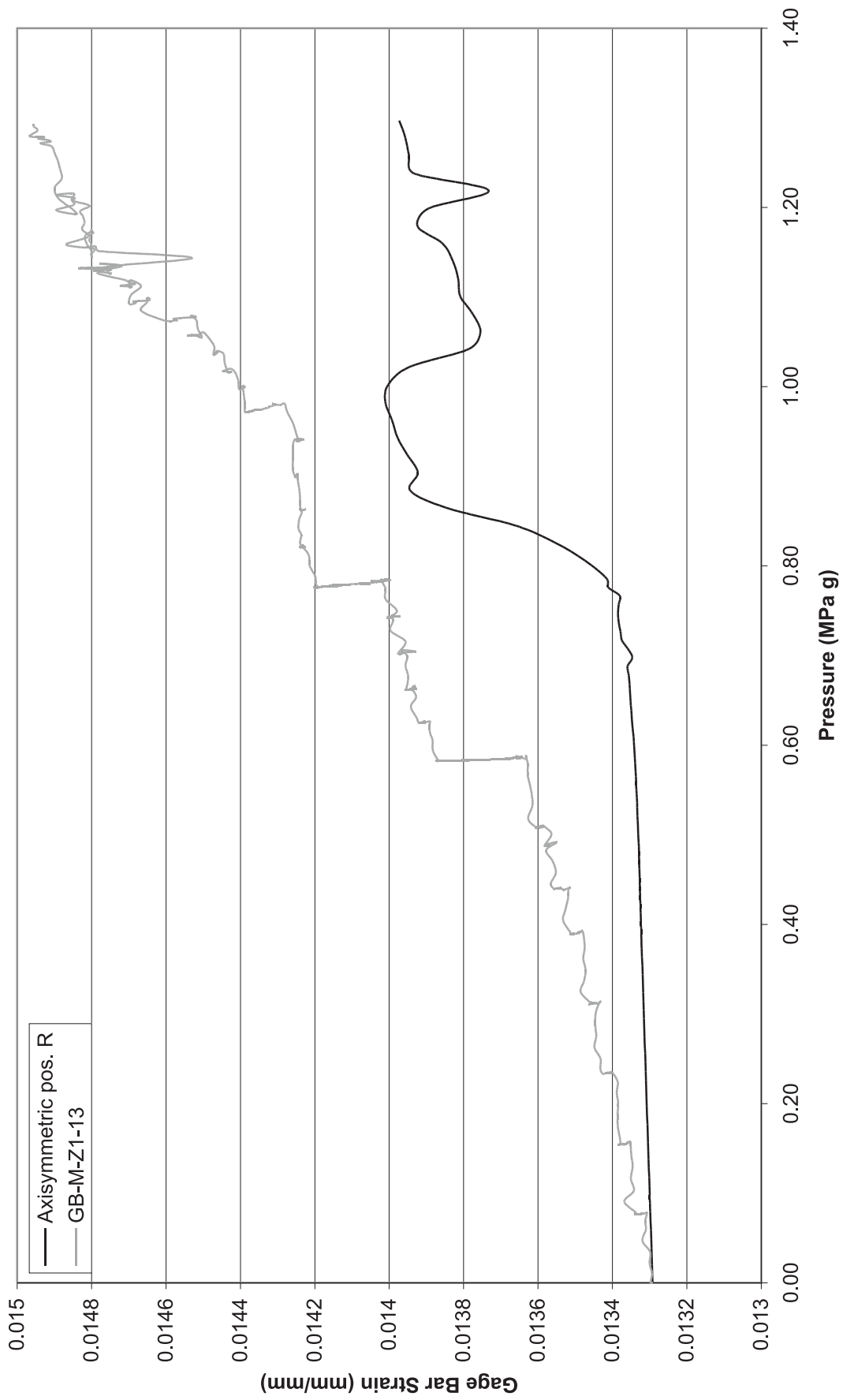


Figure 4-40. 1999 Pretest Analysis vs. LST at Wall Base Gage Bar Position R

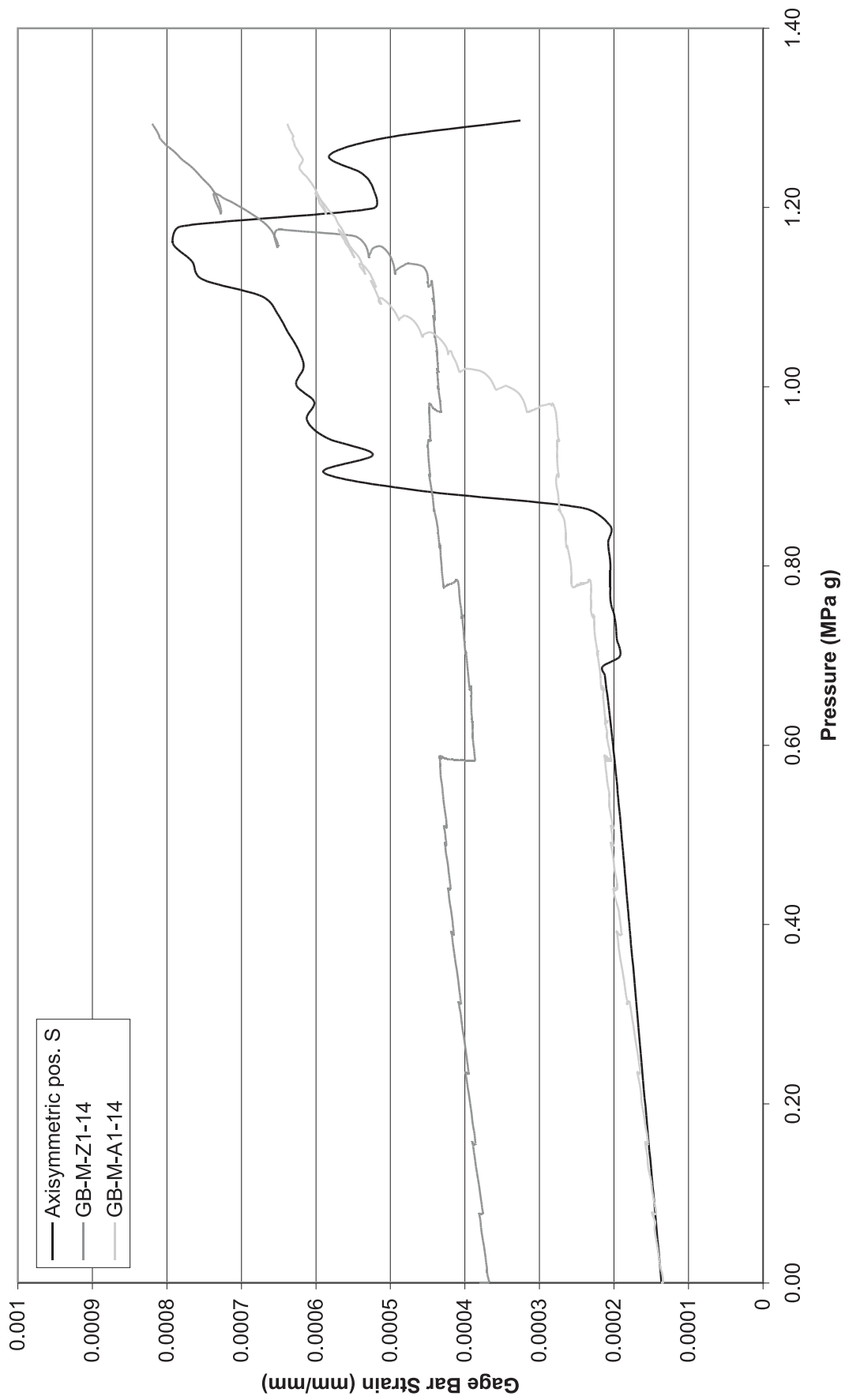


Figure 4-41. 1999 Pretest Analysis vs. LST at Wall Base Gage Bar Position S

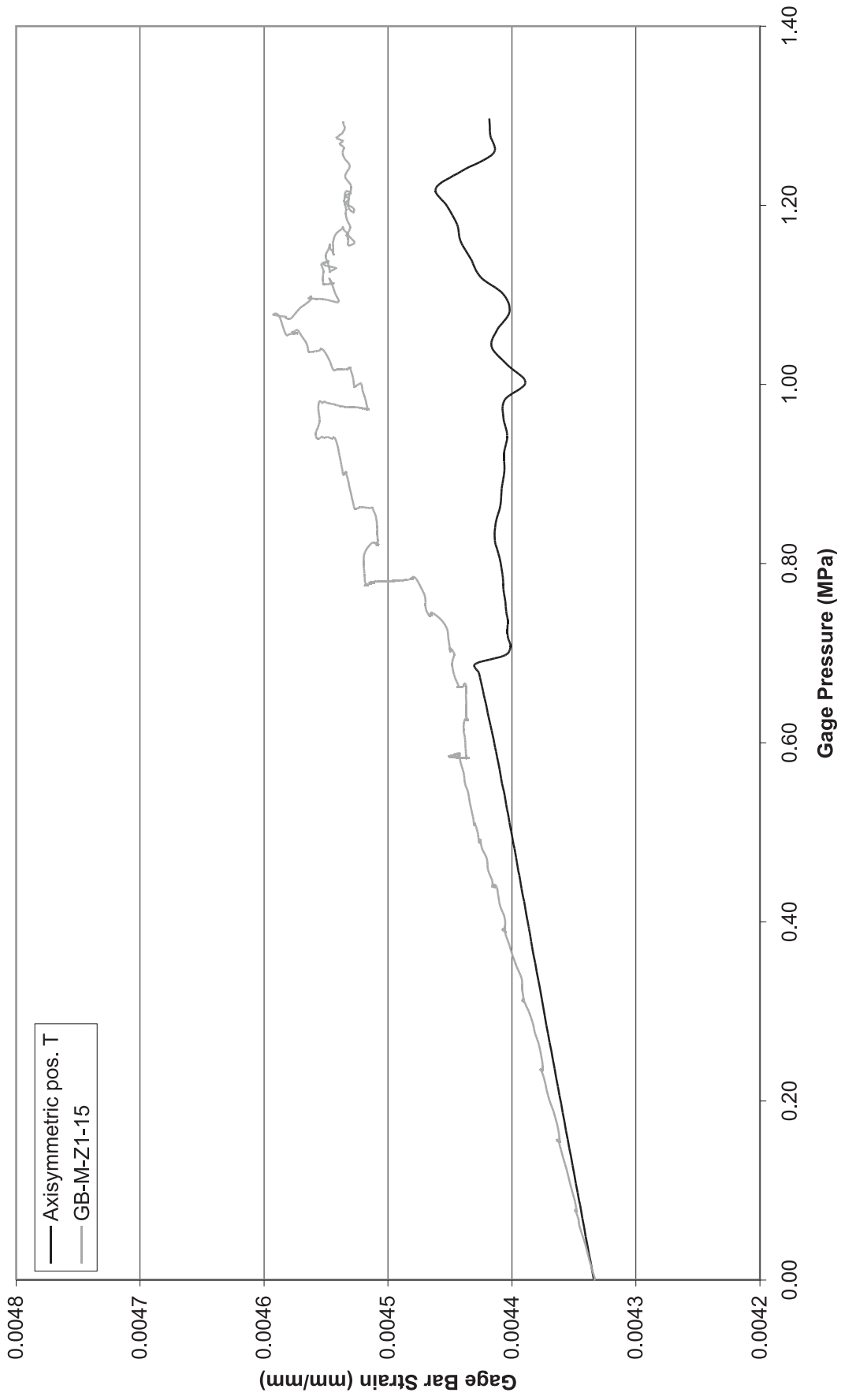


Figure 4-42. 1999 Pretest Analysis vs. LST at Wall Base Gage Bar Position T

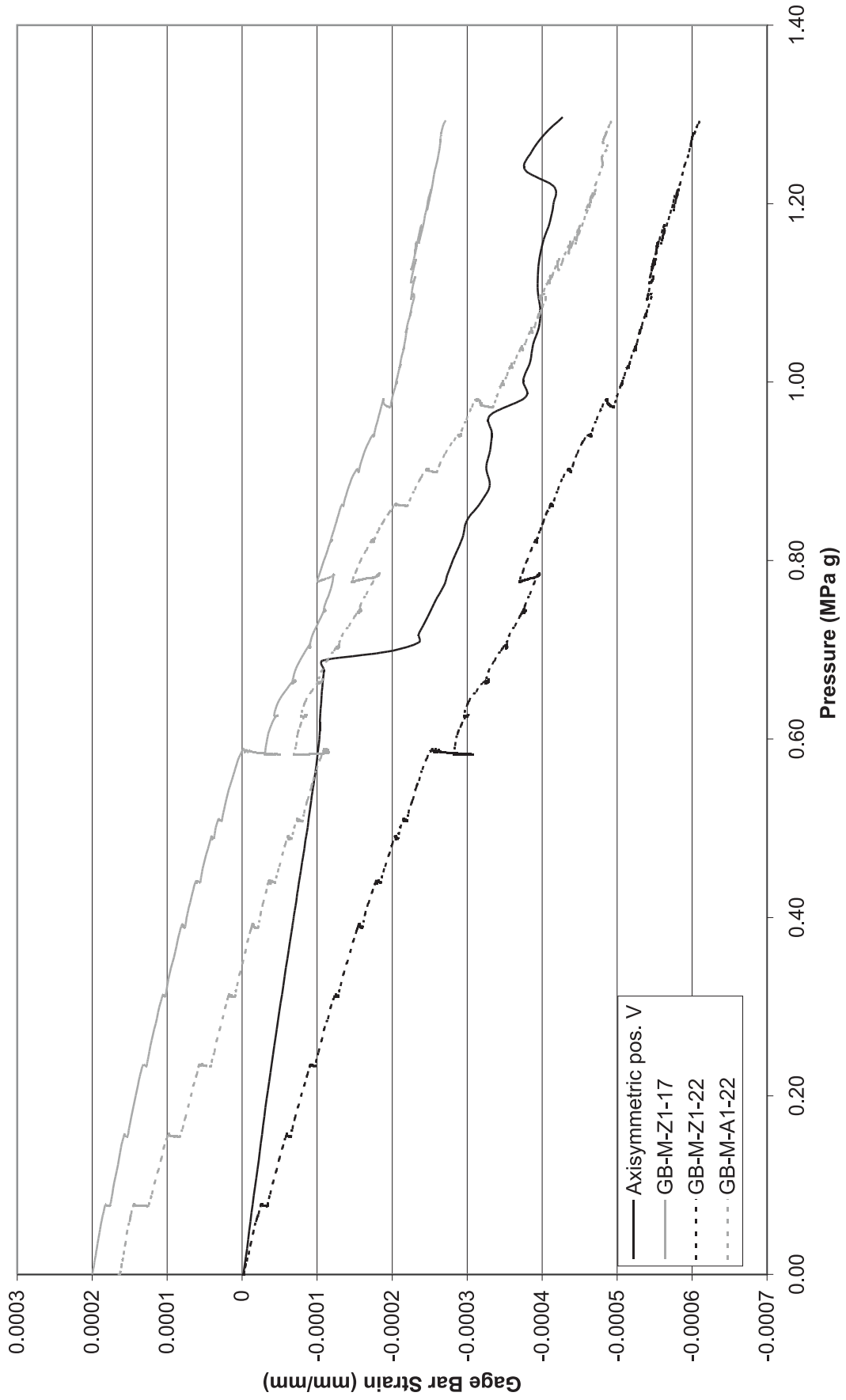


Figure 4-43. 1999 Pretest Analysis vs. LST at Wall Base Gage Bar Position V

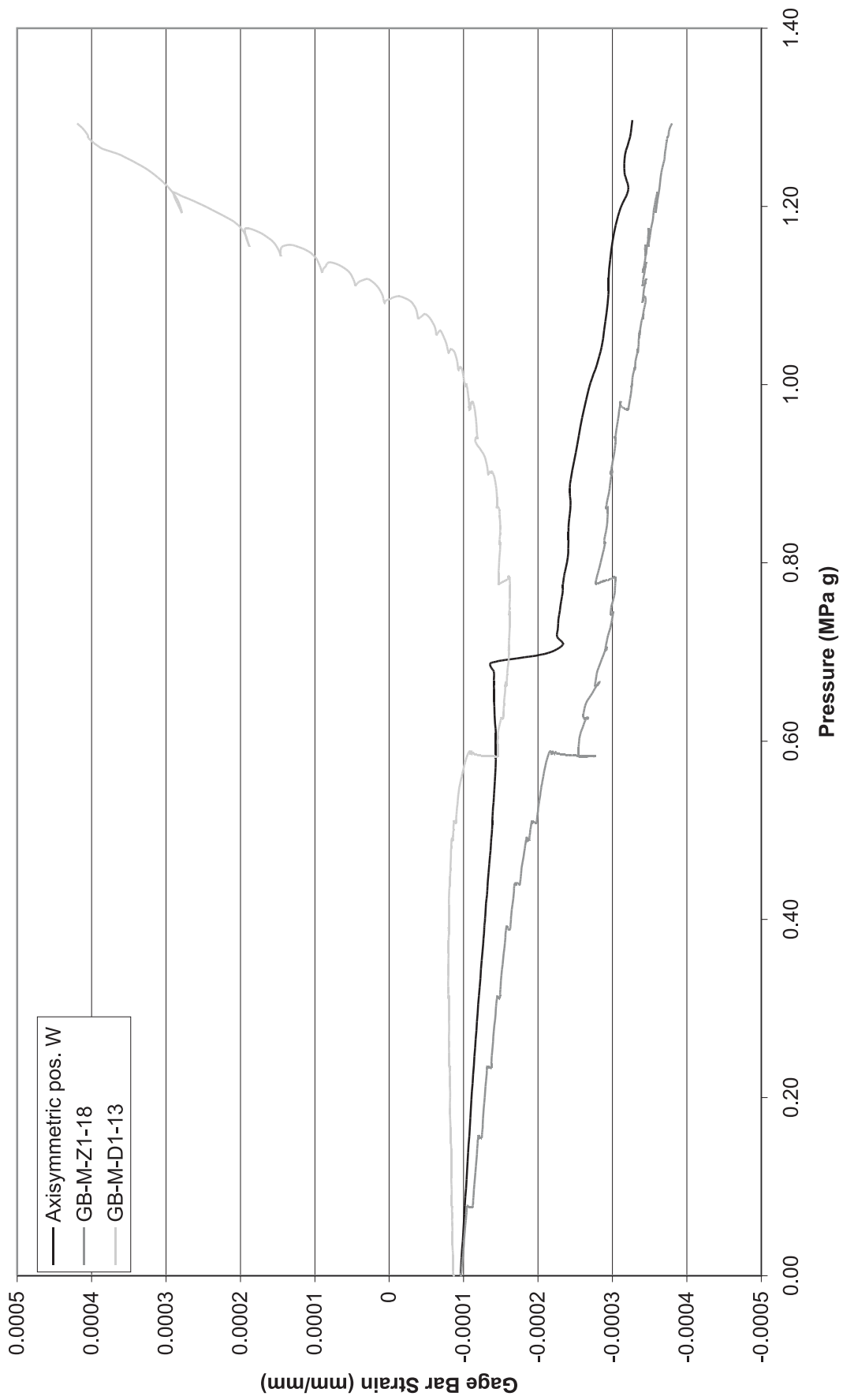


Figure 4-44. 1999 Pretest Analysis vs. LST at Wall Base Gage Bar Position W

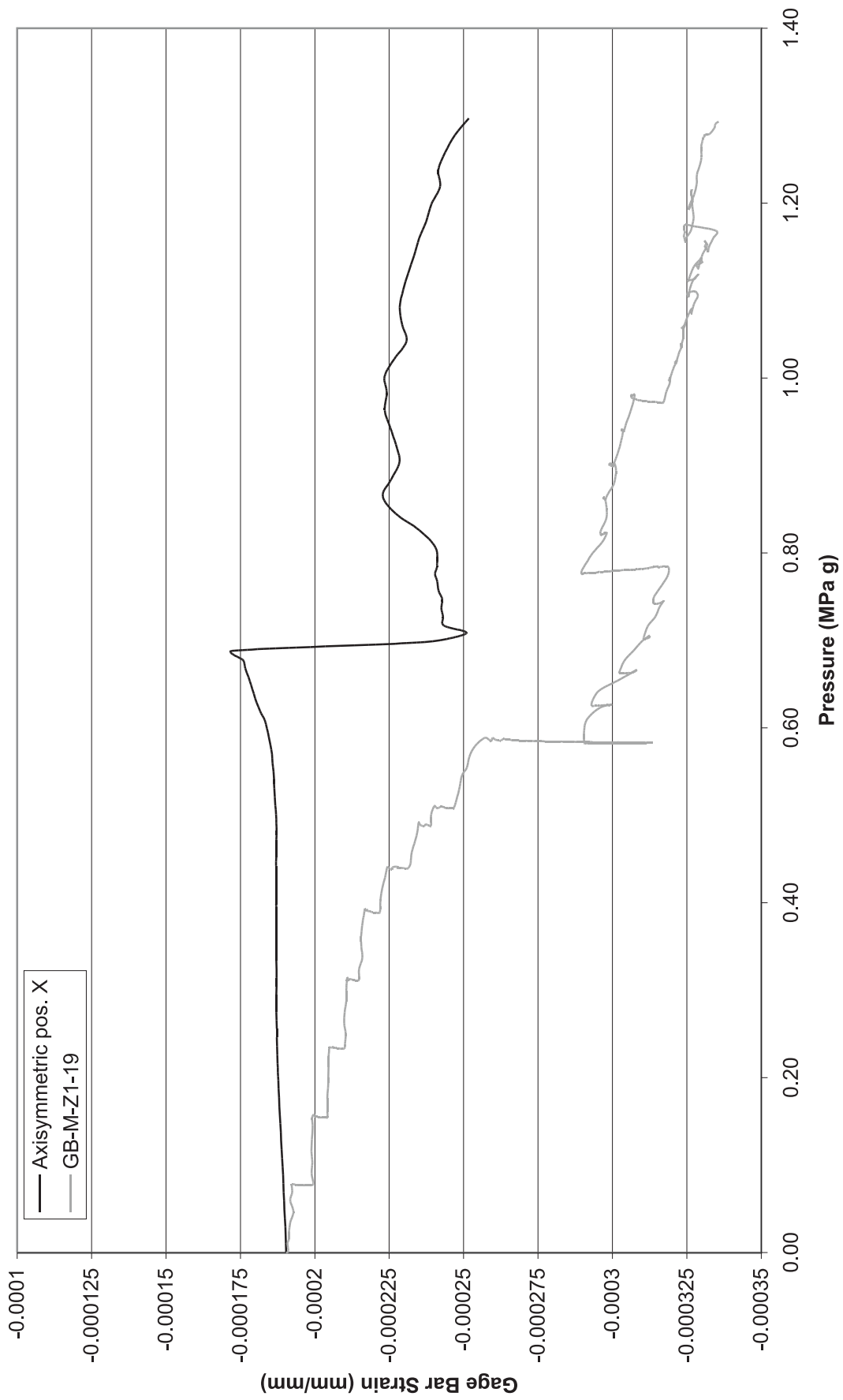


Figure 4-45. 1999 Pretest Analysis vs. LST at Wall Base Gage Bar Position X

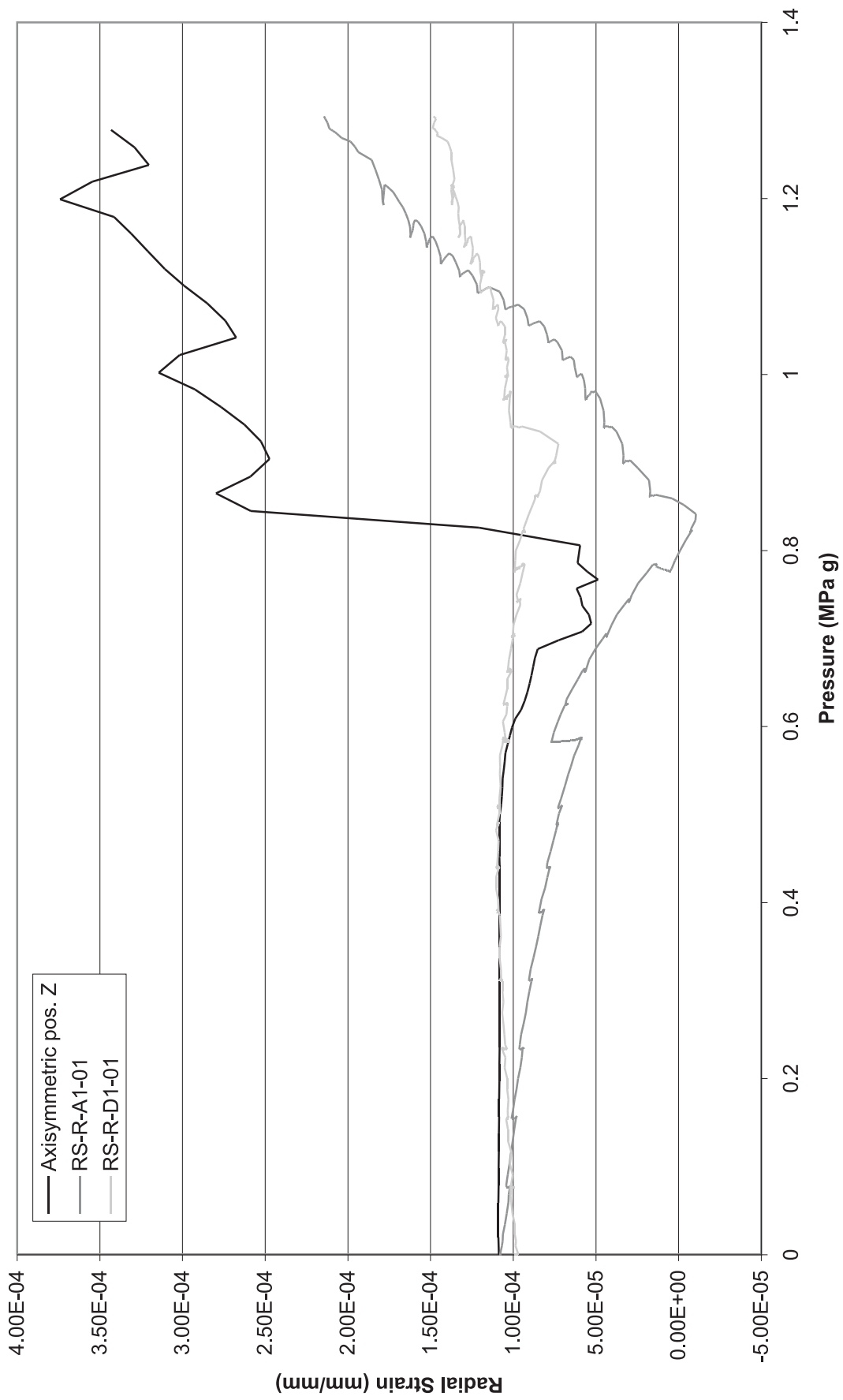


Figure 4-46. 1999 Pretest Analysis vs. LST at Wall Base Radial Stirrup Position Z

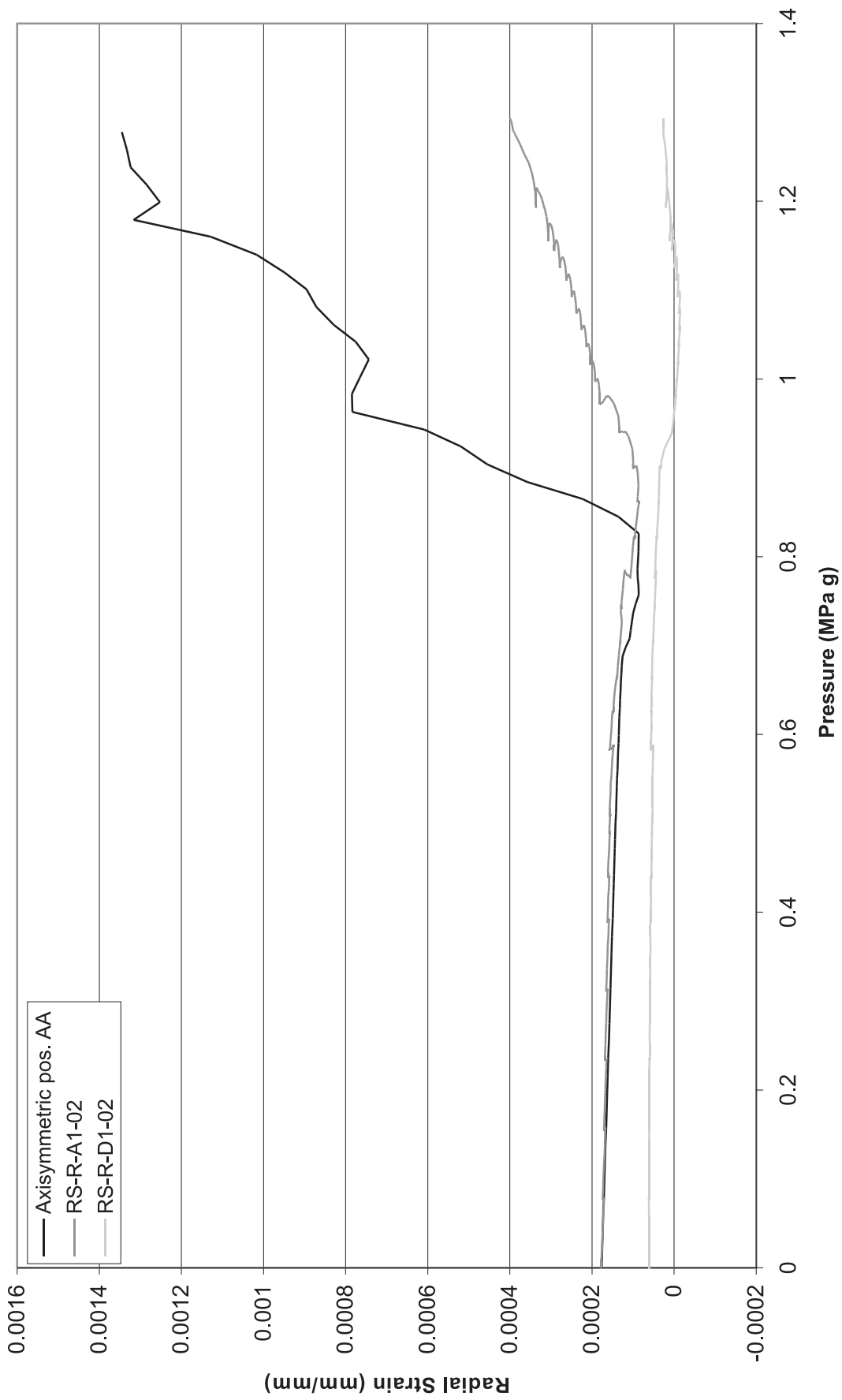


Figure 4-47. 1999 Pretest Analysis vs. LST at Wall Base Radial Stirrup Position AA

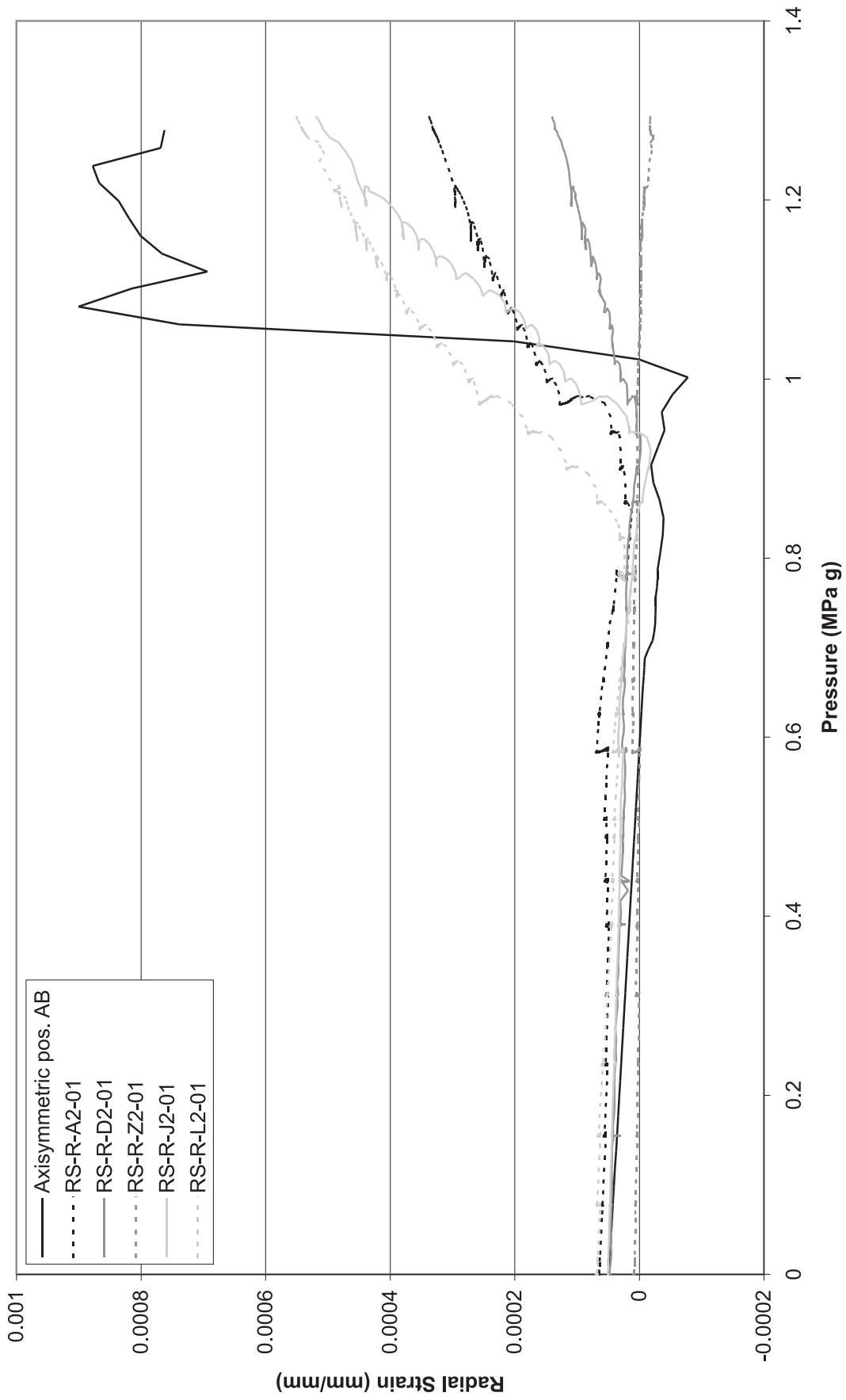


Figure 4-48. 1999 Pretest Analysis vs. LST at Wall Base Radial Stirrup Position AB

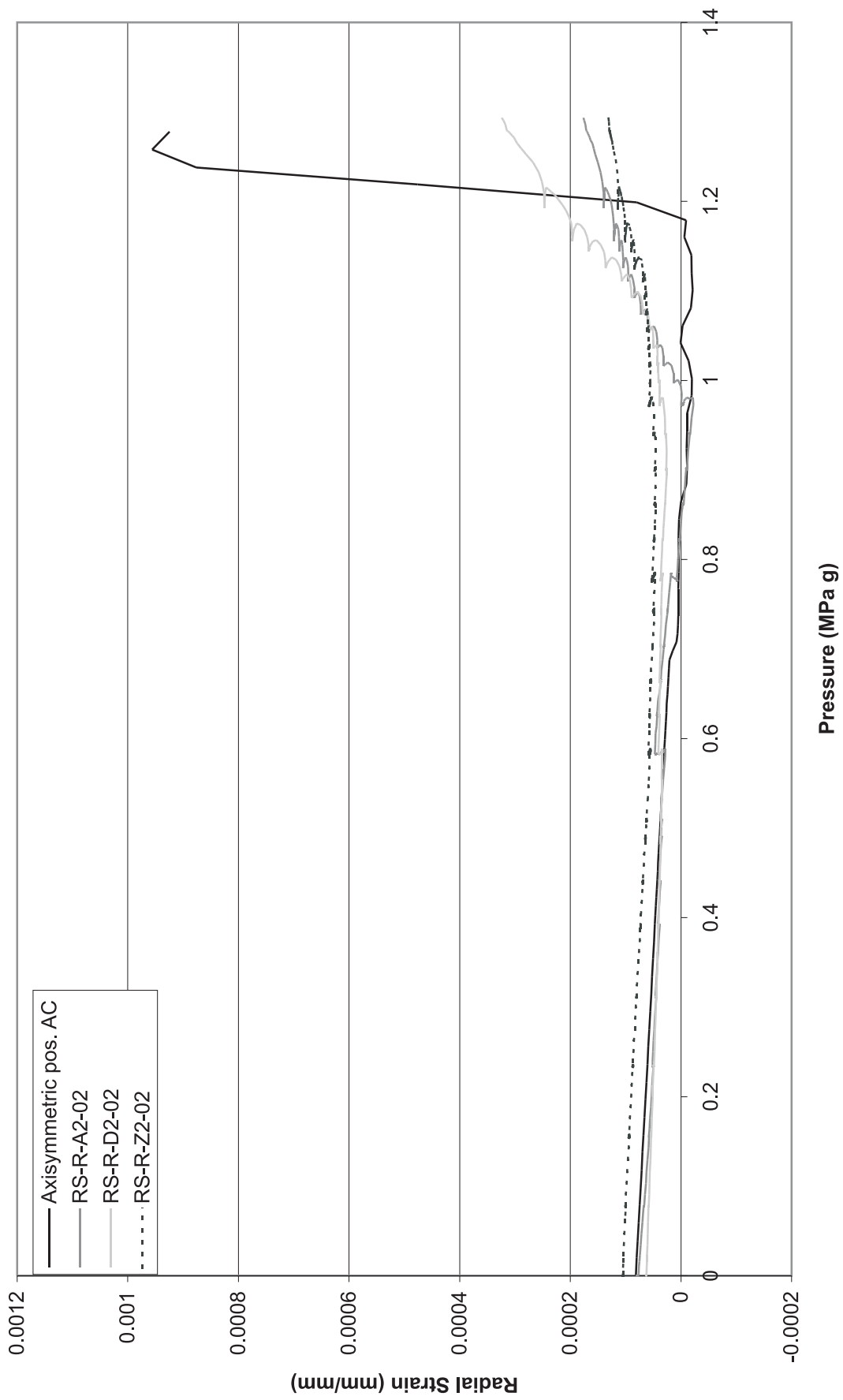


Figure 4-49. 1999 Pretest Analysis vs. LST at Wall Base Radial Stirrup Position AC

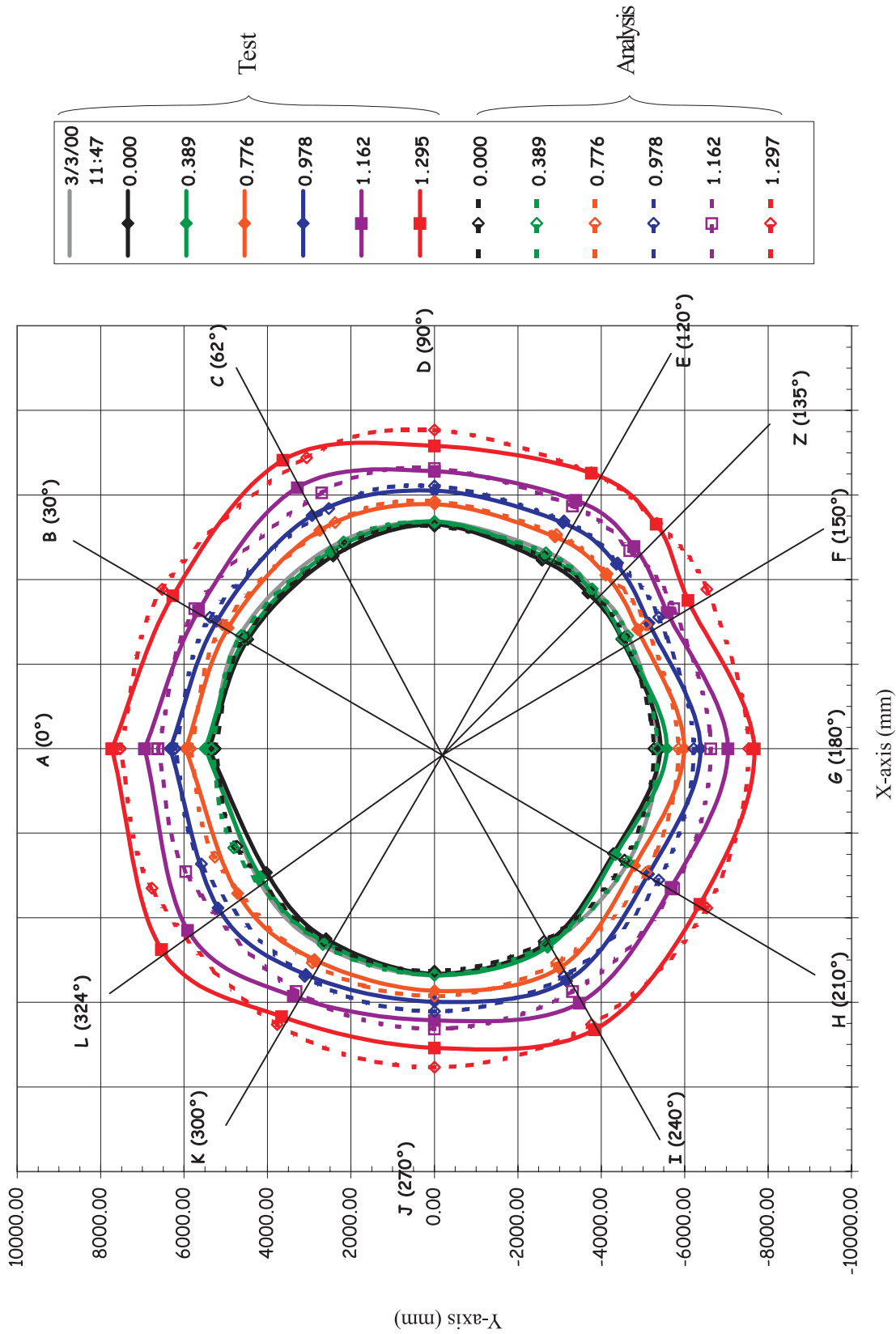


Figure 4-50. PCCV LST - Deformation @ El 4680 (5) x 100
Compared to Axisymmetric Pretest Analysis

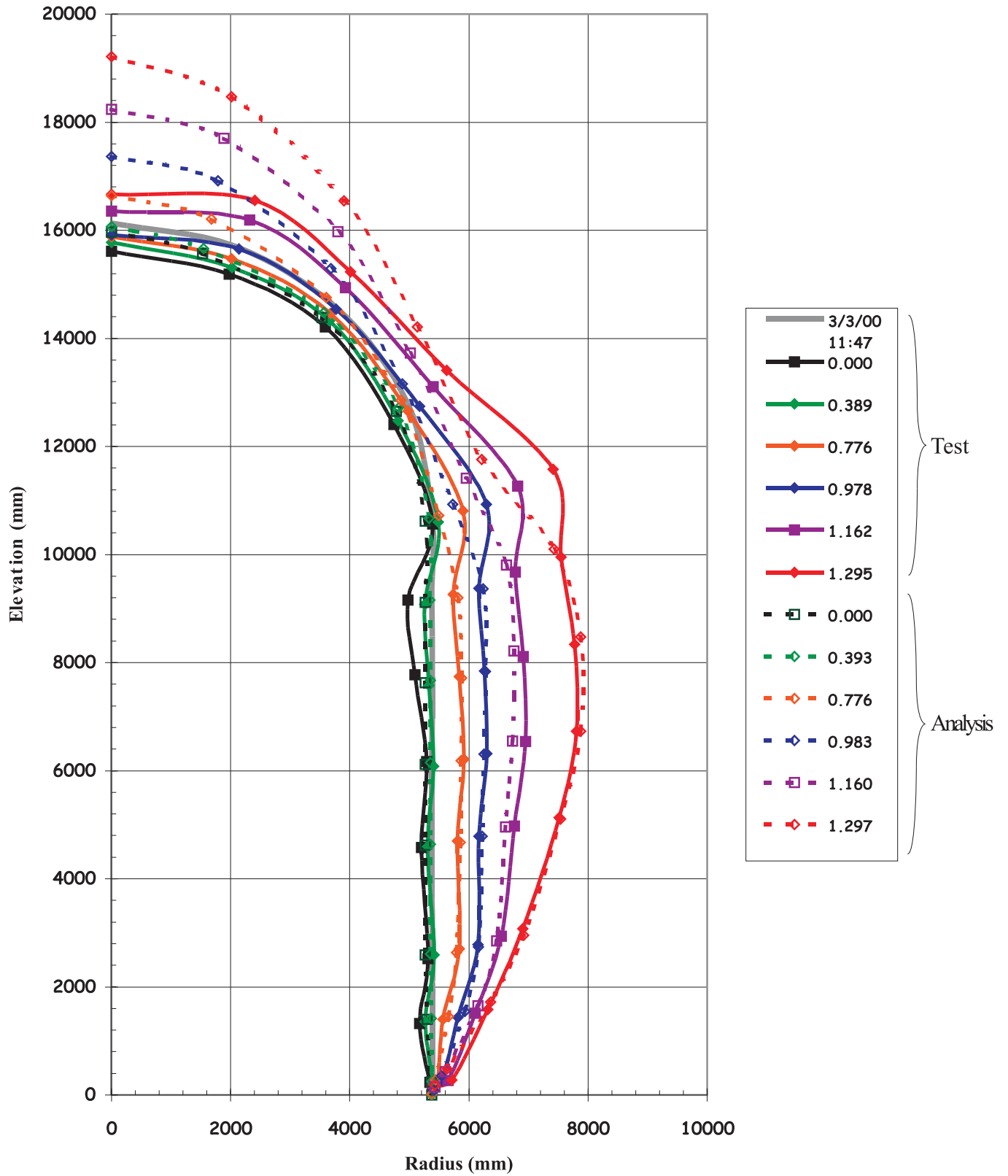


Figure 4-51. PCCV LST - Deformation @ Azimuth 135 (Z) \times 100 Compared to Axisymmetric Pretest Analysis

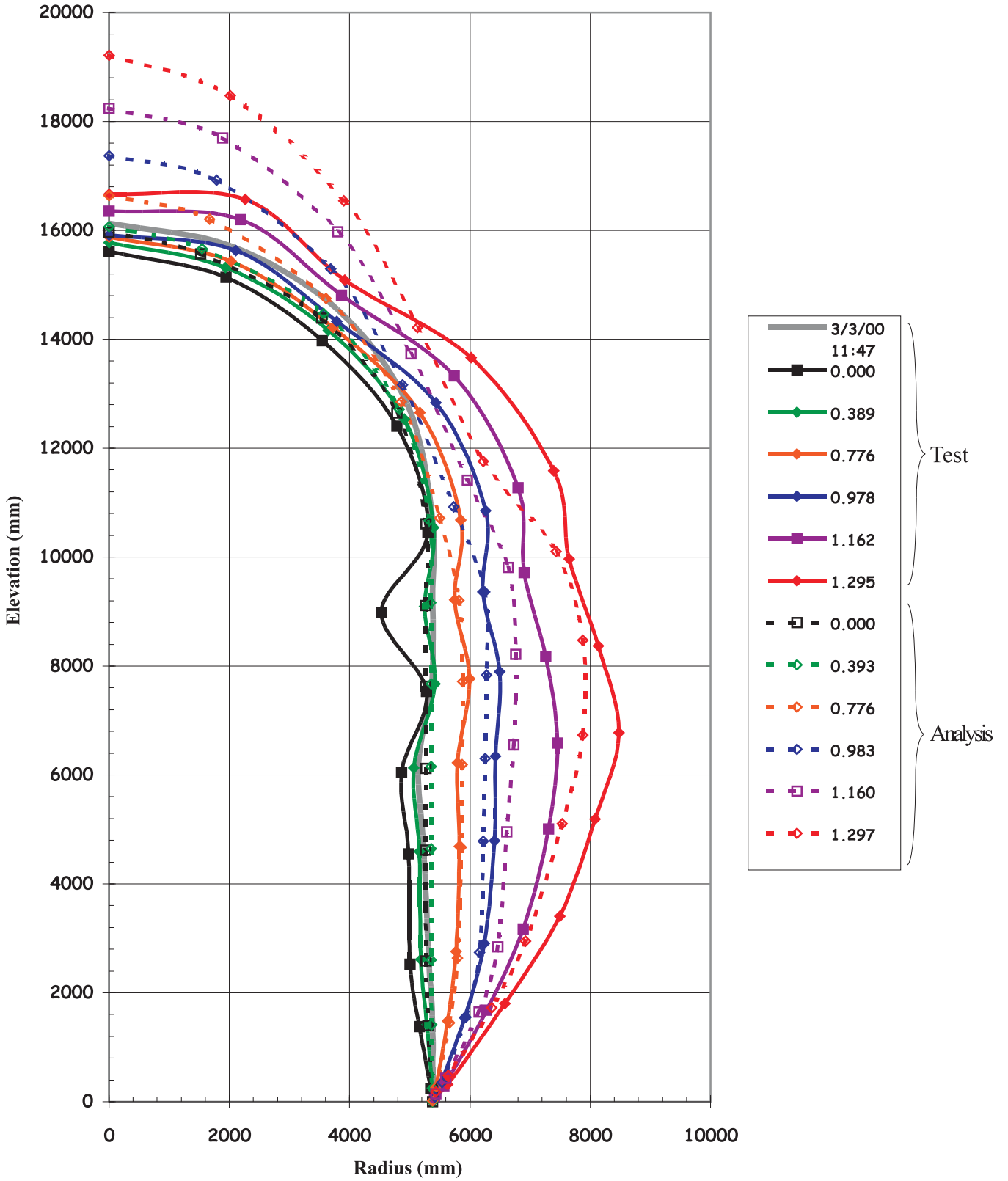


Figure 4-52. PCCV LST - Deformation @ Azimuth 324 (L) \times 100 Compared to Axisymmetric Pretest Analysis

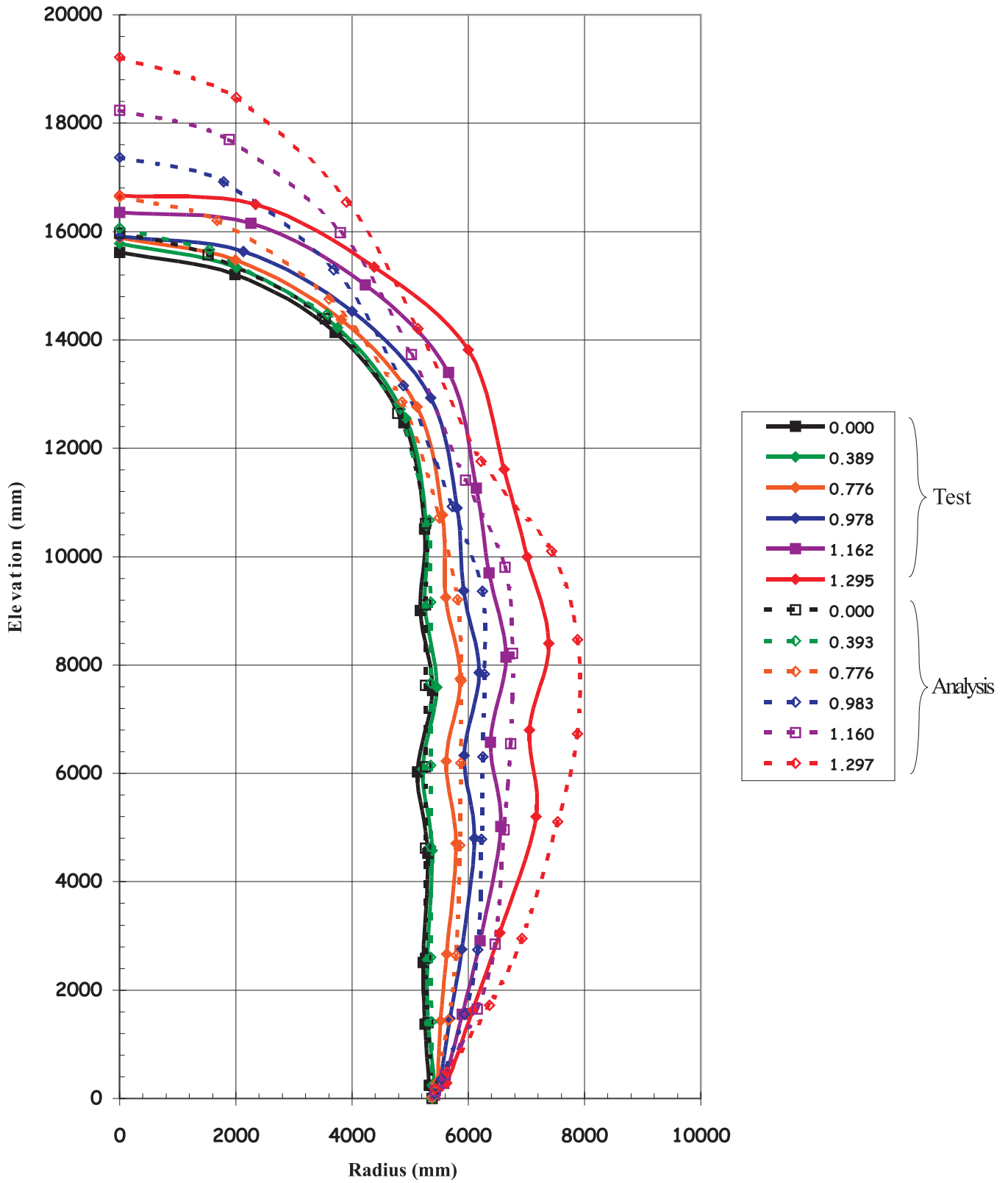


Figure 4-53. PCCV LST - Deformation @ Azimuth 90 (D) \times 100 Compared to Axisymmetric Pretest Analysis

